

Atmospheric correction of DInSAR phase for land subsidence measurements using an integrated approach

SHANKAR ACHARYA KAMARAJUGEDDA

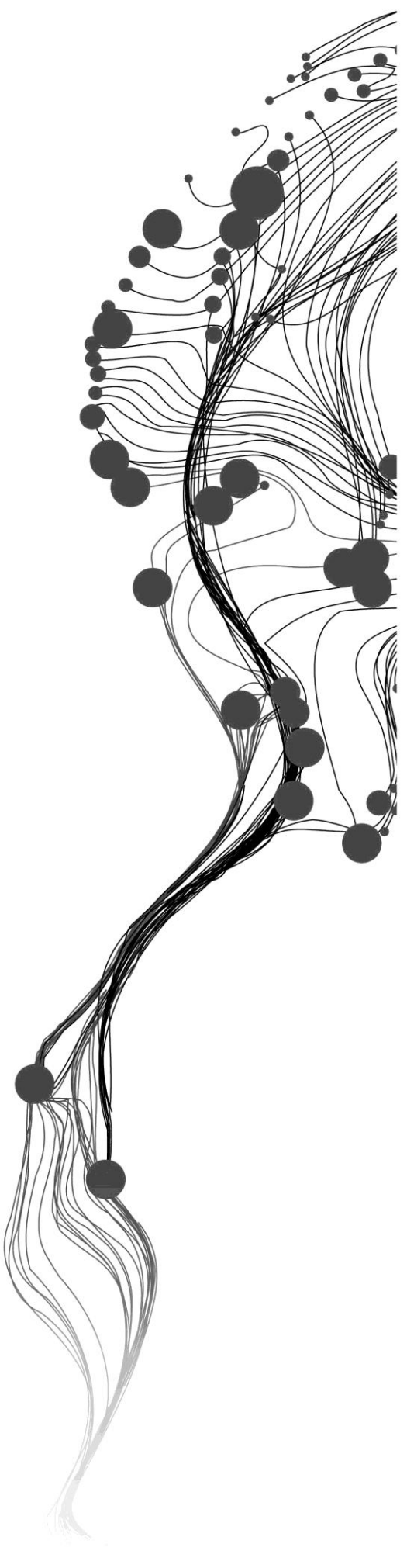
March, 2013

ITC SUPERVISOR

Dr. V.A.Tolpekin

IIRS SUPERVISORS

Dr. R.S.Chatterjee



Atmospheric correction of DInSAR phase for land subsidence measurements using an integrated approach

SHANKAR ACHARYA KAMARAJUGEDDA
Enschede, The Netherlands [March, 2013]

Thesis submitted to the Faculty of Geo-information
Science and Earth Observation of the University of Twente
in partial fulfilment of the requirements for the degree of
Master of Science in Geo-information Science and Earth
Observation.

Specialization: Geoinformatics

THESIS ASSESSMENT BOARD:

Chairperson : Prof. dr. ir. M.G. Vosselman
ITC Professor : Prof. dr. ir. A.Stein
External Examiner : Mr. Sanjay (DEAL, Dehradun)
ITC Supervisor : Dr. V.A.Tolpekin
IIRS Supervisor : Dr. R.S.Chatterjee



**FACULTY OF GEO-INFORMATION
SCIENCE AND EARTH OBSERVATION,
UNIVERSITY OF TWENTE,
ENSCHEDE, THE NETHERLANDS**

DEDICATED TO MY
LOVING FAMILY....

DISCLAIMER

This document describes work undertaken as part of a programme of study at the Faculty of Geo-information Science and Earth Observation of the University of Twente. All views and opinions expressed therein remain the sole responsibility of the author, and do not necessarily represent those of the institute.



ABSTRACT

Differential Interferometric Synthetic Aperture Radar (DInSAR) is an effective tool to measure the surface deformations. The measurements derived from this technique are affected due to the errors caused by the earth's atmosphere on the propagating RADAR signal. Troposphere and Ionosphere are the main layers of the atmosphere which induce the atmospheric error in DInSAR measurements. Many studies were performed to mitigate the effects of atmosphere on the RADAR signal traversing through it. The RADAR signals when propagating through the atmosphere undergo refraction. Research studies have shown that the temperature, pressure and water vapour pressure are the causative factors of RADAR signal refractivity in troposphere. The ionospheric refractivity is dependent on the Total Electron Content (TEC) present in the ionosphere. This study explores the integrated approach of using ground meteorological observations and satellite based meteorological data to model the atmospheric effects on the interferograms generated from RADARSAT-2 single look complex (SLC) data. Jharia coal field in Jharkhand was taken as the study area. The coal field is prone to land subsidence cause by mining activities. The DInSAR was generated from three RADARSAT-2 SLC's (acquisition dates: 12-10-2012, 29-11-2012 and 23-12-2012). The topography removal from the interferogram was performed using a 10m resolution DEM (Digital Elevation Model). Automated weather station (AWS) was used to obtain the ground meteorological observations and MODIS (Moderate Resolution Imaging Spectrometer) water vapour product (MOD07) was used for satellite based meteorological data. Since the time of pass of RADARSAT-2 is not in synchronization with MODIS, a regression analysis was performed to define a relationship between the meteorological data from AWS and MODIS. Hence the temperature, pressure and water vapour pressure were modelled for the time of acquisition of RADARSAT-2. The modelled bands were used to calculate the amount of tropospheric path delay. The tropospheric delay for the three acquisition dates ranged between 5.0 m and 5.07 m. The TEC data from IRI-2007 model was used to model the ionospheric path delay. The ionospheric path delays for the three acquisition dates were -0.189 m, -0.137 m and -0.118 m respectively. The negative sign indicates the phase advance caused due to presence of ions in the layer. The total delays observed for the three dates were subtracted from the phases of the differential interferograms generated. Three differential interferograms were generated for this study. Atmospheric correction was performed on the phase of all the three interferograms and the residual phase was analysed. Two differential interferograms exhibited excessive phase noise because of temporal decorrelation. These pairs were discarded for subsidence measurements. The better differential interferogram was used to extract the subsidence fringes. The subsidence rates for the fringes were validated with respect to ground levelling data. Two test sites were used in this study where ground levelling was performed. Subsidence fringes were observed from the differential interferogram for one of the test site (Bastacolla). The subsidence rates from DInSAR showed good correlation with the ground levelling data. No subsidence fringes were observed in the second test side (Mahespur). The low coherence caused due to temporal decorrelation might be one of the factors. The low coherence exhibited by the interferometric pairs lead to phase unwrapping problems. This approach provided a platform to explore the tropospheric and ionospheric path delays effects on the interferograms generated from RADARSAT-2 SLC's. Accurate subsidence measurements can be achieved when atmospheric correction is performed on interferometric pairs exhibiting higher coherence.

Keywords: DInSAR, troposphere, ionosphere, path delay, integrated approach, coherence, temporal decorrelation, total electron content, phase, subsidence, fringes.

ACKNOWLEDGEMENTS

Firstly I would like to give my sincere regards to my IIRS supervisor Dr. R.S.Chatterjee for his constant support and guidance throughout my research work. His experience and expertise have immensely helped me to complete the research work.

I am extremely thankful to my ITC supervisor Dr. V.A.Tolpekin for his valuable suggestions and guidance throughout my research work which made my work a success. I am very grateful to him for giving me an opportunity to be his student.

I would like to thank Dr. P.S.Roy (Former Director,IIRS) and Dr. Y.V.N.Krishna Murthy (Present Director,IIRS) for providing excellent infrastructure and facilities which made my stay comfortable and fruitful.

I would also like to thank Mr. P.L.N.Raju (Group Head, GID & PRSD) and Dr. S.K.Srivastav (Head GID) for their constant encouragement and help rendered throughout this course period.

I sincerely thank all the scientists of Geoinformatics department for their help and technical support throughout the course.

I would like to thank Dr. Nicholas Hamm for continuously observing my work in my project phase.

I feel very grateful to my parents and family who have always motivated and encouraged me and never let me feel dejected in difficult situations. Without their support I would have never achieved this.

Last but not the least I would like to thank all my friends specially Pavan, Bharadwaj, Bhavya, Hemanth, Ravi, Ankur, Jayson, Pavan.K, Mrinal, Anudeep, Anukesh, Deepak, Abhishek, Akhil, Chetan, Sharath and Dipima for their continuous moral and technical support throughout my research work.

TABLE OF CONTENTS

List of Figures	V
List of Tables	VII
1. INTRODUCTION	1
1.1. Background.....	1
1.2. InSAR.....	1
1.3. DInSAR	1
1.4. Atmospheric effects on SAR interferometry.....	2
1.4.1. Tropospheric path delay effects.....	2
1.4.2. Ionospheric path delay effects	3
1.5. Research Identification	4
1.5.1. Main research objective.....	4
1.5.2. Sub-objectives.....	4
1.5.3. Research Questions	4
1.5.4. Innovation aimed at.....	4
2. LITERATURE REVIEW	5
2.1. Introduction	5
2.2. InSAR theory	5
2.3. InSAR related work.....	6
2.4. DInSAR	7
2.5. Atmospheric effects on RADAR interferometry.....	10
2.5.1. Tropospheric effects on RADAR interferometry.....	10
2.5.2. Ionospheric effects on RADAR interferometry.....	13
3. STUDY AREA.....	15
3.1. Justification of choice of study area.....	16
4. MATERIALS AND METHODS.....	17
4.1. Materials used in the study	17
4.1.1. MODIS data	17
4.1.2. Ground meteorological data.....	18
4.1.3. Total Electron Content (TEC) data	18
4.1.4. SAR data.....	19
4.1.5. Digital Elevation Model (DEM)	19
4.1.6. Subsidence data obtained from ground levelling	20
4.2. Field Work.....	20
4.3. Atmospheric path delay computation	25
4.3.1. Tropospheric path delay	25
4.3.2. Ionospheric path delay	27
4.4. DInSAR generation.....	27
4.4.1. Image Co-registration and multilooking.....	27
4.4.2. Baseline estimation	28
4.4.3. Interferogram generation.....	29

4.4.4. Interferogram flattening and Topographic phase removal.....	31
4.4.5. Adaptive filter and coherence generation	31
4.4.6. Phase unwrapping.....	31
4.5. Phase correction	32
4.6. Validation of subsidence measurements.....	32
5. RESULTS AND DISCUSSION	34
5.1. Comparison of weather station meteorological parameters with MODIS derived parameters	34
5.2. Modelling the MODIS temperature and pressure bands for the time of acquisition of RADARSAT-2 using regression analysis between the weather station and MODIS readings.	38
5.3. Tropospheric path delay computation.....	45
5.4. Ionospheric path delay computation.....	47
5.5. Total path delay computation.....	47
5.6. DInSAR generation and phase correction	49
5.7. Subsidence measurement and validation	59
6. CONCLUSIONS AND RECOMMENDATIONS	62
6.1. Conclusions.....	62
6.2. Recommendations.....	63
REFERENCES.....	65

LIST OF FIGURES

Figure 2-1: Air borne InSAR imaging geometry with two antennae. Source [30]	5
Figure 2-2: Three pass SAR imaging geometry. A1, A2 and A2' are the antenna positions during the three pass acquisitions. The solid black lines are the RADAR signal path of the first interferogram pair formed by A1 and A2. The dashed black lines are the RADAR signal path of the second Interferometric pair formed by A1 and A2'. Source[18]	7
Figure 3-1(a): Geographical position of the study area (Dhanbad) in India.....	15
Figure 3-2(b): Cartosat-1 PAN sharpened LISS-IV image of the study area.	15
Figure 4-1: Flow chart of Methodology	17
Figure 4-2: Temperature plot of October.....	20
Figure 4-3: Pressure plot of October.....	21
Figure 4-4: Humidity plot of October.....	21
Figure 4-5: Temperature plot of November.....	22
Figure 4-6: Pressure plot of November	22
Figure 4-7: Humidity plot of November	23
Figure 4-8: Temperature plot of December	23
Figure 4-9: Pressure plot of December.....	24
Figure 4-10: Humidity plot of December	24
Figure 4-11: Interferogram of data pair (1).....	30
Figure 4-12: Interferogram of data pair (2).....	30
Figure 4-13: Interferogram of data pair (3).....	30
Figure 5-1: Comparison between temperature readings from weather station (WS) and MODIS in October.....	34
Figure 5-2: Comparison between pressure readings from weather station (WS) and MODIS in October.....	35
Figure 5-3: Comparison between temperature readings from weather station (WS) and MODIS in November	35
Figure 5-4: Comparison between pressure readings from weather station (WS) and MODIS in November.....	36
Figure 5-5: Comparison between temperature readings from weather station (WS) and MODIS in December.....	36
Figure 5-6: Comparison between pressure readings from weather station (WS) and MODIS in December	37
Figure 5-7: Temperature fit for October data.....	38
Figure 5-8: Pressure fit for October data.....	39
Figure 5-9: Temperature fit for November data.....	41
Figure 5-10: Pressure fit for November data	42
Figure 5-11: Temperature fit for December data	43
Figure 5-12: Pressure fit for December data	44
Figure 5-13: Histogram of tropospheric path delay caused on 12-10-2012	46
Figure 5-14: Histogram of tropospheric path delay caused on 29-11-2012	46
Figure 5-15: Histogram of tropospheric path delay caused on 29-12-2012	46

Figure 5-16: Histogram of total path delay caused on 12-10-2012.....	48
Figure 5-17: Histogram of total path delay caused on 29-11-2012.....	48
Figure 5-18: Histogram of total path delay caused on 23-12-2012.....	48
Figure 5-19: Differential interferogram (DInt) of data pair (1).....	49
Figure 5-20: DInt phase of data pair (1)	50
Figure 5-21: Corrected DInt phase of data pair (1)	49
Figure 5-22: Phase variation before correction.....	49
Figure 5-23: Phase variation after correction.....	49
Figure 5-24: Corrected differential interferogram of data pair (1).....	50
Figure 5-25: Differential interferogram of data pair (2)	51
Figure 5-26: DInt phase of data pair (2)	52
Figure 5-27: Corrected DInt phase of data pair (2)	51
Figure 5-28: Phase variation before correction.....	52
Figure 5-29: Phase variation after correction.....	51
Figure 5-30: Corrected differential interferogram of data pair (2).....	52
Figure 5-31: Differential interferogram of data pair (3)	52
Figure 5-32: DInt phase of data pair (3).....	54
Figure 5-33: Corrected DInt phase of data pair (3)	53
Figure 5-34: Phase variation before correction.....	54
Figure 5-35: Phase variation after correction.....	53
Figure 5-36: Corrected differential interferogram of data pair (3).....	53
Figure 5-37: Fint before correction (pair 1)	55
Figure 5-38: Fint after correction (pair 1).....	54
Figure 5-39: Fint before correction (pair 2)	56
Figure 5-40: Fint after correction (pair 2).....	55
Figure 5-41: Fint before correction (pair 3)	56
Figure 5-42: Fint after correction (pair 3)	55
Figure 5-43: Subsidence fringe before correction	56
Figure 5-44: Subsidence fringe after correction.....	56
Figure 5-45: Coherence image of data pair (1).....	56
Figure 5-46: Coherence image of data pair (2).....	57
Figure 5-47: Coherence image of data pair (3).....	57
Figure 5-48: Coherence image of Maheshpur test site	58
Figure 5-49: Coherence image of Bastacolla test site.....	58
Figure 5-50: Map showing subsidence fringes and test site locations.....	59
Figure 5-51: Map showing subsidence rate of observed fringes	60
Figure 5-52: Subsidence zones observed near Bastacolla test site.....	61

LIST OF TABLES

Table 4-1: RADARSAT-2 SLC data specifications.....	19
Table 4-2: Dataset extent.....	19
Table 4-3: Baseline values of interferometric pairs	29
Table 5-1: Ionospheric path delay calculated from TEC	47
Table 5-2: Subsidence rate of subsidence zones identified near Bastacolla test site	61

1. INTRODUCTION

1.1. Background

Accurate topographic measurements are important in the fields of geology, geophysics and hydrology [1]. In recent times, topographic data is being generated using many techniques. Topographic data generation involves stereographic techniques using optical remote sensing and lately with the evolution of GPS technology, point positioning has come to light [2]. Among the techniques, Radio Detection and Ranging (RADAR) interferometry is a very promising technique in the field of accurate topographic measurements. With the recent increase in the number of SAR (Synthetic Aperture Radar) sensors on different space borne platforms, these sensors are able to collect the data all over The Earth [2]. Unlike optical remote sensing, SAR observations can be collected even at night time because SAR is an active sensor having its own source of radiation. The SAR operational wavelength ranging from 1 mm to 1 m has an additional advantage of cloud penetration as opposed to optical remote sensing [2].

Interferometric Synthetic Aperture Radar (InSAR) and Differential Interferometric Synthetic Aperture Radar (DInSAR) are widely used tools to measure the topographic profile and surface deformations [3]. These deformations could occur due to phenomena like landslides, land subsidence, earthquakes, etc.

1.2. InSAR

SAR data is in complex format where each pixel contains information of phase and amplitude. SAR interferometry (InSAR) is a technique which extracts the height information of the earth's surface using the phase content [3]. InSAR technique requires minimum two SAR images. This technique generates an interferogram. The interferogram is formed by phase difference between two images. Interferometry is classified as single pass or repeat pass based on the mode of acquisition. In case of single antenna system, revisit to the same scene is required. This is called repeat pass interferometry [4]. Topographic height measurements and surface displacements have been major applications of repeat pass interferometry.

1.3. DInSAR

The Repeat pass Interferometric SAR phase contains topographic information along with surface deformation information. This leads to misinterpretation of topographic information as surface deformation. To overcome this constraint DInSAR technique has been introduced.

A minimum of three Single Look Complex (SLC) data are required for repeat pass interferometry. With these inputs two Interferometric phases can be generated. Then the phases for each pixel of the two interferograms generated are subtracted to produce a differential interferogram.

DInSAR is generated using two pass, three pass or multi-pass satellite data. Two - pass technique uses an external Digital Elevation Model (DEM) along with an Interferometric pair to generate a DInSAR. The resultant interferogram is free from topography. Hence this generated DInSAR will be a composition of phase noise, surface deformations/displacements and atmospheric delay.

DInSAR technique provides much precise surface deformation with accuracies up to 1 cm over large swaths [5].

Atmospheric effects are one of the main sources of error that influence the final results of DInSAR. Because of this, the differential interferograms have both deformation fringes and atmospheric fringes. These atmospheric effects can deprive the accuracy of surface deformation measurements [6]. In general small errors due to atmospheric effects might contribute to large errors due to other effects. In case of slow deforming areas, along space and time, these corrections are necessary for accurate measurements of these deformations [7]. This is the reason due to which atmospheric effects in DInSAR are important.

1.4. Atmospheric effects on SAR interferometry

RADAR signal propagation is affected by the atmosphere mainly by troposphere and ionosphere. The presence of water vapour in the troposphere and the presence of electron content (ions) in the ionosphere lead to the bending and delay in the propagation of RADAR signal [4]. The signal attenuation depends on the wavelength. Due to these atmospheric effects, the signal undergoes additional time delay due to the refractive index of the atmosphere [8].

In repeat pass interferometry, atmospheric effects are significant due to the variable state of atmosphere between the acquisitions [9]. Tropospheric errors caused by spatiotemporal changes of 20% in relative humidity can be in the order of 10 cm in deformation products [9]. This is a very high value in the context of deformation due to land subsidence. Ionospheric effects are wavelength dependent. RADAR waves traversing through ionosphere suffer distortions because of its dispersive nature caused by the free electrons or ions present in the medium. The total number of electrons per cubic meter (i.e., electron density) is the main reason for RADAR signal path shortening during its passing through this medium.

The tropospheric and ionospheric path delays can mask subtle deformation signatures. These effects on DInSAR phase can influence the accuracy of derived measurements. So calibration and mitigation of atmospheric effects on DInSAR phase is vital for precise measurements.

1.4.1. Tropospheric path delay effects

Troposphere is the lower most layer of the earth's atmosphere comprising of water vapour, clouds and aerosols. It extends up to 50 km from earth's surface. The refractivity of the RADAR signal propagating through this layer is mainly affected by temperature, air pressure, water vapour pressure and water content in clouds present in this layer.

Some of the previous works in mitigation of tropospheric effects on repeat pass interferometry have been done by using different techniques based on ground meteorological observations, GPS observations, high resolution meteorological models, MODIS and MERIS water vapour data, correlation analysis, stacking methods, etc [4]. Each of these methods has advantages and limitations.

Tropospheric delay was calibrated using surface weather data [10]. These results were used to calibrate InSAR measurements. The integration of meteorological data along with GPS observations was suggested [11]. The fact is that the spatial resolution of GPS stations is lower than that of the InSAR data in terms of coverage. This serves as a potential limitation for using

only GPS observations. Having dense GPS networks is also not always economically feasible and it is difficult to setup in remote areas.

High resolution meteorological models like NWP (Numerical Weather Prediction model) have been used by several authors [12]. These models are always questioned in the scientific community in terms of their reliability because often they are modelled based on specific observations.

A recent study by Li et al. [13] recommended meteorological data to be used along with MERIS data (water vapour product). MODIS and MERIS have brought a revolution in modelling and correcting tropospheric effects on InSAR. These sensors provide water vapour pressure data to quantify the error caused by it. Many studies [13, 14] have made use of this data coupled with GPS observations. MODIS data (water vapour product) has a high spatial resolution of $1\text{km} \times 1\text{km}$ and MERIS has a resolution of $0.3\text{ km} \times 0.3\text{ km}$. These are very useful for modelling and correcting atmospheric effects on InSAR. The advantage of this data is that the densest GPS network resolution in the world is ten times sparser than the resolution of MODIS [4]. However the presence of cloud cover is the main limitation of using MODIS and MERIS data alone. This affects the efficiency of using satellite based tropospheric correction. Using GPS integrated with this data can improve the efficiency of this method.

As an alternative, ground meteorological observations integrated with satellite based products like MODIS/MERIS (water vapour products) can be used instead of only satellite data driven atmospheric correction. With this approach tropospheric error quantification and its removal can be achieved.

The satellites providing the meteorological data must be synchronised with the SAR platforms in order to mitigate the tropospheric effects. One such example is MERIS (Medium Resolution Imaging Spectrometer) and ASAR (Advanced Synthetic Aperture Radar) which share a common platform i.e. ENVISAT. So, the meteorological data from MERIS can be directly used to model and mitigate the tropospheric effects on ASAR. But this is not the same case with all the SAR platforms. Meteorological data parameters like temperature, pressure and humidity are geographically and temporally dynamic.

One such case with RADARSAT-2 satellite is that it doesn't have any synchronisation with meteorological data provider platform. So modelling the atmospheric effects on this kind of platform is a challenge and new approaches have to be adopted to mitigate the tropospheric effects on this satellite data. An integrated approach of both ground meteorological data and satellite data would be the primary study of this research to mitigate the tropospheric effects on DInSAR generated from RADARSAT-2 SLC's.

1.4.2. Ionospheric path delay effects

Ionosphere extends from 70 km upto 3000 km from earth's surface. This layer has electron content which gets ionized by the incoming solar radiation. The refractive index of the RADAR signal in the ionosphere is a function of height and also dependent on the electron density of the medium [15].

The broad context of this research is to study and remove the atmospheric effects on DInSAR phase of RADARSAT-2 SLC's for land subsidence measurements using an integrated approach. This approach is to integrate ground meteorological data and satellite data for mitigation of atmospheric effects.

1.5. Research Identification

Focussing on the research problem mentioned in section 1.3, the research objectives and research questions are framed below to derive the solution.

1.5.1. Main research objective

To explore the tropospheric and ionospheric delays on DInSAR phase using an integrated approach for land subsidence measurements.

1.5.2. Sub-objectives

- To integrate ground based meteorological observations and satellite data for estimating tropospheric phase delay.
- To calculate the ionospheric phase delay from TEC data.
- To quantify and remove the total error due to atmospheric effects.

1.5.3. Research Questions

- What will be the errors induced by tropospheric and ionospheric component on the RADAR signal?
- How can the parameters (temperature, pressure and water vapour pressure) derived from MODIS water vapour products be modeled in synchronization with acquisition time of RADARSAT-2?
- What will be the accuracy of land subsidence measurements after atmospheric correction?

1.5.4. Innovation aimed at

The novelty of this study would be to use an integrated approach of both ground meteorological observations and satellite data to model the atmospheric effects on RADARSAT-2 single look complex (SLC). This approach provides an insight to model the temperature, pressure and water vapour pressure bands for the time of pass of RADARSAT-2.

2. LITERATURE REVIEW

2.1. Introduction

Topographic map generation has been used since many years with the growth of aerial photography and first satellite images [16]. The first satellite remote sensing exploited the visible and infra-red range of the optical spectrum. These techniques were hampered by certain limitations i.e., presence of cloud cover and lack of sunlight in Polar Regions for almost half the year [2]. So these reasons gave way to the development of radar. Topographic measurements using radar has been developed since times which lead to the development of SAR. SAR is a coherent airborne or spaceborne platform which uses the flight path simulating a large antenna to generate high resolution imagery [2]. This technology lead to the launch of many satellite platforms carrying SAR sensors for wide range of applications. SAR systems were unable to distinguish two objects in same range from two different angles. This problem has lead to the idea of using two SAR systems which in turn gave rise to interferometry [2]. Hence, radar uses the technique of SAR to generate high resolution imagery and interferometry to give the third dimension [16].

2.2. InSAR theory

InSAR is a technique where two SAR images are taken with nearly same incident angle. These two images are then combined to generate a phase difference image called interferogram [17]. The main principle of InSAR is to use an additional antenna to measure the phase of a pixel of interest [30]. The Fig.(2-1) below explains the airborne InSAR geometry [30].

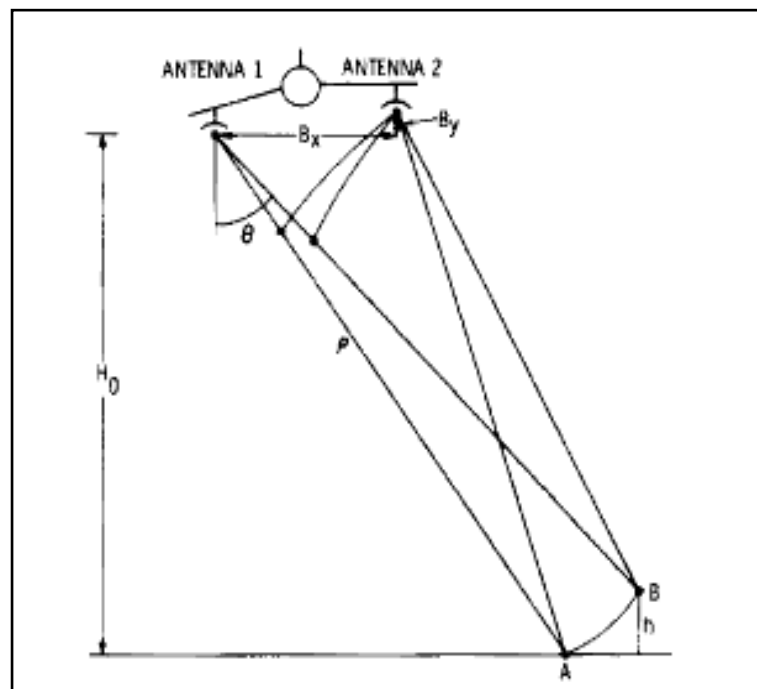


Figure 2-1: Air borne InSAR imaging geometry with two antennae. Source [30]

The Fig.(2-1) illustrates the antennae (1 and 2) are separated by a baseline which is fraction of aircraft dimension. Target points A and B in the fig are in the same slant range to antenna1 and are also in the same relative azimuth position [30]. Thus the topographic height cannot be measured. So the second antenna has been utilized. The phase difference measured between the two antennae (1 and 2) from the Fig.(2-1) will vary for the targets A and B. So, based on the phase differences, the height of the object can be measured for each pixel [30].

The height of the target B with respect to the terrain is calculated as:

$$\Phi = \frac{4\pi}{\lambda} [B_x \sin\theta - B_y \cos\theta] \quad (2.1)$$

$$b = H_0 - \rho \cos\theta \quad (2.2)$$

where

Φ is the phase difference

b is the height of the target B

H_0 is the flying height

ρ is the range from antenna A1 to the point on the ground

θ is the look angle

λ is the RADAR signal wavelength

B_x is baseline length between antenna1 and antenna2

B_y is the vertical distance from intersecting point of horizontal from antenna1 and vertical from antenna2

Based on the phase difference (Φ) and (θ) the off nadir angle. Then the height (b) is computed using eq.(2.2).

2.3. InSAR related work

First experiments of airborne single pass interferometry were started in 1980's by [19] which used coherent multiplicative interferometry. First interferograms were produced by [17]. They generated a topographic map of San Francisco Bay area which was 11 km by 10 km in size. This map had accuracy between 10 m and 30 m.

Repeat pass interferometry was first demonstrated by [1] which utilized SEASAT SAR data. The resulted interferograms depicted the topographic contours of the study area. This paper mainly focused on topographic mapping using repeat pass interferometry. Gabriel and Goldstein [20] performed a cross orbit interferometry where SIR-B orbits were not parallel but inclined at an angle. This was performed in order to reduce the length of the baseline. This method was useful but it had few drawbacks. It was computationally intensive and it required measured or derived knowledge of orbital parameters.

Studies were made by [18] to understand the potential of this technique to produce high resolution topographic maps. With this technique, relative height errors of 5 m or less have been produced using 3 day repeat pass ERS-1 images.

DEM (Digital Elevation Model) is used in applications like topographic mapping, run-off studies, seismic modelling, etc. One of the studies performed by [22] showed that InSAR is a promising

technique in generating good quality DEM's from airborne and space borne data for various applications.

2.4. DInSAR

The early applications of Radar interferometry was topographic mapping. InSAR had become a very effective tool for this application because the relative line of sight movement of point scatterers with respect to reference locations on the image could be measured as a fraction of wavelength. Space borne InSAR has become a widely accepted and effective tool to map surface movements, ground deformations, mining activities and volcano dynamics [21]. This in turn produced cm to mm accuracies for L, C and X band radars [5].

In due course of time and developments in interferometry, many applications took birth. One of the most prominent and effective application was deformation monitoring. When the effective baseline between the image pairs becomes greater than zero, interferometry fails. This was one of the limitation. In this case, the deformation signal was mixed with topographic signal. The solution to this problem was differential interferometry.

The DInSAR technique was first introduced by Gabriel et al. [5] in 1989 for measuring very small surface movements with accuracies up to 1 cm over large swaths. This method was applied to SEASAT data of Imperial Valley, California where ground swelling and shrinking was caused due to water absorbing clays in the area [5].

Three pass DInSAR technique was first introduced by Zebker et al. [18]. This technique uses three images of the same area to generate displacement map of the region. The three pass DInSAR technique described in the paper [18] is shown:

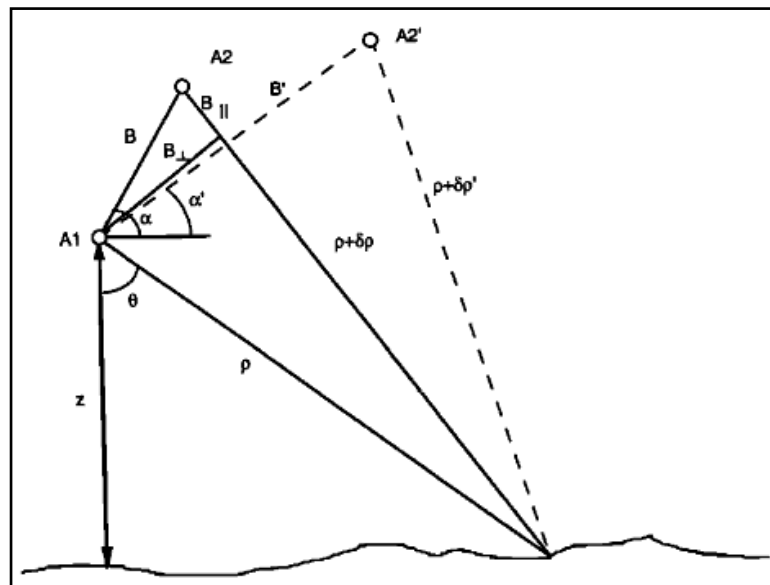


Figure 2-2: Three pass SAR imaging geometry. A1, A2 and A2' are the antenna positions during the three pass acquisitions. The solid black lines are the RADAR signal path of the first interferogram pair formed by A1 and A2. The dashed black lines are the RADAR signal path of the second Interferometric pair formed by A1 and A2'. Source [18]

DInSAR phase equations are explained as:

$$\Psi_1 = \frac{4\pi}{\lambda} \rho \quad (2.3)$$

$$\Psi_2 = \frac{4\pi}{\lambda} (\rho + \delta\rho) \quad (2.4)$$

$$\Psi_3 = \frac{4\pi}{\lambda} (\rho + \delta\rho') \quad (2.5)$$

Where

Ψ_1, Ψ_2, Ψ_3 are the phases measured from A1, A2 and A2' antenna positions to the ground points $\rho, (\rho + \delta\rho)$ and $(\rho + \delta\rho')$.

λ is the RADAR signal wavelength

From the three phase measurements derived, the Interferometric phases are derived as:

$$\Phi_1 = \Psi_1 - \Psi_2 = \frac{4\pi}{\lambda} \delta\rho \quad (2.6)$$

$$\Phi_2 = \Psi_1 - \Psi_3 = \frac{4\pi}{\lambda} \delta\rho' \quad (2.7)$$

From the Fig 2.1. based on the cosine law, the solution for $\delta\rho$ is formulated in [18] as:

$$(\rho + \delta\rho)^2 = \rho^2 + B^2 - 2\rho B \sin(\theta - \alpha) \quad (2.8)$$

where

B is the baseline length

ρ is the range from antenna A1 to the point on the ground

θ is the look angle

α is the angle of the baseline with respect to the sensor horizontal

From the equation, neglecting the $(\delta\rho)^2$ order term, the modified equation turns into:

$$\delta\rho \approx B \sin(\theta - \alpha) + \frac{B^2}{2\rho} \quad (2.9)$$

According to [18] for space geometries, the second term in the eq.(2.9) can be neglected. Hence the equation becomes:

$$\delta\rho \approx B \sin(\theta - \alpha) \quad (2.10)$$

From the Fig.[2.1].

$$B \sin(\theta - \alpha) = B_{\parallel} \quad (2.11)$$

Therefore,

$$\delta\rho \approx B_{\parallel} \quad (2.12)$$

So, the final Interferometric phases are formulised as:

$$\Phi_1 = \frac{4\pi}{\lambda} B_{\parallel} \quad (2.13)$$

B'_{\parallel} is the baseline length of the second Interferometric pair.

Consider the situation when displacement has occurred during the second Interferometric pair acquisition. Hence in addition to the topographic phase, an additional phase change due to displacement in the RADAR line of sight is also present [18]. So the second Interferometric phase is represented as:

$$\Phi_2 = \frac{4\pi}{\lambda} (B'_{\parallel} + \Delta\rho) \quad (2.14)$$

where, $\Delta\rho$ is the additional displacement component

From the eq.(2.13) and (2.14), the deformation component is derived as:

$$\Delta\rho = \frac{\lambda}{4\pi} (\Phi_2 - \frac{B'_{\parallel}}{B_{\parallel}} \Phi_1) \quad (2.15)$$

This technique [18] was applied to the co-seismic displacement occurred due to an earthquake in Landers, California in 1992. In this study the comparison of displacement map generated had a correlation of 0.96 with GPS and EDM survey measurement data.

Later, differential interferometry was applied using German Aerospace Centre (DLR) E-SAR L-Band data by Reigber [23]. In this study, the differential interferogram of agricultural and forested areas was presented. The study showed that using L-Band data could preserve coherence in vegetated areas even after a year.

Another study by [24], the potential of L-Band DInSAR was evaluated by using Japanese Earth Resources satellite (JERS) data. As compared to ERS C-band SAR data, L-band interferometry could retrieve the subsidence values over vegetated and forest areas for less than one year time interval and small baseline. In this study it was also concluded that areas with large deformation gradients, L-Band was superior to C-Band interferometry. C-Band interferometry had phase unwrapping problems.

In a paper by Herrera [25], an advanced technique in DInSAR called the Coherent Pixels Technique (CPT) has been used to study the subsidence phenomena. It was taken for two time intervals, from January 1998 to December 2000, and from March 2003 to December 2004. The results derived using technique has shown good agreement with topographic levelling data. The absolute differences w.r.t. topographic levelling data vary from 0 to 1.9 cm from July 1994.

A technique in order to generate the topographic phase removed sample coherence also called as differential coherence has been proposed. It was proposed by Lee and Liu [26]. It was applied on ERS-1, 2 SAR data of Grenada, Spain. This technique showed improvement in coherence in terrain slopes.

Repeat pass interferometry had certain limitations like temporal and geometric decorrelation. These limitations often hinder the performance of interferometry for surface deformation monitoring. Temporal decorrelation makes the Interferometric measurements unsuitable over vegetated areas. So Permanent Scatterers (PS) technique has been implemented to identify coherent pixels over long time [27]. Identifying these PS have improved the coherence for interferogram having larger baselines and this also lead to make use of all the data pairs for interferometry [27].

DInSAR technique was applied to identify urban land subsidence in Jakarta. The work was carried out by Bayuaji et al. [29] during the years 2007 and 2008. ALOS PALSAR L-Band data was used for three dates in 2008. The subsidence was successfully estimated and validation with ground based GPS data showed good results [29].

Later mining area subsidence was monitored using multi-band SAR data [28]. In this paper DInSAR technique was applied to C-Band ENVISAT ASAR data and L-Band JERS SAR and ALOS PALAR data of Fengfeng coal mine area in china. The study showed that both C-band

and L-Band can be used to monitor land subsidence. It was also observed that the deformation pattern obtained by both bands data were not uniform [28].

With the wide applications of InSAR and DInSAR in the field of topographic mapping and deformation monitoring, yet there have been limitations. One of such limitation is the refractive effect of atmosphere on the RADAR signal which leads to additional path delay on the phase of the interferogram. Many researchers have taken efforts to minimise the effect of atmosphere on the interferogram to improve the accuracy of measurements.

2.5. Atmospheric effects on RADAR interferometry

Interferometry is a powerful tool in measuring the topography. These measurements are however affected by the atmospheric effect on the RADAR signal during its propagation. Troposphere and ionosphere are the main layers of the atmosphere which cause the propagation delay and bending of the RADAR signal [4].

The atmospheric effects on interferograms were first observed by Goldstein et al. [14]. Over years, many research works have been done to understand the atmospheric effects on the RADAR signal. Various studies were performed to understand and mitigate the atmospheric effects which are discussed in the next section(2.5.1).

2.5.1. Tropospheric effects on RADAR interferometry

Tropospheric effect on the interferometry is mainly caused due to the change in refractive index of the medium [4]. Troposphere is the lowest portion of atmosphere extending up to 50 km from earth's surface. It comprises of 99% water vapour and aerosols. Temperature, atmospheric pressure and humidity are the main gradients which affect the RADAR signal during its propagation through this layer.

First atmospheric artefacts on interferograms were observed by Goldstein et al. [14]. The expedition carried out by SIR-C was on repeat track interferometry. The results concluded that the tropospheric turbulence including the water vapour content was the reason for the lack of accuracy in motion detection. They recommended that interferometry performed with two antennas may show better results.

A study by Tarayre and Massonnet has revealed that atmospheric heterogeneities can be revealed using RADAR interferometry [31]. ERS-1 data was used for the study. The study showed that the effects of pressure and temperature are smaller in magnitude as compared to water vapour. These effects were also evenly distributed through the interferogram [31]. It is sometimes difficult to distinguish these errors from orbital uncertainties [31]. The study also emphasised that RADAR interferometry can be used as a tool to investigate the tropospheric and ionospheric turbulences.

Water vapour which extends up to 2 km above the ground is the main reason for spatial heterogeneity in refractivity. This spatial heterogeneity is caused by mixing process of the water vapour which in turn causes localized phase gradient in flat as well as mountainous regions [2].

Water vapour being the strong parameter for tropospheric path delay, but in regions with more topographic changes, atmospheric pressure changes can lead to larger tropospheric path delays

than water vapour and humidity [4]. One study by Hanssen, based on the liquid water content in the clouds, the zenith propagation delay has been computed [32]. The clouds have been classified into three types in this study namely, stratiform, cumulus and ice clouds. The study has derived that the stratiform and ice clouds do not contribute to large phase disturbances because of their large horizontal extent [32]. The cumulus type of clouds contribute to significant zenith delay about 0.7-3 mm/km because of their limited horizontal extent in contrast to large vertical height and water content [32].

Modelling approaches have been developed by Saastamoinen [33] based on ground measurements and their algorithms are till date valid for measurement of delays. He has also recommended that geographic latitude of the station and also station height should be taken in account for improving the accuracy. An expert system modelling approach was developed by Nahvi [34] for further improvement of the atmospheric delay corrections. A total of about 535 radiosonde measurements of different parameters like pressure, temperature and dew point depression were taken within a time span of 3 years in Sweden. Here he emphasized that a relational database can be generated from historical meteorological data over time scale to generate models that could reduce the tropospheric error.

In 1997, Zebker et al. proposed to use the Saastamoinen model to assess the tropospheric path delay on InSAR measurements [9]. This model used ground meteorological data to assess the tropospheric path delay. In this study, SIR-C data of Hawaii was used. Tropospheric path delay estimation was the main motive of the research..The Earth's atmosphere is spatially inhomogeneous having a higher refractive index than free space. So the RADAR signal propagating through this medium will have a decrease in velocity contaminating the measurements [9]. The basic theory used in this study [9] is shown as:

For any signal propagating through free space, the phase shift (Φ) is represented as:

$$\Phi = \frac{2\pi}{\lambda} x \quad (2.16)$$

where x is the distance propagated

λ is the signal wavelength

when the signal propagates through the atmosphere, the phase shift equation turns into:

$$\Phi = \frac{2\pi}{\lambda} x + \frac{2\pi}{\lambda} \Delta x \quad (2.17)$$

where $\Delta x = 10^{-6} N(x)x$ is the additional path length cause due to earth's atmosphere

$N(x)$ is the additional refractive index caused due to atmosphere

Δx is separated into two components as follows:

$$\Delta x = (\Delta x)_{dry} + (\Delta x)_{wet} \quad (2.18)$$

where

$(\Delta x)_{dry}$ is the contribution due to hydrostatic component

$(\Delta x)_{wet}$ is the contribution due to water vapour and clouds

$$\Delta x = 77.6 \times 10^{-5} \int_0^X \frac{P}{T} dx + 3.73 \times 10^{-1} \int_0^X \frac{e}{T^2} dx \quad (2.19)$$

where X is total path length through the atmosphere

P is atmospheric pressure in millibars

T is temperature in Kelvin

e is the partial pressure of water vapour in millibars

This study [9] also revealed that 20% spatial or temporal change in humidity can lead up to 10-14 cm deformation measurement errors.

Many researchers [8,9,33,34] had assessed the tropospheric path delays using ground meteorological data. There were difficulties in using ground based meteorological data because of poor accuracies of atmospheric correction and also non-spatial nature of the data.

Advancements in space technology like the launch of GPS satellites and the availability of satellite-based meteorological data like MODIS (Moderate Resolution Imaging Spectroradiometer) and MERIS (Medium Imaging Resolution Spectrometer) water vapour, surface pressure and LST have added cream to assess the atmospheric effects. Li et al. developed an integrated use of continuous GPS and ground meteorological observations to model and correct the atmospheric effects [35]. This model utilized spatial relationship between the two data and also included the elevation. The resulted RMS error of total zenith delay using this approach was in the order of 0.5 cm in contrast to 4 cm in using meteorological data only. One of the potential limitations of using GPS data is that the spatial resolution of the GPS stations distributed is in general lower than that of InSAR data. The reason is that GPS delivers point-based observations as compared to spatial observation in case of InSAR.

Numerical meteorological modelling was used to model the tropospheric path delays [4]. These modelling approaches were done on Global, Regional and Mesoscale. The global and regional models were too coarse to assess the tropospheric effects. One of the studies used mesoscale forecast model, Unified Model (UM) for computing atmospheric delay [36]. The UM is used by Met Office to produce numerical weather predictions at global scale with 60 km cell size. This study utilized the UM to simulate the atmosphere at higher resolutions i.e., at 12, 4, 1 and 0.3 km. This 60 km prediction is simulated to the nested domains from which temperature, pressure, water vapour and humidity are computed for the RADAR satellite acquisition time. This technique showed promising results as compared to GPS and meteorological data. They concluded that this model is suited to high relief regions and specific targets.

MODIS near-IR water vapour products has a spatial resolution of 1 km \times 1 km. The MODIS water vapour retrieval algorithm showed error of derived water vapour values in the range between 5% and 10% [37]. Li, first used MODIS water vapour data integrated with GPS to reduce the water vapour effects on the interferograms [38]. This integrated approach not only helped reduce the water vapour effect but also helped to discriminate the geophysical signal from the atmospheric signal [38]. MODIS PWV (Precipitable Water Vapour) products are sensitive to clouds. This is the main limitation in using MODIS data in cloudy regions.

A case study was performed in China using ENVISAT ASAR products in which the atmospheric effects on small baseline subset DInSAR was calibrated for land subsidence monitoring application. The phase delay was computed using MODIS data for the tropospheric wet component and this was removed from the interferogram phase [40].

Balaji [39] studied estimation and correction of tropospheric and ionospheric effects on DInSAR interferograms. The data used was ALOS PALSAR (L Band) SLC. The tropospheric correction was done using MODIS cloud product and the ionospheric correction was done using vertical TEC data from CODE (Europe). The main focus of the work was to study the atmospheric propagation effects on the interferogram phase and to remove the error induced by them. Baseline decorrelation effects have not been considered and even phase unwrapping were not done in this study. The study area showed no displacement between the time period. The atmospheric errors were quantified and showed.

MERIS which is on board ENVISAT has two infrared water vapour channels which retrieve global PWV every three days [4]. It acquires water vapour data together with ASAR on board ENVISAT which in turn helps to accurately model the atmospheric effects on ASAR. The resolution of MERIS is $300\text{ m} \times 300\text{ m}$ which is higher than MODIS. In a recent paper by Li et al. MERIS data along with an elevation dependent interpolation model was used to model the atmospheric artefacts on the interferograms of ENVISAT ASAR data [13]. The ASAR data was acquired from 2004 to 2009. The accuracy of this method is assessed with GPS data. After the correction, the R.M.S (Root Mean Square) differences between InSAR measurements and GPS data decreased by 69.4%, 29%, 31.8% and 23.3% for four pairs of selected interferograms [13]. This study also recommended the use of GPS meteorological data or other meteorological measurements along with MERIS water vapour data.

One of the studies on correlation analysis by Chabane [41] concludes that this analysis is advantageous and no external data (GPS, meteorological, etc) is needed. This analysis depends on the correlations between the deformations and between the atmospheric signals in different interferograms. Atmospheric effect removal is not sufficient if the correlations are weak. This is one of its limitations.

2.5.2. Ionospheric effects on RADAR interferometry

The ionosphere is located at height of about 50 km – 1500 km from the earth's surface. The presence of free electrons and ions in this region is the main cause of refractivity of the RADAR signal propagating through this region [41]. The degree of ionization in this medium mainly depends on the incoming solar UV radiation.

The TEC (Total Electron Content) is the number of free electrons in a column of 1 m^2 along the RADAR signal path [41]. TEC is usually in the order of 10^{16} electrons per m^2 . TEC varies from day to night i.e., TEC is usually low at night and high at noon. The dispersive nature of the medium can be used to estimate the TEC along the RADAR signal path [41]. The electron density in ionosphere varies seasonally and geographically.

Various approaches have been made to understand and mitigate the ionospheric effects on the interferograms. Since ionosphere is a dispersive medium, these effects on the interferogram can be distinguished from the non-dispersive effects of deformations and the atmosphere [42]. A multi-frequency split spectrum processing technique has been introduced to study the

ionospheric effects on InSAR data [42]. This technique showed promising results for L-Band SAR data.

Another technique is to derive the global TEC map using GPS. Then this map can be used to generate the ionospheric phase delay. Daily global TEC maps are generated by CODE (Centre for Orbit Determination in Europe). The global ionospheric maps (GIM'S) are generated from the GPS tracking data using the doubly differenced carrier phase measurements [43].

Based on the equation derived by Hanssen [2], Jehle used this ionospheric model to estimate the effect of ionosphere on C-Band ENVISAT ASAR scenes. This study used the TEC from GIM's generated by CODE and the path delay was estimated using the following equation:

$$\Delta\psi_{\text{iono,SAR}} = 2K \cdot \frac{TEC}{f^2 \cdot \cos \alpha} \quad (2.20)$$

where

$(\Delta\psi_{\text{iono,SAR}})$ is the phase shift

K is refractive constant which is $40.28 \text{ m}^3 \text{ s}^{-2}$

f is the frequency of the RADAR signal

α denotes the satellite incidence angle

One of the empirical model's namely the IRI (International Reference Ionosphere) was started by the Committee on Space Research (COSPAR) and by the International Union of Radio Science (URSI) during 1960's. The goal of this model was to establish an international standard for the specifications of ionospheric parameters. These parameters were based on experimental observations of the ionospheric plasma either by ground or in-situ measurements [44]. The IRI model gives the electron density, electron content, ion temperature and ion composition in the vertical range of 60 km to 2000 km. This model derives the TEC by numerically integrating the electron density profiles in the altitude range [44]. The IRI model is continuously upgraded based on the new data added and also the modelling approaches [45].

One of the studies which showed the comparison between the GPS derived TEC and IRI derived TEC was done by Okoh et al. in 2012 [45]. The results show that the IRI TEC values compared with the GPS TEC values showed correlation coefficients about 0.9, and the rms deviations were generally around 20–50% for diurnal comparisons.

3. STUDY AREA

The study area chosen for this work is Jharia Coalfield of Jharkhand state in India. It is located in the eastern India between latitudes $23^{\circ} 30' N$ and $23^{\circ} 55' N$ and longitudes $86^{\circ} 10' E$ and $86^{\circ} 30' E$. It covers an area of about 450 km^2 . Dhanbad is the major city which is located near the study area.

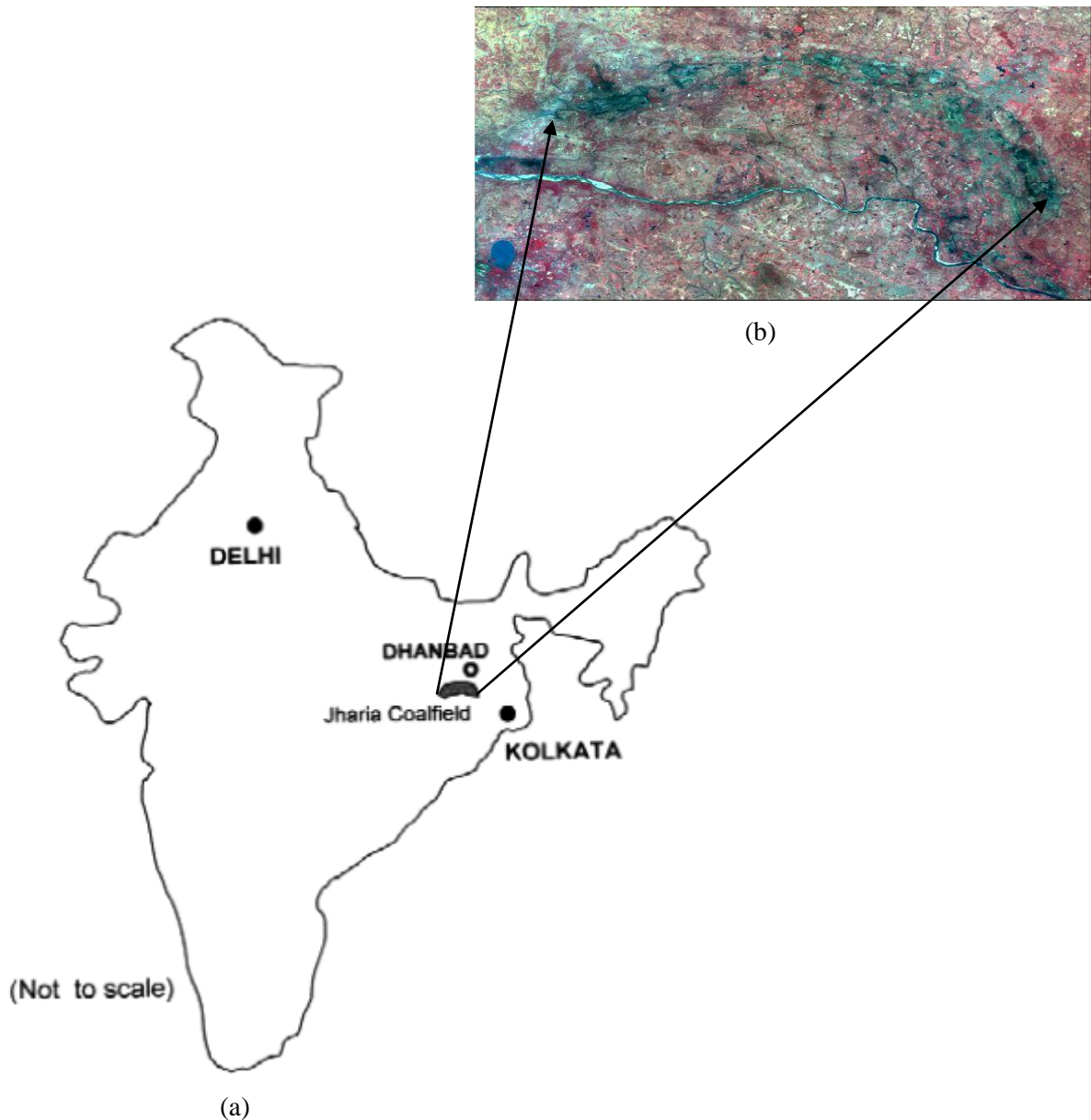


Figure 3-1(a): Geographical position of the study area (Dhanbad) in India

Figure 3-2(b): Cartosat-1 PAN sharpened LISS-IV image of the study area.

3.1. Justification of choice of study area

Coal mining was started in Jharia Coalfield in the early 1890's [49]. Jharia coalfield was one of the best for mining because it had several thick coal seams which were at relatively shallow depths beneath the surface. It was proven that the crescent shaped basin of the coal field has approximately 1 billion tonnes of coal reserves [49]. Coal is the primary source of energy in India. Mining in this coalfield was started 100 years ago approximately and is still continuing. Bharat coking coal limited (BCCL) is the primary mining agency in this area and it supplies about 40% of nation's coking coal.

Attributes of the study area:

1. Jharia coal field consists of mainly sedimentary rocks.
2. Damodar is a major river which flows in the south of this coal field.
3. This coal field has more than 100 coal mines.
4. There are many underground mines in the coalfield. But, major mining activity is done by opencast mining method.
5. Dense population over underground mining areas and in affected areas is high which approximates to 1.1 million.
6. This coal field has three main coal formations namely Barakar, barren measures and Raniganj formations. Barakar and Raniganj formations are coal bearing but Barren Measure lacks coal deposit

The uniqueness of this coal field is not only in its geologic formation and being primary coking coal reserve but also in land degradation, mine fires and also in environmental pollution. It is considered to be one of the world's most degraded coal field [49].

Land degradation in this coal field is mainly due to mining activities, abandoned quarries, overburden dumps, degraded vegetation and mining fires. Land subsidence is one of the major considerations of land degradation in and around this coal field.

This coal field is much degraded and it exhibits severe environmental problems in land, air and water [49].

It is evident that different types of scatterers are found in this study area. The buildings and other urban features in and around Dhanbad city and other villages act as permanent scatterers. The water bodies like Damodar River in the south of the study area causes specular reflection to the RADAR signal. The vegetation in this region acts as volume scatterers. The terrain in this region is continuously changing with time due to mining activities. Interferometric pairs with low temporal baselines over this study area would be feasible to get accurate deformation measurements.

4. MATERIALS AND METHODS

The methodology applied to this study is briefly described through the flow chart:

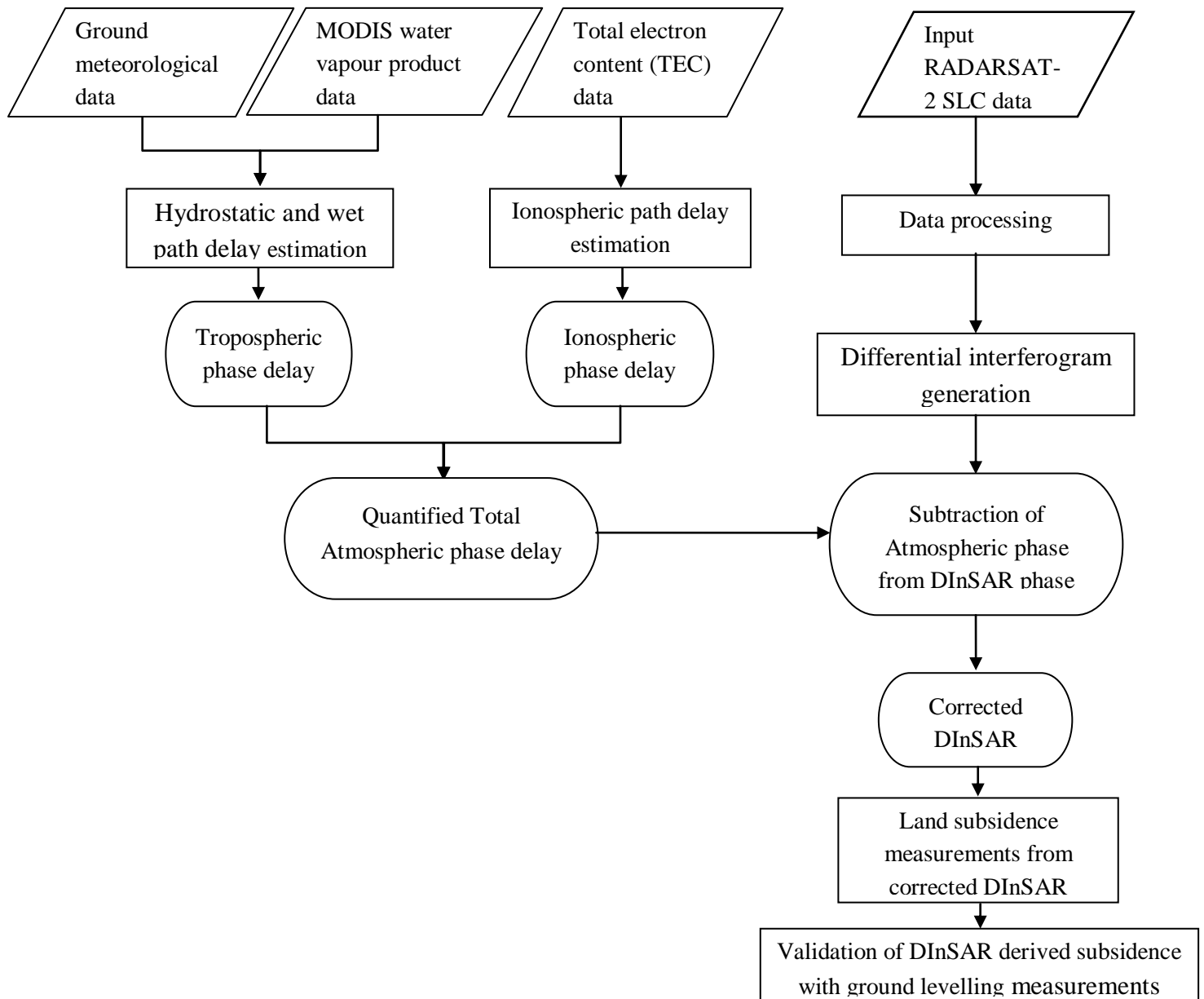


Figure 4-1: Flow chart of Methodology

4.1. Materials used in the study

4.1.1. MODIS data

MODIS sensor has two platforms namely Terra and Aqua which provide daily coverage of the Earth. For any location on the Earth, the images from these sensors can be available for morning and evening.

MODIS sensor specifications are mentioned in brief:

- MODIS operates in a sun-synchronous near polar orbit approximately 705 km above the surface.
- It is a 36 band Spectroradiometer.
- MODIS products are available in three different resolutions i.e., 250 m (bands 1-2), 500 m (bands 3-7) and 1000 m (bands 8-36).
- Swath dimensions are 2330 km (cross track) by 10 km (along track at nadir).

MODIS product used in this study and its specifications are as follows:

- MODIS/Terra Temperature and Water vapour product (MOD07_L2).
- MODIS/Aqua Temperature and Water vapour product (MYD07_L2).
- Processing level of these products is Level 2 (L2).
- Data downloaded website: <https://reverb.echo.nasa.gov/reverb/>
- MODIS version: V5.
- The MODIS files are in Hierarchical Data Format-Earth Observation System (HDF-EOS) format.

The downloaded MODIS data were extracted and projected using MODIS Conversion Toolkit (MCT) in ENVI 5.0 software. These HDF format files were converted into .img(IMAGE file format) files and projected to WGS-84 datum and UTM 45 N projection. The study area lies in the 45 N zone of UTM projection. The temperature, pressure and Precipitable water vapour content bands were extracted from the MOD07 HDF file.

Temperature band units in °K (physical values 150 to 350 °K)

Pressure band units in hPa (physical values 800 to 1100 hPa)

Precipitable water vapour content band units in cm (physical values 0 to 20 cm)

4.1.2. Ground meteorological data

Automated Weather Station (AWS) is used to collect the ground meteorological observations for the study area. The AWS records the values of temperature, pressure, humidity, wind speed, wind direction, rain rate and solar rate. The AWS is a combination of anemometer, rain gauge and sensors for measuring temperature and pressure. The AWS data can be recorded in specified time interval. This instrument has been placed in the field to continuously record the readings of the meteorological parameters. The data is stored in a text document which can be used for further analysis.

4.1.3. Total Electron Content (TEC) data

Total Electron Content (TEC) data is used to calculate the ionospheric path delay. The TEC data was derived from the IRI-2007 model. The TEC values from IRI-2007 model were obtained for height of 800 km above the earth's surface. This was used because RADARSAT-2 orbit height is approximately 798 km above the earth's surface.

4.1.4. SAR data

RADARSAT-2 single look complex (SLC) SAR data are used in this study for DInSAR processing. Three SLC data sets were procured for this study. The specifications of SAR data used in the study are mentioned below:

Table 4-1: RADARSAT-2 SLC data specifications

RADARSAT-2 SLC			
Data Type	Single look complex	Single look complex	Single look complex
Satellite name	RADARSAT-2	RADARSAT-2	RADARSAT-2
Acquisition mode	Standard Beam	Standard Beam	Standard Beam
Polarization	HH	HH	HH
Incidence angle (deg)	27.5	27.5	27.5
Orbit number	25202	25888	26231
Date of acquisition	12-10-2012	29-11-2012	23-12-2012
Time of acquisition (UTC)	00:17:04	00:17:03	00:17:01
Pulse wavelength (cm)	5.6	5.6	5.6

The SLC images were subset as per the study area.

The extents of the subsets are shown below:

Table 4-2: Dataset extent

Position	Latitude	Longitude
Top Left corner	23° 53'46.507" N	86° 6'39.515" E
Top Right corner	23° 48'44.512" N	86° 33'27.707" E
Bottom Left corner	23° 40'8.214" N	86° 3'34.319" E
Bottom Right corner	23° 35'4.309" N	86° 30'25.166" E

4.1.5. Digital Elevation Model (DEM)

A combined CARTOSAT and SRTM (Shuttle Radar Topographic Mission) Digital Elevation Model (DEM) of 10 m resolution. The vertical accuracy is 8 m and the horizontal accuracy is 15 m.

4.1.6. Subsidence data obtained from ground levelling

Two test sites namely Maheshpur and Bastacolla are considered in this study for validation of subsidence measurements. The test sites have pillars established which are 14 m from each other. The benchmark of each pillar was taken when the pillars were first established. Then onwards the levelling is done every month for the pillars. The subsidence is deduced by subtracting the present height of the pillar with respect to the previously recorded height. The levelling data shows the subsidence of individual pillar for the time interval during which levelling was performed. The pillars do not have spatial coordinates. Points surrounding the test sites were taken with hand held GPS (horizontal accuracy about 6 m).

4.2. Field Work

Since, the MODIS data were not in synchronisation with that of RADARSAT-2 time of acquisition, the method of integrated approach was proposed. In this approach, the readings from AWS and MODIS will be compared, analysed and modelled to generate the temperature, pressure and water vapour pressure bands for the time of acquisition of RADARSAT-2. The RADARSAT-2 acquires at 05:47 AM IST (Indian Standard Time) which is minimum 5 hours away from any MODIS data product. So, the field work was planned and executed in the following manner:

Ground meteorological data collection in October:

For October 12th, 2012 RADARSAT-2 SLC data, the field meteorological data collection was carried out from 11-10-12 (05:37) till 13-10-12 (13:40). The meteorological observations were collected for an interval of 1 min. For the same time period, MOD07 water vapour products were downloaded. There were a total of 8 datasets including both Terra and Aqua passes for the same time period of ground meteorological collection. The temporal variability of temperature, pressure and humidity was recorded in the time frame planned. The behaviour of these meteorological parameters from the weather station are shown :

Temperature (T) plot:

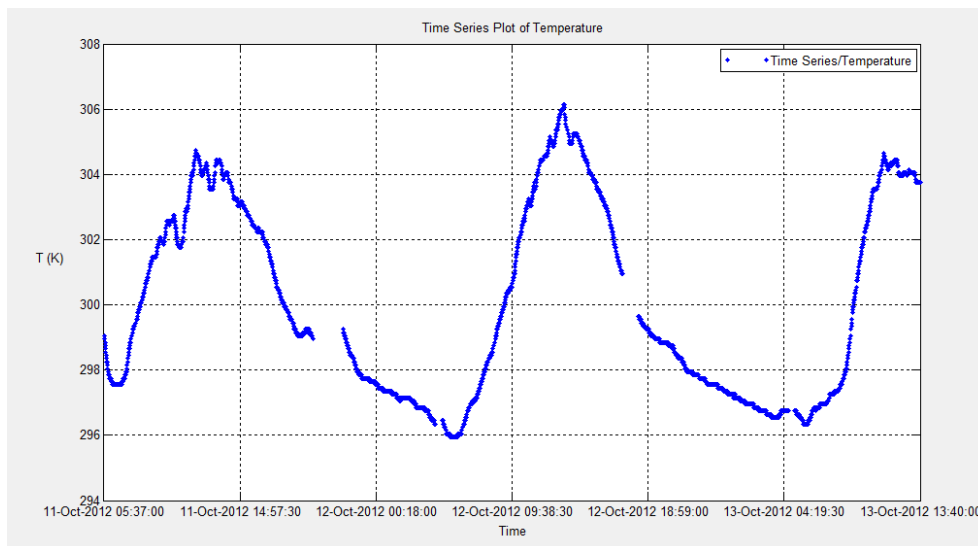


Figure 4-2: Temperature plot of October

Pressure (P) plot:

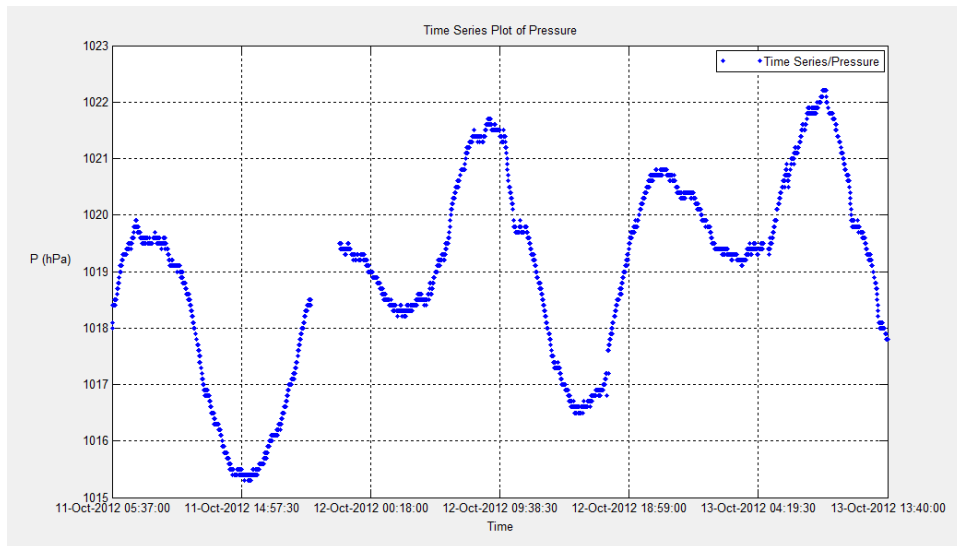


Figure 4-3: Pressure plot of October

Humidity (H) plot:

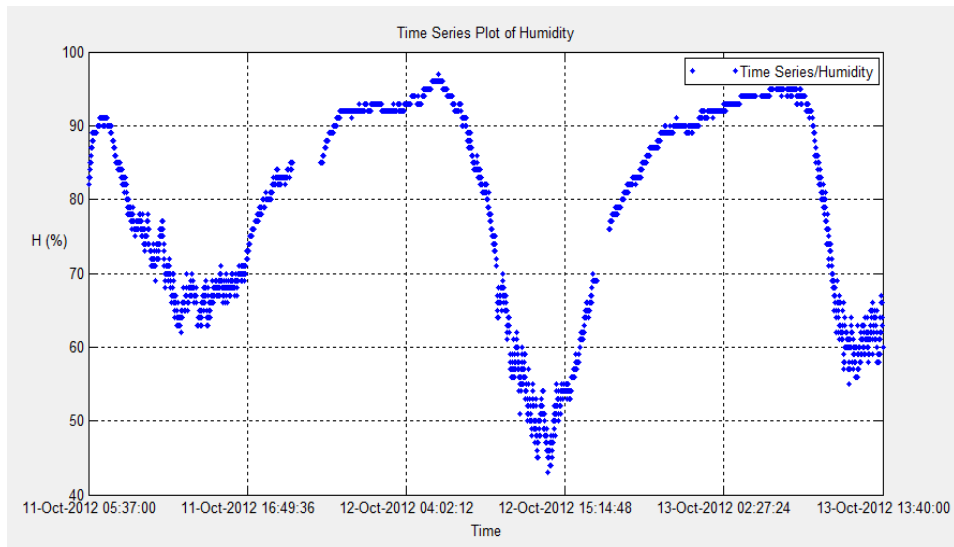


Figure 4-4: Humidity plot of October

The missing data values in the plot are because of non recording of the data due to instrument shift. The time scale on the X-axis is plotted with an interval of 1 min since the weather station readings have been recorded every 1 min.

Ground meteorological data collection in November:

For November 29th, 2012 RADARSAT- 2 SLC data, the field meteorological data collection was carried out from 26-11-12 (13:29) till 02-12-12 (09:02). The ground meteorological data archival interval was increased than the previous month. This was done in order to better analyse the data since more MODIS products will be available to compare with the Weather Station readings. AWS readings were collected for an interval of 1 min.

For the above mentioned time interval, 20 MODIS water vapour products of both Terra and Aqua passes were downloaded for analysis. The temporal variability of temperature, pressure and humidity was recorded in the time frame planned. The behaviour of these meteorological parameters with respect to the weather station is shown:

Temperature (T) plot:

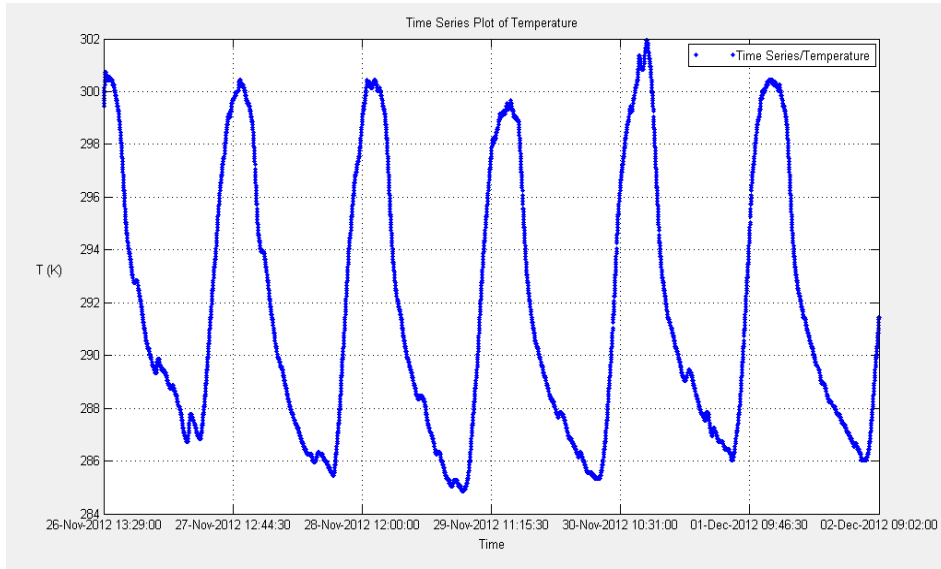


Figure 4-5: Temperature plot of November

Pressure (P) plot:

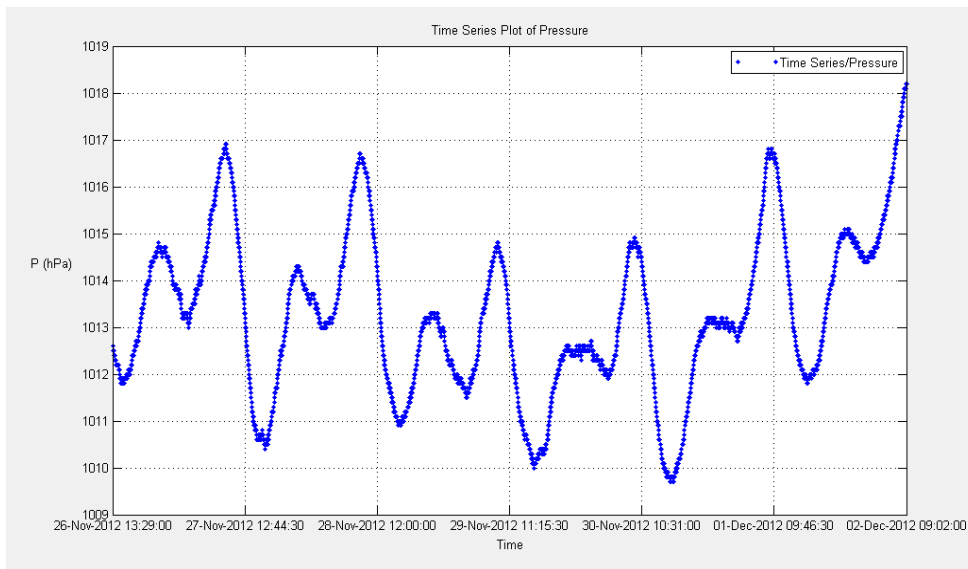


Figure 4-6: Pressure plot of November

Humidity (H) plot:

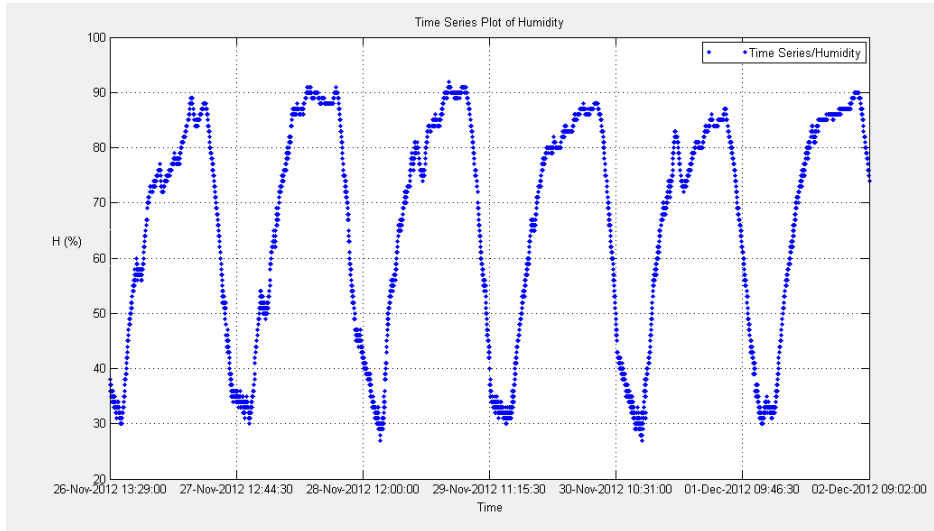


Figure 4-7: Humidity plot of November

Ground meteorological data collection in December:

For December 23rd, 2012 RADARSAT-2 SLC data, the field meteorological data collection was carried out from 20-12-12 (13:22) till 25-12-12 (17:30). The AWS readings were collected for an interval of 1 min.

For the above mentioned time interval, 20 MODIS water vapour products of both Terra and Aqua passes were downloaded for analysis. The temporal variability of temperature, pressure and humidity was recorded in the time frame planned. The behaviour of these meteorological parameters with respect to the weather station is shown:

Temperature (T) plot:

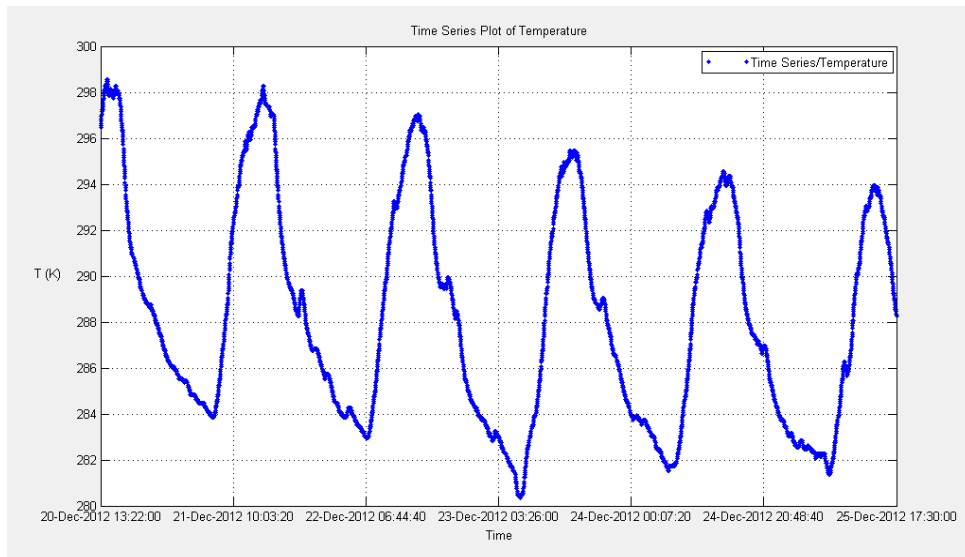


Figure 4-8: Temperature plot of December

Pressure (P) plot:

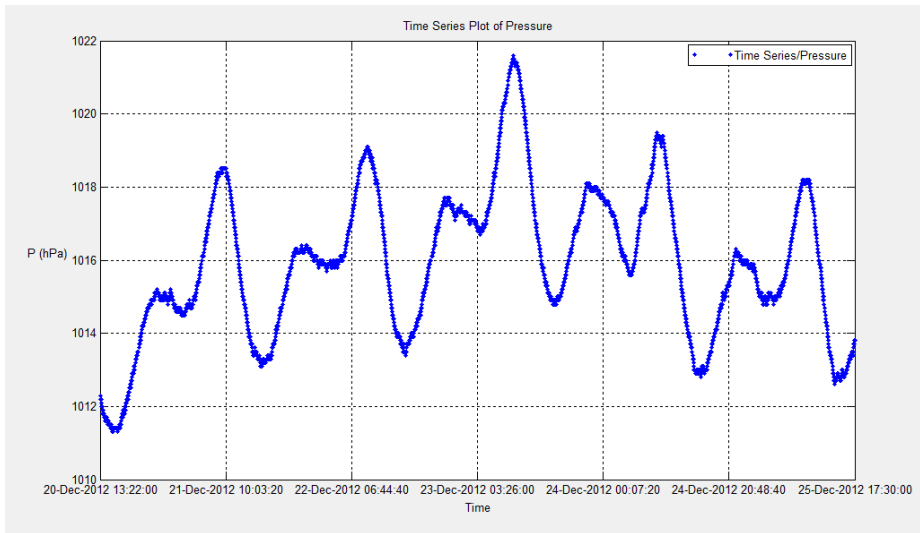


Figure 4-9: Pressure plot of December

Humidity (H) plot:

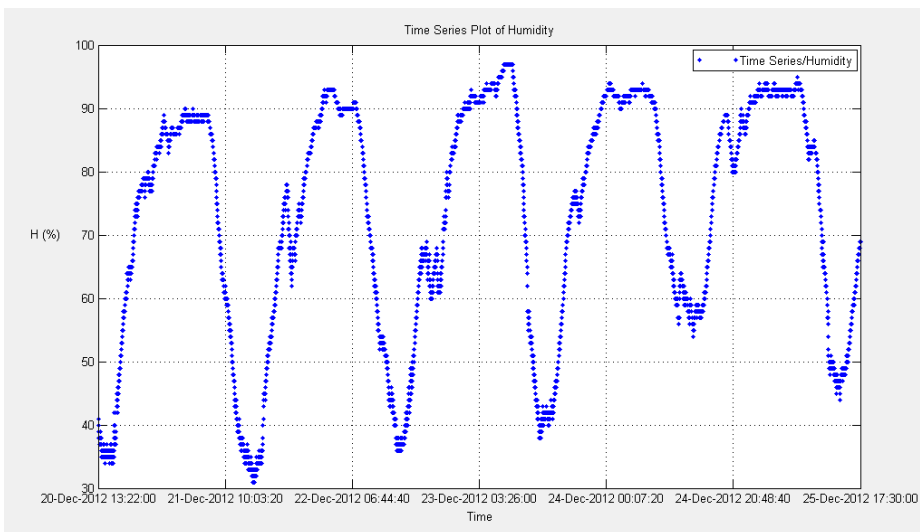


Figure 4-10: Humidity plot of December

These meteorological parameters namely temperature and pressure values have been compared with the temperature and pressure values derived from MODIS water vapour product. The comparison was performed by taking direct measurements from both weather station and MODIS and plotting them on the same time scale and measurements were plotted. For the same time of the day, the weather station values are compared with the MODIS derived values and a regression analysis is performed to define a relation between weather station derived parameters and MODIS derived parameters. After the establishing the relation, the MODIS temperature and pressure bands would be modelled for the time of acquisition of RADARSAT-2 i.e, the value of MODIS at the time of acquisition of RADARSAT-2 will be predicted using the relationship defined by the best fit curve. The water vapour pressure band would be derived directly using the

temperature and humidity value from the weather station at the time of acquisition of RADARSAT-2. These modelled bands would be used as input to tropospheric path delay computation.

4.3. Atmospheric path delay computation

Atmosphere has many layers starting from troposphere to exosphere in the ascending order of distance from earth's surface. Troposphere and ionosphere are the main layers in the atmosphere which affect the RADAR signal. Troposphere is the lower most layer of the earth's surface extending up to 50 km. The presence of gases, water vapour and clouds in troposphere cause the RADAR signal to undergo propagational path delay. The presence of free electrons or ions in the ionosphere is the main cause of propagational delay through ionosphere. These layers have different refractive indices which is the main reason for the propagational delay of the RADAR signal. Tropospheric and ionospheric path delays computation is dealt in this section individually as:

4.3.1. Tropospheric path delay

Tropospheric path delay is mainly caused by the variations in refractive index (n) [41]. This refractive index is a function of air pressure(P), temperature(T), and water vapour pressure(e) [41]. The phase error depends on the atmospheric refractivity based on the height of these parameters above the earth surface in clear sky conditions[12]. These parameters vary with height above the earth's surface.

According to [33], the total tropospheric delay ($\Delta\psi_{\text{tropo},\text{SAR}}$) is separated in terms of their hydrostatic ($\Delta\psi_{\text{hydro},\text{SAR}}$), wet ($\Delta\psi_{\text{wet},\text{SAR}}$) and liquid components ($\Delta\psi_{\text{liq},\text{SAR}}$).

$$\Delta\psi_{\text{tropo},\text{SAR}} = \Delta\psi_{\text{hydro},\text{SAR}} + \Delta\psi_{\text{wet},\text{SAR}} + \Delta\psi_{\text{liq},\text{SAR}} \quad (4.1)$$

The hydrostatic component in this context refers to the standard atmosphere. The wet and liquid components refer to the difference between the standard and actual atmosphere [41].

Standard atmosphere is hypothetical assumption which is devoid of dust, clouds and water vapour. The actual atmosphere refers to the total profile of the troposphere including the clouds and water vapour.

The wet component refers to the water vapour content and the liquid component refers to the water content i.e. cloud droplets, rain, etc. The wet component is highly variable due to the changes in the atmospheric water vapour. The contribution of rain and cloud droplets to path delay is in the order of mm to cm [41], to be specific typical contribution of rain is 6 mm and cloud droplets is <1 mm at C Band[12]. So the liquid component is generally neglected in SAR applications.

So eq. (4.1) is modified to

$$\Delta\psi_{\text{tropo},\text{SAR}} = \Delta\psi_{\text{hydro},\text{SAR}} + \Delta\psi_{\text{wet},\text{SAR}} \quad (4.2)$$

According to Hanssen [2], $\Delta\Psi_{\text{hydro, SAR}}$ can be modeled as

$$\Delta\Psi_{\text{hydro, SAR}} = 2 \times 10^{-6} k_1 \frac{R_d}{g_m} P_s \quad (4.3)$$

Where

$g_m [\text{ms}^{-2}]$ is the acceleration due to gravity

$k_1 = 77.6 \text{ K mbar}^{-1}$ is the refractive constant

$R_d = 287 \text{ J K}^{-1} \text{kg}^{-1}$ is the gas constant

$P_s [\text{mbar}]$ is the surface air pressure

According to [2], with the value of surface air pressure, the hydrostatic delay can be predicted with an accuracy of 1 mm using the equation(4.3).

Most of the models used for wet path delay have not been as good as that of hydrostatic path delay. We used one model approach developed by Askene and Nordius [10].

$$\Delta\Psi_{\text{wet, SAR}} = 10^{-6} \cdot \left(\frac{(k'_2 T_m + k_3) R_d e_0}{T_0 (g_m (\lambda + 1) - \beta R_d)} \right) \cdot k_{\text{wet}} \quad (4.4)$$

and

$$k_{\text{wet}} = \left(1 - \frac{\beta h}{T_0} \right)^{\frac{(\lambda+1)g_m}{\beta R_d} - 1} \quad (4.5)$$

where

$k'_2 = 23.3 \text{ K mbar}^{-1}$ is a refractive constant.

$k_3 = 3.75 \times 10^5 \text{ K}^2 \text{mbar}^{-1}$ is a refractive constant

$\beta = 6.5 \text{ K km}^{-1}$ is the temperature lapse rate

$T_0 [\text{K}]$ is the mean temperature above sea level

$e_0 [\text{mbar}]$ is water vapour pressure above sea level

$T_m [\text{K}]$ is mean temperature of water vapour

$h [\text{Km}]$ is the target's height

λ [unitless] is average decrease of water vapour

The parameters β, T_0, e_0, λ are modeled using latitude and height of the station [41].

The values of zentihal tropospheric delay must be converted into slant range geometry in which he RADAR signal propagates. So the zentihal tropospheric delay is converted into slant range.

The slant range propagation is calculated as

$$\Delta\Psi_{\text{tropo, SAR}} / \cos \alpha \quad (4.6)$$

where

α denotes the satellite off nadir angle.

4.3.2. Ionospheric path delay

Ionosphere is a part of the atmosphere located at a height of about 50–1500 km. It mainly constitutes free electrons and ions which are responsible for the path delay in the signals [3]. The total electron content specifies the total number of free electrons in a column of $1 \times 1 \text{ m}^2$ along the signal path [3]. The number of free electrons interacting with the signal causes the path delay. The path integral of electron density is regarded as the ionospheric delay. The ionospheric path delay is inversely proportional to square of the frequency of the signal. So microwave regions like L and P band will have more ionospheric influence as compared to X and C bands of the spectrum.

A general methodology as defined by [41] calculates the phase shift ($\Delta\psi_{\text{iono,SAR}}$) due to ionosphere as

$$\Delta\psi_{\text{iono,SAR}} = 2K \cdot \frac{\text{TEC}}{f^2 \cdot \cos \alpha} \quad (4.7)$$

Where

$K = 40.28 \text{ m}^3 \text{ s}^{-2}$ is refractive constant

$f = 5.405 \text{ GHz}$ is the frequency of the RADAR signal

α in degrees denotes the satellite off nadir angle

The TEC data is available as GIM's (Global Ionospheric Maps) which are updated every hour. The TEC data is also available from IRI-model. In this study, TEC data from IRI-2007 model is used because TEC from GPS data is generally overestimated because it also includes the plasma exosphere which extends above the ionosphere [46]. RADARSAT-2 is approximately 800 km above the earth's surface. So, the IRI model is suitable as it gives the TEC value till ionosphere layer only i.e. within 800 km above the surface.

4.4. DInSAR generation

For our study, RADARSAT-2 SLC data on 12-10-2012, 29-11-2012 and 23-12-2012 are used. Three pass DInSAR technique can be applied but since mining subsidence is very prominent in the study area even in the RADARSAT-2 acquisition dates. In this case, for using three pass DInSAR technique, the Interferometric pair generated used to remove the topography will have subsidence information too. Hence the topographic phase will be removed from each Interferometric pair generated using a high resolution Carto-SRTM DEM. Using the same technique, three differential interferograms will be generated on which the atmospheric correction will be applied.

The steps for DInSAR generation are shown:

4.4.1. Image Co-registration and multilooking

Co-registration is the process of superimposing two or more SAR images having same acquisition geometry in their slant range geometry. Along track shift between the two SAR images can arise depending on the start-stop times of the platform in the orbits. The processing of Interferometric data requires sub pixel registration of both the images acquired in the same geometry [2].

The basic requirement of SAR interferometry is pixel to pixel matching between the SAR image pairs. Image co-registration holds a key for accurate determination of phase difference in SAR interferometry.

The process of co-registration is divided into two stages namely coarse and fine co-registration. This is done in order to speed up the procedure of optical alignment which is generally slow for large search windows [2]. This process calculates the offsets between the two SAR images. In case of coarse registration, the offsets are approximated using visual interpretation of common points in the two images or by using the orbits and timing as reference [2]. Then the fine co-registration is applied using automatic correlation techniques to get sub-pixel alignment accuracy [2]. Resampling is done to fit the reference image after the offsets are determined.

RADAR imaging geometry is in slant range i.e., it measures the distance between the objects and also the distance from the sensor in slant range direction. In this process, the objects in near range appear to be compressed as compared to the object in far range. This is also known as slant range distortion. This effect can be removed by converting the slant range in to ground range resolution. This process reduces the overall spatial resolution.

The ground range resolution is given by the following [48]:

$$G = \frac{c\tau}{2\sin\theta} \quad (4.8)$$

where G is the ground range resolution.

c is the speed of light.

τ is the pulse length.

θ is the look angle.

The process of converting the slant range resolution into ground range is done by multilooking. The number of looks is a function of pixel spacing in range direction, azimuth direction and incidence angle. The multilooked image will have approximately square pixels.

4.4.2. Baseline estimation

Interferogram generation is only possible when the ground reflectivity acquired with at least two antennae overlap [47]. If the perpendicular component of the baseline crosses beyond a certain limit, it is termed as critical baseline [47]. In this stage, the phase information is not preserved because of geometric decorrelation. This can lead to loss of coherence. The critical baseline is calculated as follows:

$$B_{cr} = \frac{\lambda R \tan(\theta)}{2R_r} \quad (4.9)$$

Where λ is wavelength of the RADAR signal.

R is the range distance.

θ is the incidence angle.

R_r is the pixel spacing in range

Apart from the perpendicular and critical baselines, the sensitivity to height variations is inversely proportional to 2π ambiguity height. The bigger the ambiguity height, the capability of

detecting small elevation changes reduces [47]. The sensitivity to detect displacement is dependent on the wavelength.

The Baseline details of the Interferometric pairs are shown in the Table.(4-3):

Table 4-3: Baseline values of interferometric pairs

S. no	Data pairs	Date1	Date2	Baseline(m)			2 Pi Ambiguity(m)		Doppler	
				Normal	Critical	Temporal	Height	Displacement	Centroid difference	Critical
1	Oct12-Nov29	12-10-2012	29-11-2012	98.3	1263.4	48	114.2	0.028	-39.9	1269.7
2	Nov29-Dec23	29-11-2012	23-12-2012	155.9	1263.3	24	72.0	0.028	-8.4	1269.7
3	Oct12-Dec23	12-10-2012	23-12-2012	58.4	1263.4	72	192.2	0.028	-48.3	1269.7

Further in this study, the interferometric pairs are annotated as follows:

According to the Table.(4-3), the interferometric pairs namely Oct12-Nov29, Nov29-Dec23 and Oct12-Dec23 will be used as data pair (1), data pair (2) and data pair (3).

4.4.3. Interferogram generation

The Single look complex image is in the form of a two dimensional matrix where each pixel is associated with phase and amplitude. The amplitude is related to surface reflectivity. The phase registers the changes at the surface. In order to extract meaningful information from phase, repeat pass acquisition is carried out for which a correlation between the phase terms can be deduced. Subtracting the two phases gives the height of the pixel in relation to the height of the sensor.

Multiplying one image by the complex conjugate of the other generates an interferogram. The interferogram formed has phase difference contributions from topography, noise, atmosphere and also any displacements occurred during the master and slave acquisitions.

The interferogram generation is the process of pixel to pixel computation of the Hermitian product of two co-registered SAR images.

The phase of an interferogram is represented as follows [47]:

$$\phi = \tan^{-1} \left(\frac{\text{Imag}(I)}{\text{Real}(I)} \right) \quad (4.10)$$

Where $\text{Imag}(I)$ and $\text{Real}(I)$ are the imaginary and real parts of the interferogram.

The interferograms of three SLC images are shown:

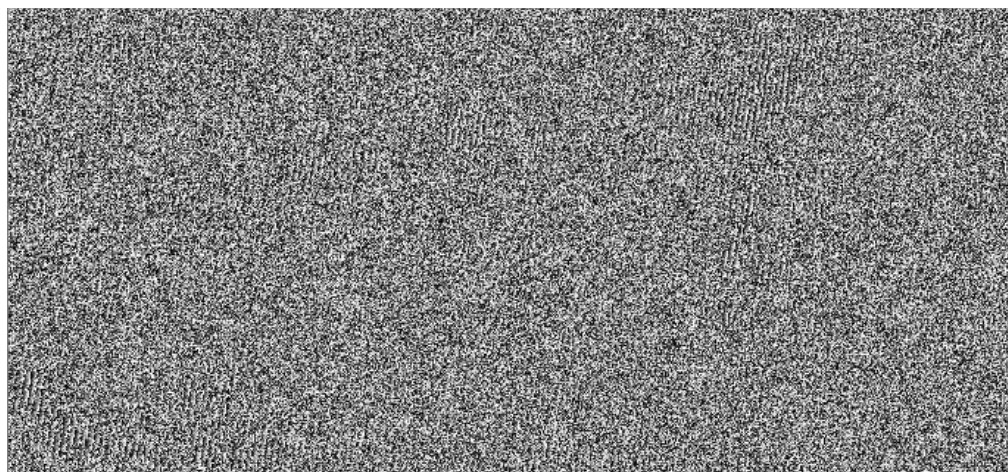


Figure 4-11: Interferogram of data pair (1)

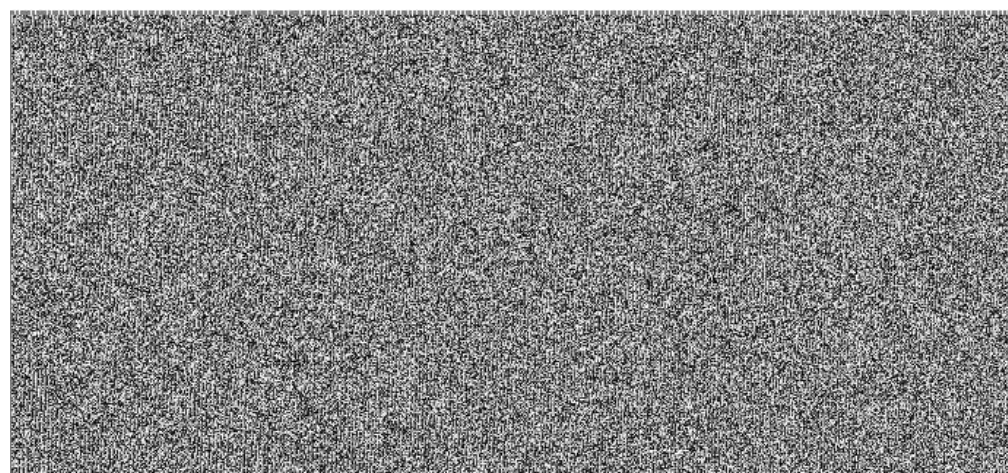


Figure 4-12: Interferogram of data pair (2)

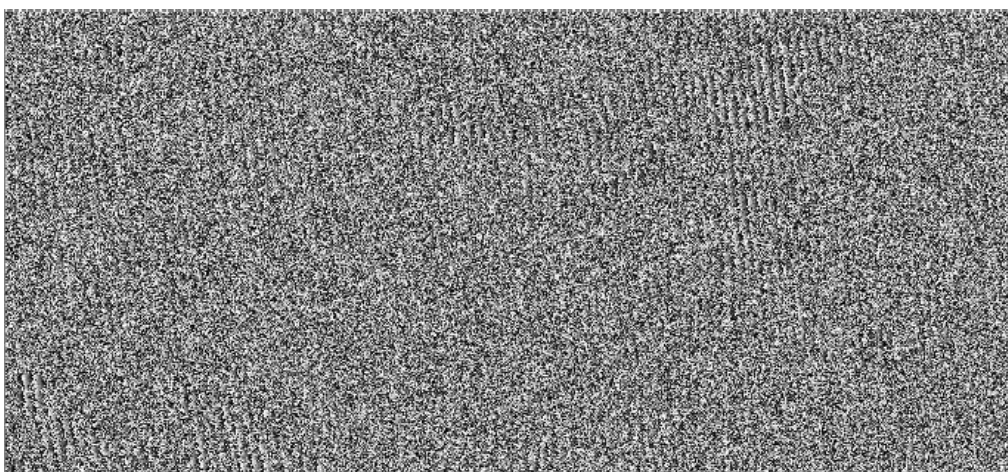


Figure 4-13: Interferogram of data pair (3)

4.4.4. Interferogram flattening and Topographic phase removal

The fringe pattern caused by the flat earth overlay on the topographic fringes of the interferogram. The raw interferogram generated in section(4.4.3) can't avoid the flat earth effect due to the InSAR imaging geometry. The flat earth effect is caused due to the non-zero baseline. Due to the flat earth effect, the points with the same height on the surface will not have the same interferometric phase [50]. Performing this process with a high quality external DEM, the residual interferogram generated is free from topography and the remaining fringes will be only related to change in elevation, displacements, atmosphere and noise.

The reference DEM is given as input to the flattening process which in turn removes the available topographic term from the interferogram. The output of this step is a flattened interferogram or a differential/residual phase interferogram which is devoid of the topographic fringes.

The DEM mentioned in section(4.1) was used to generate three differential interferograms which contained the deformation fringes.

4.4.5. Adaptive filter and coherence generation

The filtering method incorporates the reduction of noise in the interferogram. The sources of phase noise in the interferogram are due to baseline decorrelation, temporal decorrelation and also thermal noise generated by the sensor.

Coherence which is an indicator of phase quality is generated. The coherence calculated from two input co-registered SAR images (S_1) and (S_2) is defined as [47]:

$$\gamma = \frac{|\sum S_1(x) \cdot S_2(x)^*|}{\sqrt{\sum |S_1(x)|^2 \cdot \sum |S_2(x)|^2}} \quad (4.11)$$

Coherence is defined as the degree of similarity between two SAR images [2]. The coherence image values range between 0 and 1. The value 1 indicates the areas with high coherence and value 0 indicates the areas with low coherence.

The estimated coherence is a function of systematic spatial de-correlation and temporal de-correlation between the master and slave images [47].

In general, coherence decreases with increase in master-slave acquisition time intervals. Data pairs with low coherence are not used to derive phase related measurements.

Filtering is essential to minimize the phase noise and retrieve the surface information which is present in the phase of the interferogram [51].

In this study, filtering was done using Boxcar filter to identify the subsidence fringes and derive the subsidence measurements. Boxcar filter works well for homogeneous areas [51].

4.4.6. Phase unwrapping

The phase signal of the interferogram is given as a modulo 2π . The interferogram containing wrapped phase results in 2π ambiguity. The phase unwrapping process resolves this 2π ambiguity by adding correct multiples of 2π to the Interferometric phase for each pixel.

4.5. Phase correction

The phase correction is done on the phase of the differential interferogram by using the atmospheric range correction bands generated. The differential interferogram generated is split into two components namely phase and amplitude (module). This phase is corrected by removing the atmospheric range correction bands. The corrected phase is then recombined with the module component to generate the atmospheric phase corrected differential interferogram.

The propagational delay of the RADAR signal corresponding to the phase eq.(2.3), (2.4) and (2.5) are shown:

$$\Psi_1 = \frac{4\pi}{\lambda} (\rho + \Delta R_1) \quad (4.12)$$

$$\Psi_2 = \frac{4\pi}{\lambda} (\rho + \delta\rho + \Delta R_2) \quad (4.13)$$

$$\Psi_3 = \frac{4\pi}{\lambda} (\rho + \delta\rho' + \Delta R_3) \quad (4.14)$$

The Interferometric phases of two interferograms corresponding to the above eq.(4.12),(4.13) and(4.14) are formulated as shown:

$$\Phi_1 = \Psi_2 - \Psi_1 = \frac{4\pi}{\lambda} \delta\rho + \frac{4\pi}{\lambda} (\Delta R_2 - \Delta R_1) \quad (4.15)$$

$$\Phi_2 = \Psi_3 - \Psi_1 = \frac{4\pi}{\lambda} \delta\rho' + \frac{4\pi}{\lambda} (\Delta R_3 - \Delta R_1) \quad (4.16)$$

Where ΔR_1 , ΔR_2 and ΔR_3 are the atmospheric propagation delays generated.

Hence the corrected phases of the interferograms are generated. They are represented as:

$$\frac{4\pi}{\lambda} \delta\rho = \Phi_1 - \frac{4\pi}{\lambda} (\Delta R_2 - \Delta R_1) \quad (4.17)$$

$$\frac{4\pi}{\lambda} \delta\rho' = \Phi_2 - \frac{4\pi}{\lambda} (\Delta R_3 - \Delta R_1) \quad (4.18)$$

Where $\frac{4\pi}{\lambda} \delta\rho$ and $\frac{4\pi}{\lambda} \delta\rho'$ are the corrected phases of two interferograms.

These corrected phases are then combined with their respective module components to produce the corrected interferograms. The corrected differential interferograms are then analysed to generate the subsidence measurements.

4.6. Validation of subsidence measurements

From the corrected differential interferograms, the subsidence fringes are identified. Through these identified fringes, the subsidence rate is calculated for each particular differential interferogram. The area and rate of subsidence generated from each differential interferogram are the validated with respect to the ground levelling data. Subsidence measurements for two test sites (Maheshpur and Bastacolla) are generated using ground levelling. The levelling test site data for Maheshpur is from November to December. The subsidence measurements for Bastacolla are from October to December. Subsidence rates identified near the two test sites from corrected DInSAR are then compared with the subsidence data from the ground levelling data of the particular test site.

Rate of subsidence is calculated using the below formula:

One colour cycle (fringe) is 2π which is half the RADAR wavelength.

For RADARSAT-2 ($\lambda/2$) = 28 mm.

$$f = \frac{n \times 28}{N} \quad (4.19)$$

where n is the number of colour (fringes) cycle repeating.

N is the total number of colours in a cycle (in this case 7)

$$\text{Subsidence rate} \left(\frac{\text{mm}}{\text{year}} \right) = (f \times D) / B_t \quad (4.20)$$

where B_t is the temporal baseline in days.

D is the total number of days in a year. (in this case 366 since 2012 being a leap year)

The atmospheric path delay bands and the generation of corrected DInSAR along with validation are shown and explained in results and discussion chapter:

5. RESULTS AND DISCUSSION

This chapter is divided into the following sub sections:

- 5.1 Comparison of weather station meteorological parameters with MODIS derived parameters.
- 5.2 Modelling the MODIS temperature and pressure bands for the time of acquisition of RADARSAT-2 using regression analysis between the weather station and MODIS readings.
- 5.3 Tropospheric path delay computation.
- 5.4 Ionospheric path delay computation.
- 5.5 Total path delay computation.
- 5.6 DInSAR generation and phase correction.
- 5.7 Subsidence measurement and validation.

5.1. Comparison of weather station meteorological parameters with MODIS derived parameters

The field work was done in the months of October, November and December during the RADARSAT-2 SLC data acquisition. As shown in Section 4.2, MODIS water vapour products were downloaded and the temperature and pressure bands were extracted. The values of these meteorological parameters were compared with the weather station parameters for the same point in the field. The comparison of the data is shown individually for every month below:

Comparison of temperature(T) in October:

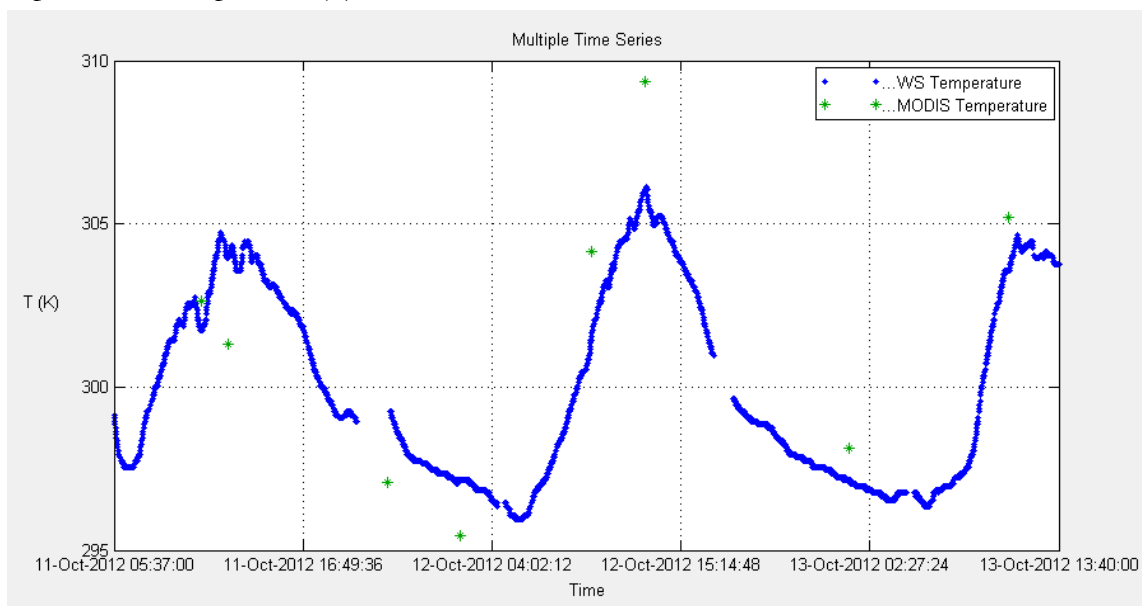


Figure 5-1: Comparison between temperature readings from weather station (WS) and MODIS in October

Comparison of pressure(P) in October:

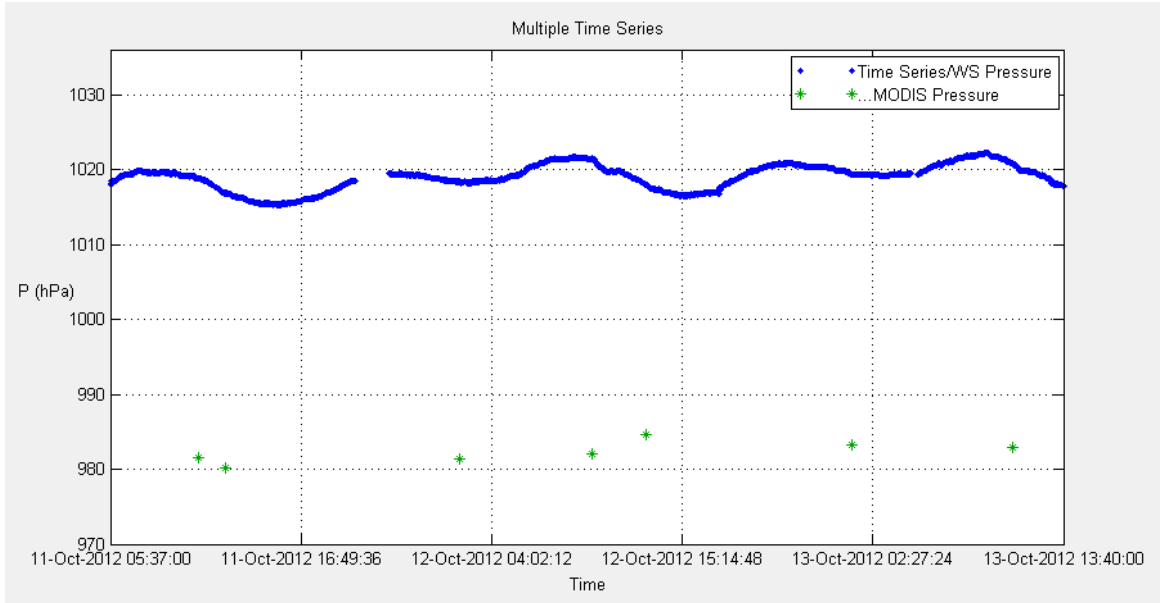


Figure 5-2: Comparison between pressure readings from weather station (WS) and MODIS in October

Comparison of Temperature(T) in November:

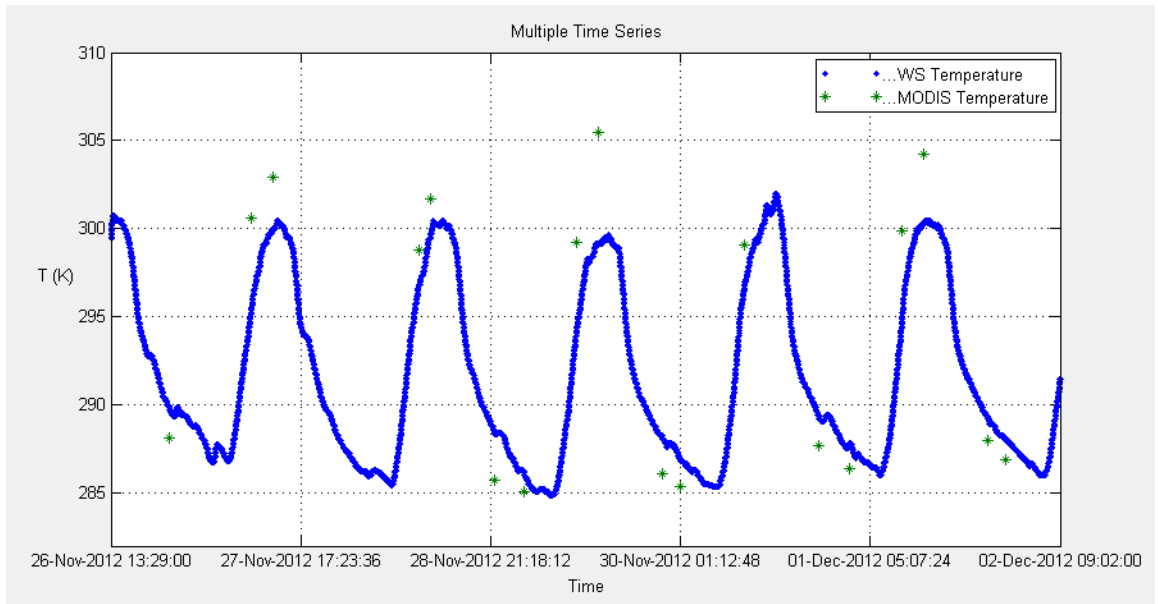


Figure 5-3: Comparison between temperature readings from weather station (WS) and MODIS in November

Comparison of Pressure(P) in November:

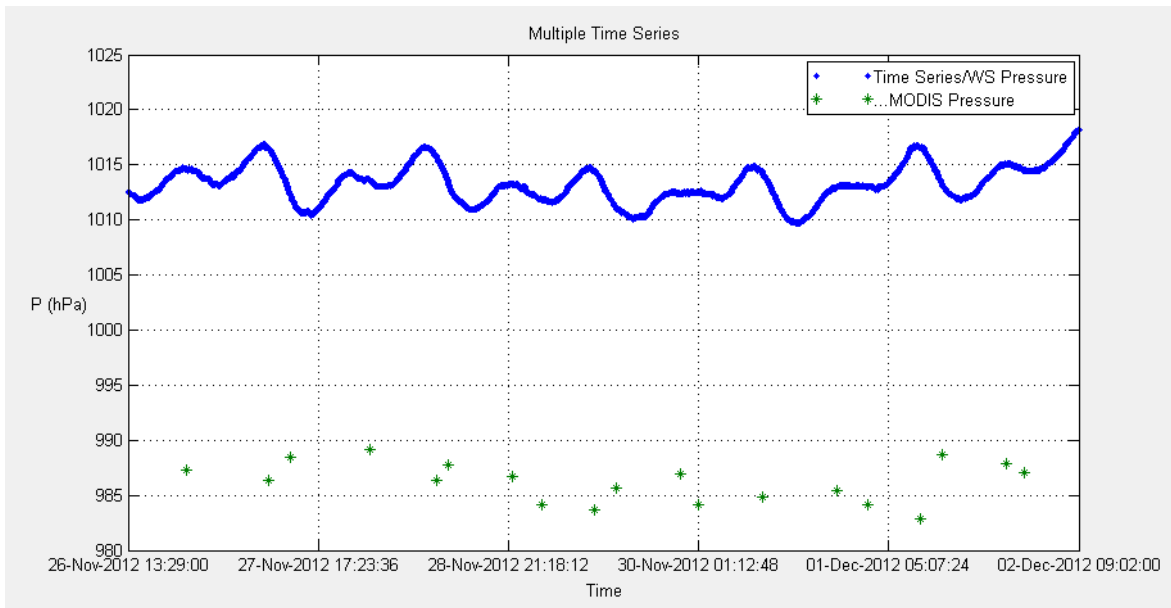


Figure 5-4: Comparison between pressure readings from weather station (WS) and MODIS in November

Comparison of Temperature(T) in December:

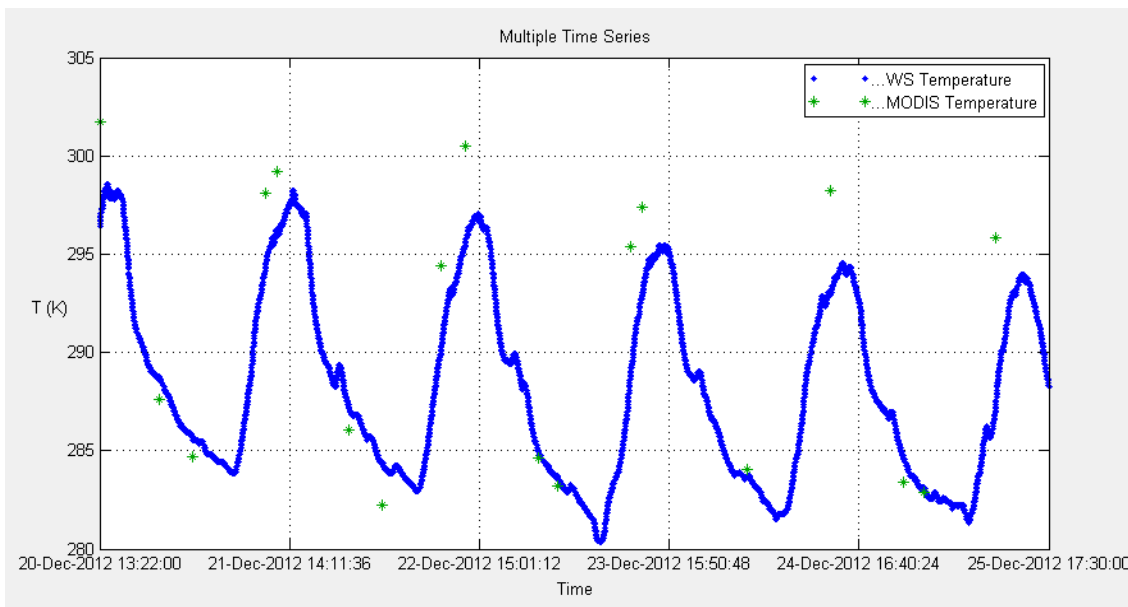


Figure 5-5: Comparison between temperature readings from weather station (WS) and MODIS in December

Comparison of Pressure(P) in December:

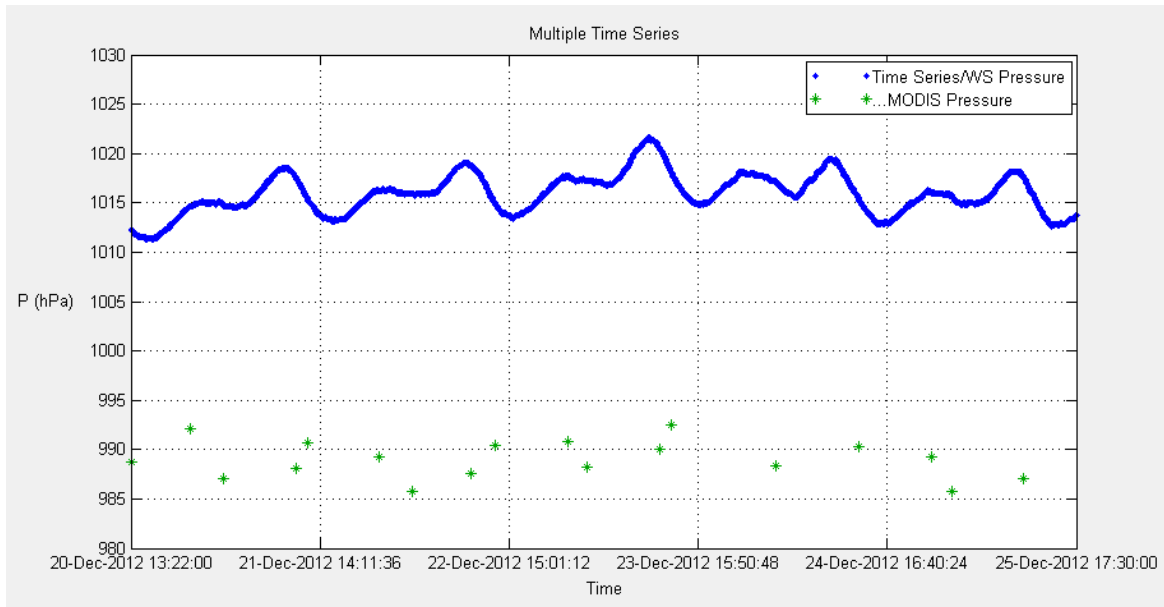


Figure 5-6: Comparison between pressure readings from weather station (WS) and MODIS in December

Discussion of the above comparison for temperature and pressure plots:

It is clearly observed from the above temperature plots in Figs.(5-1),(5-3),(5-5) that the value of temperature from MODIS is overestimated during the day and underestimated during the night. It is also clearly observed that the MODIS derived temperature readings are much closer to the weather station readings during the night time as compared to the day time. In other words, the offset in temperature readings between the weather station and MODIS during the night and early hours was less as compared to morning and noon hours.

From the Figs.(5-2),(5-4),(5-6), the pressure readings from MODIS when compared with the weather stations readings, it is clearly depicted that there has been a continuous offset of about 25-40 hPa between the two. The overall trend of the pressure readings was almost similar.

In order to predict the MODIS temperature and pressure bands for the acquisition time of RADARSAT-2, a regression analysis was performed to define the relationship between the MODIS derived readings and the weather station readings

5.2. Modelling the MODIS temperature and pressure bands for the time of acquisition of RADARSAT-2 using regression analysis between the weather station and MODIS readings.

Temperature fit of October data:

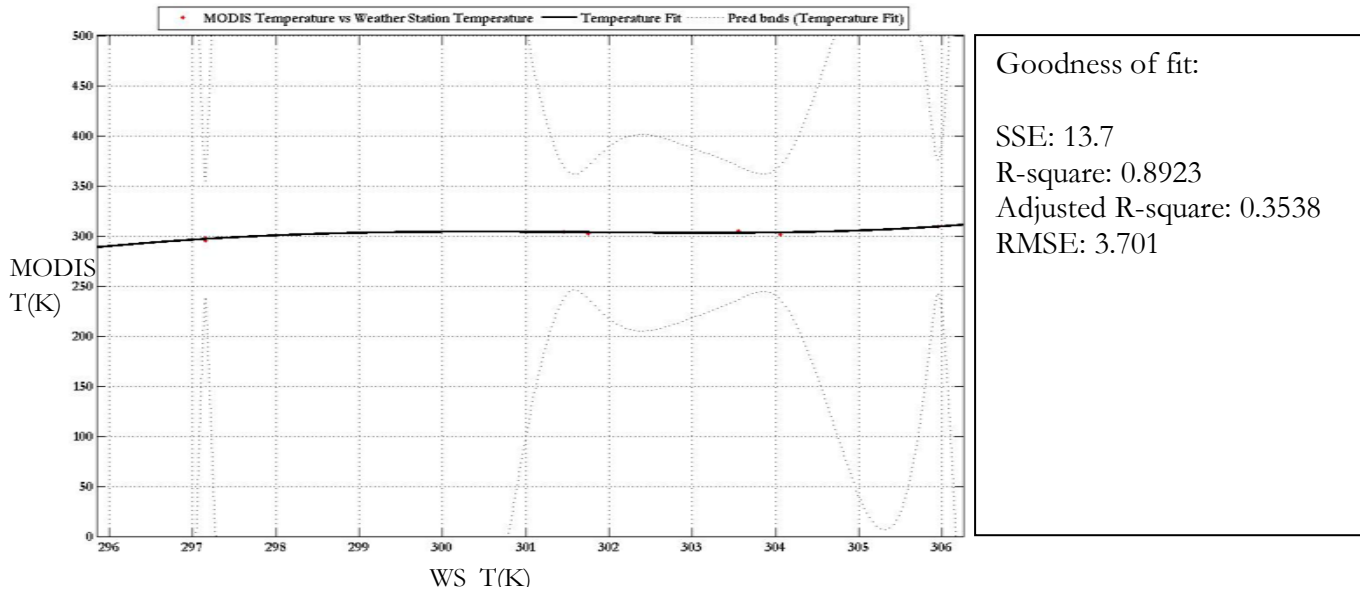


Figure 5-7: Temperature fit for October data

Analysis of the Temperature fit:

Based on the XY plot of the points, Gaussian second order was the best fit curve which could define the relationship between the MODIS temperature and weather station temperature readings. For the month of October, the temperature fitting was performed with only 7 points.

General model Gauss2:

$$f(x) = a1 \cdot \exp(-((x-b1)/c1)^2) + a2 \cdot \exp(-((x-b2)/c2)^2) \quad (5.1)$$

Coefficients (with 95% confidence bounds):

- a1 = 3.747e+016 (-2.202e+024, 2.202e+024)
- b1 = 752.9 (-8.06e+008, 8.06e+008)
- c1 = 77.62 (-7.121e+007, 7.121e+007)
- a2 = 256.8 (-3.537e+006, 3.537e+006)
- b2 = 296.8 (-4.855e+004, 4.915e+004)
- c2 = 13.23 (-6.429e+004, 6.432e+004)

The fitting of temperature data in October is based on the 7 collected data values. Due to the less number of points, gaussian2 fit shows high ranges of confidence interval for fit. Due to lack of extensive data values for fitting, this model showed greater uncertainties for the Gaussian2 fit.

When the relation has been established, based on the function $f(x)$, the temperature value of MODIS at 05:47 AM has been modelled. The modelled value is shown as follows:

Value of weather station at 05:47 AM on 12-10-2012	–	295.95 K
Modelled value of MODIS at 05:47 AM on 12-10-2012	–	289.69 K

Based on the comparison of the values in Fig.(5-1), it is depicted that the temperature values of MODIS are overestimated during the day time and underestimated during the night time. The modelled value from the fit follows this functionality.

Hence based on the curve fitting, the temporal pattern of the temperature value of MOD07 has been predicted but the spatial variation lacks because of single weather station. For that reason, the temperature band was generated by calibrating the near MOD07 temperature band using the predicted temperature value. The spatial variation of the temperature is inherited from the temperature band which is calibrated.

This process could model the temperature value at 05:47 AM and also preserve the spatial variation among the modelled pixels.

The modelled value of temperature accepts our observation in section 5.1, where it is observed that MODIS underestimates the weather station readings during the night and early hours. The modelled output follows the same trend.

The same procedure is carried out for predicting the temperature values on 29-11-12 and 23-12-12 which are the RADARSAT-2 satellite date of passes. Hence the calibrated temperature bands have been generated for 12-10-2012, 29-11-2012 and 23-12-2012 at 05:47 AM IST.

Pressure fit of October data:

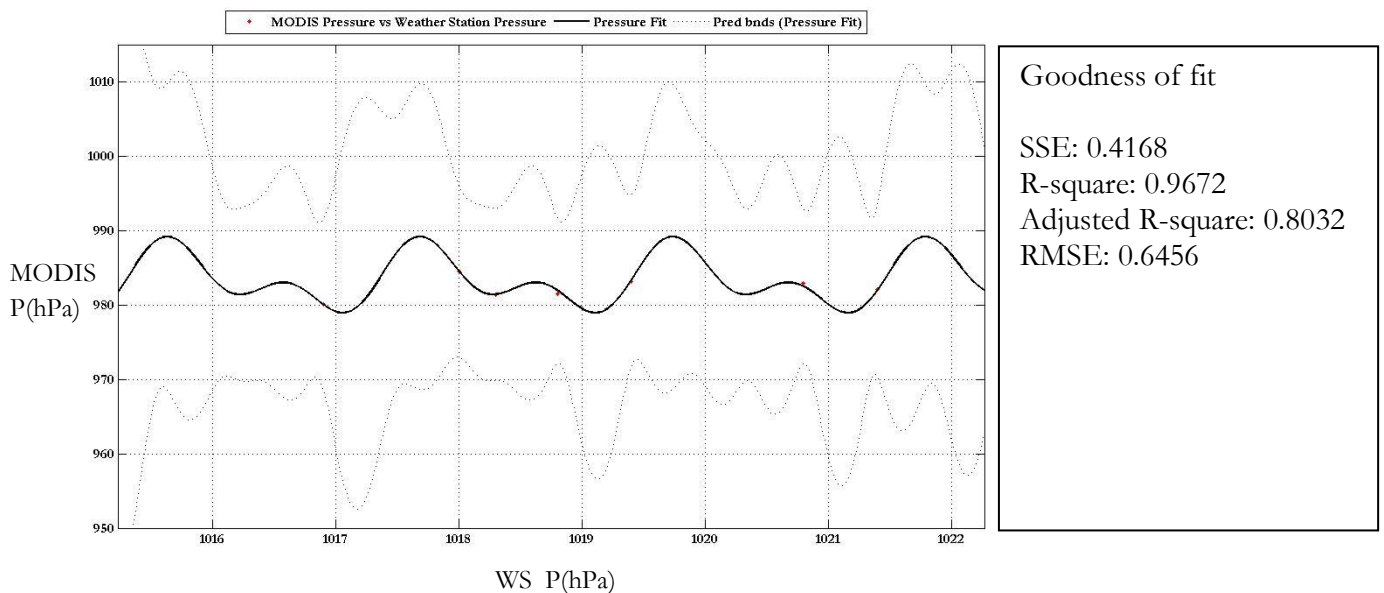


Figure 5-8: Pressure fit for October data

Analysis of pressure fit:

Based on the XY plot of the points, Fourier2 was the best fit curve which could define the relationship between the MODIS pressure and weather station pressure readings. For the month of October, the pressure fitting was performed with only 7 points.

General model Fourier2:

$$f(x) = a_0 + a_1 \cos(x*w) + b_1 \sin(x*w) + a_2 \cos(2*x*w) + b_2 \sin(2*x*w) \quad (5.2)$$

Coefficients (with 95% confidence bounds):

$$\begin{aligned} a_0 &= 983.3 \quad (978.5, 988.2) \\ a_1 &= 2.719 \quad (-1857, 1862) \\ b_1 &= -1.974 \quad (-2562, 2558) \\ a_2 &= -1.225 \quad (-4502, 4500) \\ b_2 &= -2.398 \quad (-2312, 2307) \\ w &= 3.061 \quad (2.139, 3.984) \end{aligned}$$

The fitting of pressure data in October is based on the 7 collected data values. Although fewer data values were collected, the uncertainty generated from the fitting is low.

When the relation has been established, based on the function $f(x)$, the temperature value of MODIS at 05:47 AM has been modelled. The modelled value is shown as follows:

Value of weather station at 05:47 AM on 12-10-2012	–	1017.7 hPa
Modelled value of MODIS at 05:47 AM on 12-10-2012	–	989.52 hPa

Hence based on the curve fitting, the temporal pattern of the pressure value of MOD07 has been predicted but the spatial variation lacks because of single weather station. For that reason, the pressure band was generated by calibrating the near MOD07 pressure band using the predicted pressure value. The spatial variation of the pressure is inherited from the pressure band which is calibrated.

This process could model the pressure value at 05:47 AM and also preserve the spatial variation among the modelled pixels.

The modelled value of pressure accepts our observation in section(5.1), where it is observed that MODIS underestimates the weather station readings of pressure values with an offset between 25 and 45 hPa. The modelled output follows the same trend.

The same procedure is carried out for predicting the pressure values on 29-11-12 and 23-12-12 which are the RADARSAT-2 satellite date of passes. Hence the calibrated pressure bands have been generated for 12-10-2012, 29-11-2012 and 23-12-2012 at 05:47 AM IST.

Temperature fit of November data:

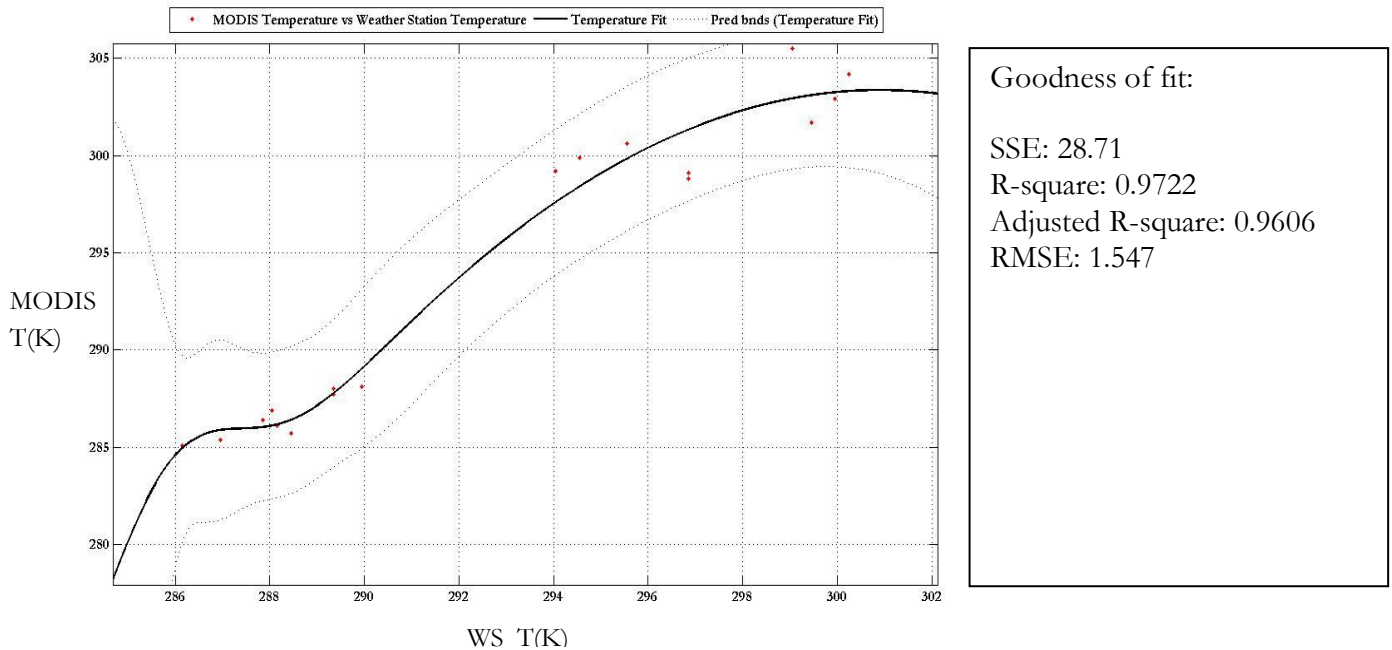


Figure 5-9: Temperature fit for November data

Analysis of temperature fit:

Based on the XY plot of the points, Gaussian second order was the best fit curve which could define the relationship between the MODIS temperature and weather station temperature readings. For the month of November, the temperature fitting was performed with 18 points.

General model Gauss2:

$$f(x) = a1*\exp(-((x-b1)/c1)^2) + a2*\exp(-((x-b2)/c2)^2) \tag{5.3}$$

Coefficients (with 95% confidence bounds):

- a1 = 303.4 (300.7, 306)
- b1 = 300.9 (295.9, 305.9)
- c1 = 49.48 (25.73, 73.23)
- a2 = 7.571 (-7.696, 22.84)
- b2 = 285.8 (280.7, 290.9)
- c2 = 2.146 (-3.102, 7.393)

The major difference in the fitting of this curve is mainly due to the presence of more data values as compared to that of October data fitting. The data values in this case show improvement in the confidence interval for this Gaussian2 fitting.

When the relation has been established, based on the function $f(x)$, the temperature value of MODIS at 05:47 AM has been modelled. The modelled value is shown as follows:

Value of weather station at 05:47 AM on 29-11-2012 – 285.05 K
 Modelled value of MODIS at 05:47 AM on 29-11-2012 – 280.47 K

The modelled value follows the observed trend in section(5.1).

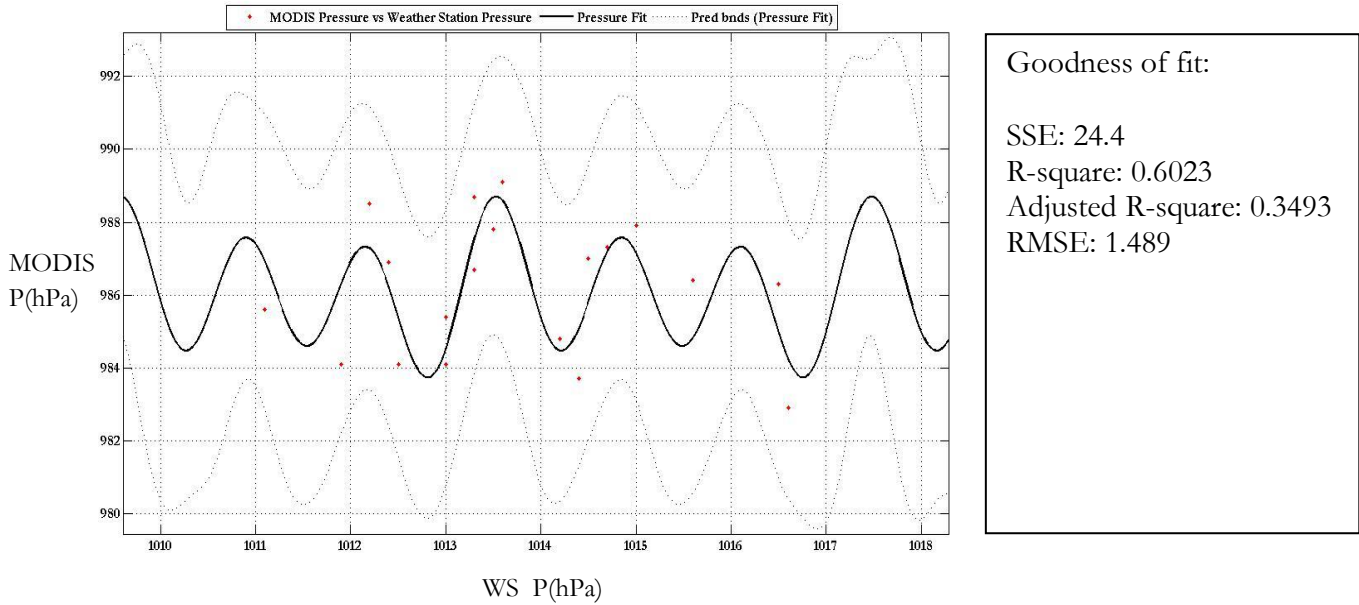


Figure 5-10: Pressure fit for November data

Analysis of pressure fit:

Based on the XY plot of the points, Fourier3 was the best fit curve which could define the relationship between the MODIS pressure and weather station pressure readings. For the month of November, the pressure fitting was performed with 18 points.

General model Fourier3:

$$f(x) = a_0 + a_1 \cdot \cos(x \cdot w) + b_1 \cdot \sin(x \cdot w) + a_2 \cdot \cos(2 \cdot x \cdot w) + b_2 \cdot \sin(2 \cdot x \cdot w) + a_3 \cdot \cos(3 \cdot x \cdot w) + b_3 \cdot \sin(3 \cdot x \cdot w) \tag{5.4}$$

Coefficients (with 95% confidence bounds):

- $a_0 = 986.1$ (985.2, 986.9)
- $a_1 = 0.3896$ (-12.64, 13.42)
- $b_1 = -0.0903$ (-56.74, 56.56)
- $a_2 = -0.1784$ (-164, 163.6)
- $b_2 = -0.5596$ (-52.75, 51.63)
- $a_3 = -1.777$ (-14.97, 11.42)
- $b_3 = 0.03048$ (-780.5, 780.6)
- $w = 1.592$ (1.448, 1.737)

The fitting of this Fourier3 curve shows better results in terms of confidence interval mainly due to the higher Fourier transformation order. The presence of 18 data values (7 in the case of October), combined with Fourier regression gives better fit.

When the relation has been established, based on the function $f(x)$, the temperature value of MODIS at 05:47 AM has been modelled. The modelled value is shown as follows:

Value of weather station at 05:47 AM on 29-11-2012 – 1012.6 hPa

Modelled value of MODIS at 05:47 AM on 29-11-2012 – 984.59 hPa

The modelled value follows the observed trend in section(5.1).

Temperature fit of December data:

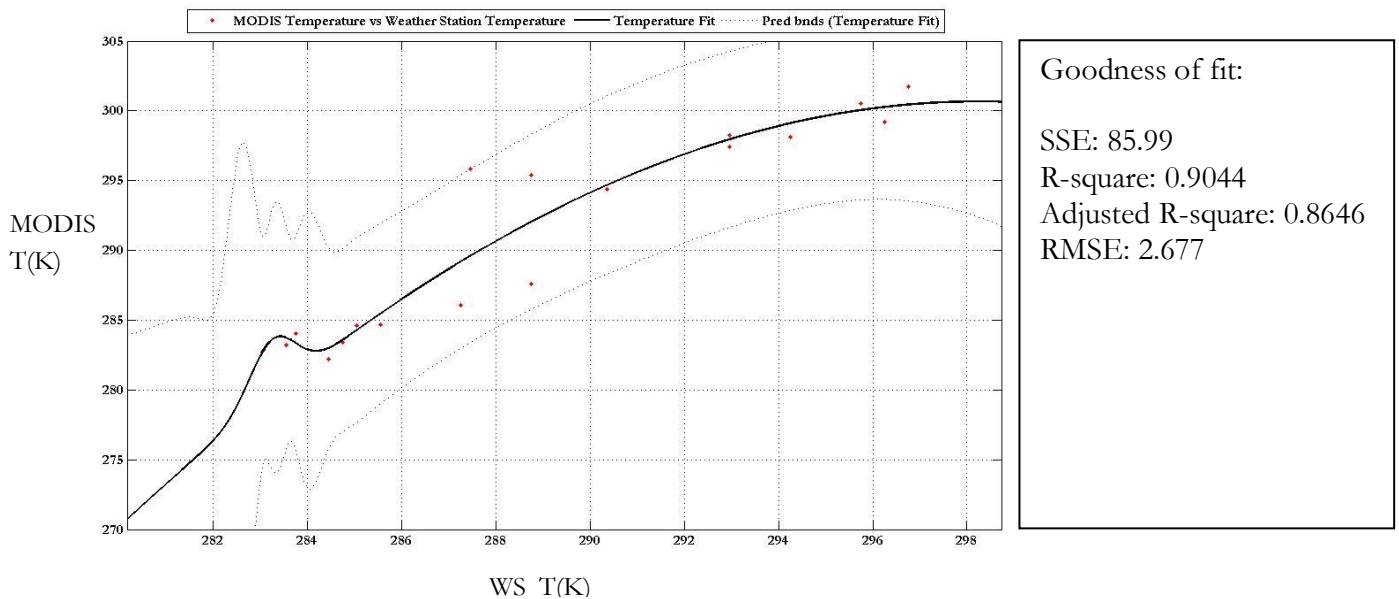


Figure 5-11: Temperature fit for December data

Analysis of temperature fit:

Based on the XY plot of the points, Gaussian second order was the best fit curve which could define the relationship between the MODIS temperature and weather station temperature readings. For the month of December, the temperature fitting was performed with 18 points.

General model Gauss2:

$$f(x) = a1*\exp(-((x-b1)/c1)^2) + a2*\exp(-((x-b2)/c2)^2) \tag{5.5}$$

Coefficients (with 95% confidence bounds):

- a1 = 300.7 (294.7, 306.6)
- b1 = 298.3 (288.2, 308.3)
- c1 = 55.91 (18.92, 92.9)
- a2 = 3.919 (-3.651, 11.49)
- b2 = 283.2 (281.7, 284.8)
- c2 = 0.7007 (-3.017, 4.418)

When the relation has been established, based on the function $f(x)$, the temperature value of MODIS at 05:47 AM has been modelled. The modelled value is shown as follows:

Value of weather station at 05:47 AM on 23-12-2012	–	281.55 K
Modelled value of MODIS at 05:47 AM on 23-12-2012	–	274.92 K

The modelled value follows the observed trend in section(5.1.

Pressure fit of December data:

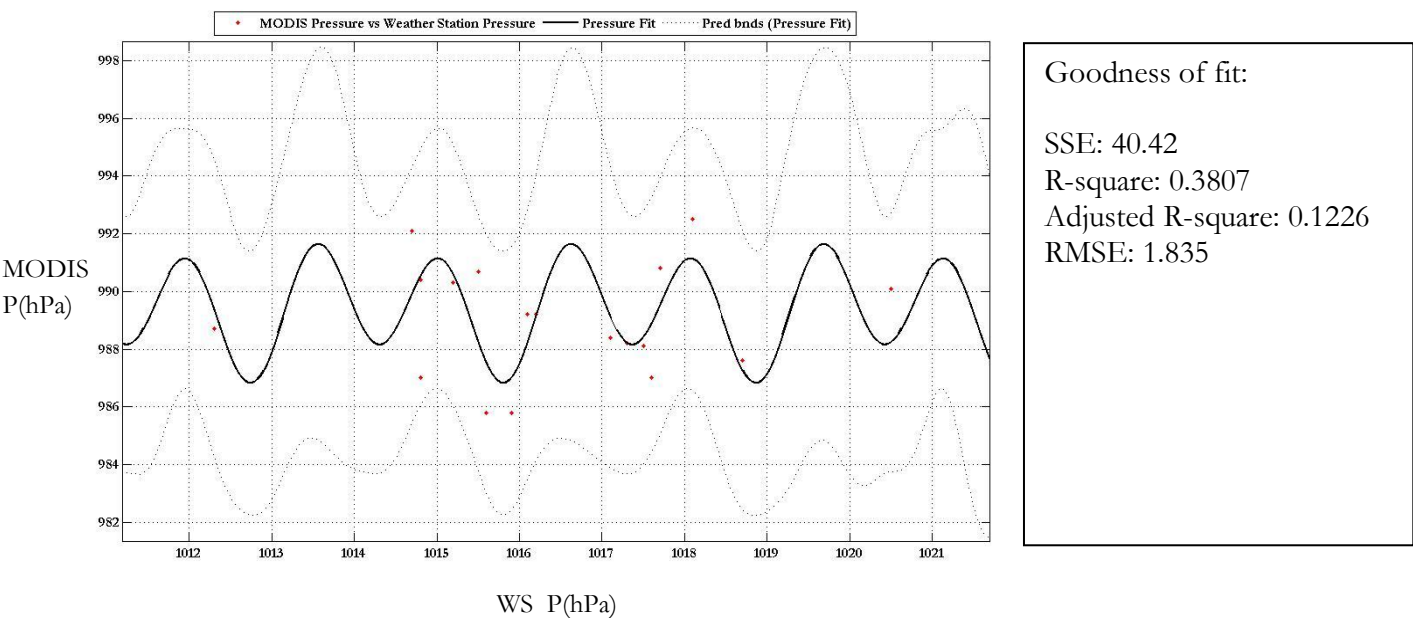


Figure 5-12: Pressure fit for December data

Analysis of pressure fit:

Based on the XY plot of the points, Fourier3 was the best fit curve which could define the relationship between the MODIS pressure and weather station pressure readings. For the month of December, the pressure fitting was performed with 18 points.

General model Fourier2:

$$f(x) = a_0 + a_1*\cos(x*w) + b_1*\sin(x*w) + a_2*\cos(2*x*w) + b_2*\sin(2*x*w) \tag{5.6}$$

Coefficients (with 95% confidence bounds):

- a0 = 989.4 (987.9, 991)
- a1 = -0.2059 (-140.3, 139.9)
- b1 = 0.6791 (-41.68, 43.03)
- a2 = 0.4969 (-770.8, 771.8)
- b2 = 1.866 (-203.6, 207.3)
- w = 2.053 (1.849, 2.256)

When the relation has been established, based on the function $f(x)$, the temperature value of MODIS at 05:47 AM has been modelled. The modelled value is shown as follows:

Value of weather station at 05:47 AM on 23-12-2012	–	1017.7 hPa
Modelled value of MODIS at 05:47 AM on 23-12-2012	–	989.52 hPa

The modelled value follows the observed trend in section(5.1).

Water vapour pressure band generation:

The water vapour pressure has been generated from the weather station using the temperature and humidity readings. The water vapour pressure is derived using the standard formula:

$$P_w = H \cdot \frac{T}{C} \quad (5.7)$$

Where P_w is water vapour pressure in Pa

H is the humidity.

C is constant (2.16679 gK/J)

The water vapour pressure bands for 12-10-2012, 29-11-2012 and 23-12-2012 have been calculated from the temperature and humidity readings of the weather station recorded at 05:47 AM. These values are used to generate the water vapour pressure bands by directly taking the offset between the pixels of Precipitable water vapour (PWV) content bands of MOD07.

The generated temperature, pressure and water vapour pressure bands were used in the tropospheric path delay algorithm explained in Section 4.3.1 to compute the tropospheric path delay.

5.3. Tropospheric path delay computation

The tropospheric path delays computed give us an understanding of level of atmospheric influence on the interferogram. From the modelled temperature, pressure and water vapour pressure bands, the tropospheric path delays for the three RADARSAT-2 dates of passes have been computed.

Tropospheric path delay for 12-10-2012 data:

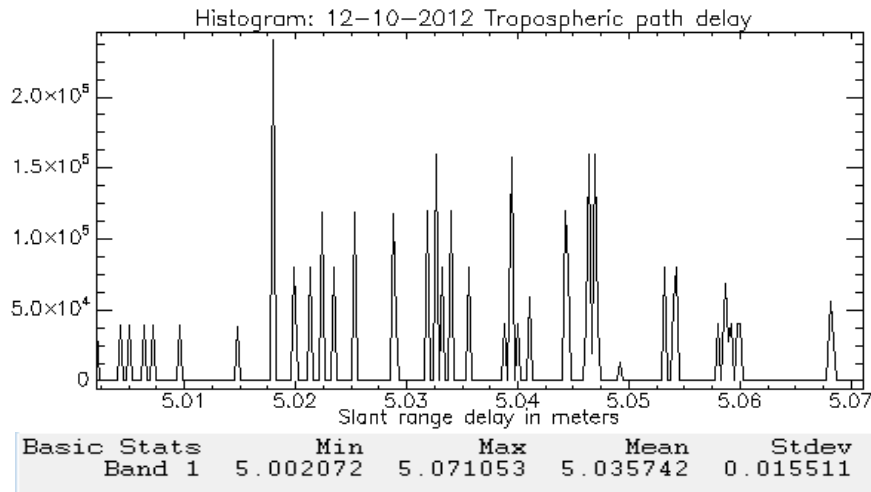


Figure 5-13: Histogram of tropospheric path delay caused on 12-10-2012

Tropospheric path delay for 29-11-2012 data:

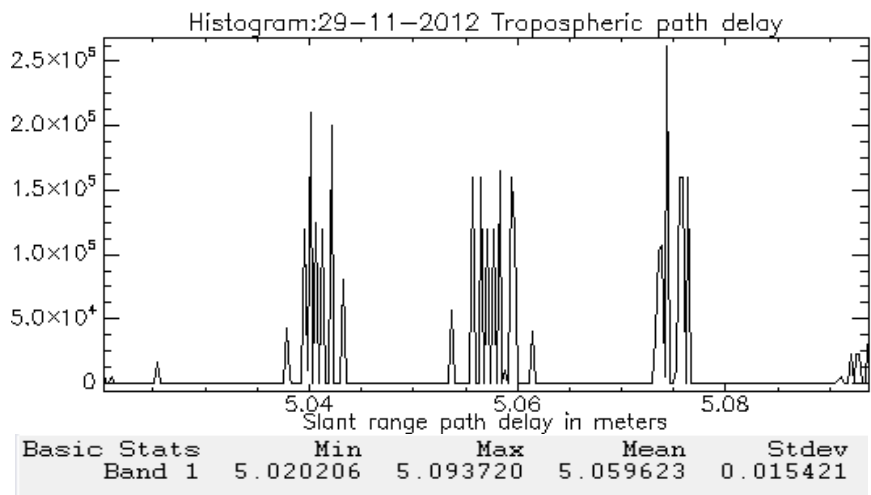


Figure 5-14: Histogram of tropospheric path delay caused on 29-11-2012

Tropospheric path delay for 23-12-2012 data:

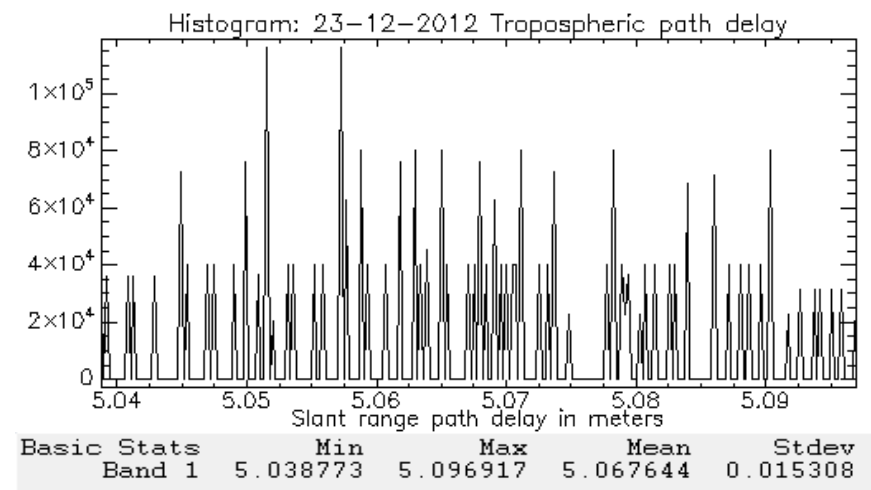


Figure 5-15: Histogram of tropospheric path delay caused on 29-12-2012

A discussion on the results of tropospheric delays:

From the Figs.(5-13),(5-14) and (5-15), it is clearly shown that the tropospheric path delay for all the three dates ranges 5.0 m to 5.07 m. According to [41], tropospheric path delay ranges between 4.6 m and 5.4 m for hydrostatic component and between 0 m and 0.8 m for wet component. It is clear from our results that the tropospheric path delays for all the three dates are within the range. It is also clear from the results that there has been considerably less effect of water vapour, clouds, temperature and humidity on the three dates.

5.4. Ionospheric path delay computation

Path delay computed from TEC data from IRI-2007 model:

Table 5-1: Ionospheric path delay calculated from TEC

	TEC (TECU)	Slant range path delay (m)
12-10-2012	6.1×10^{16}	-0.189
29-11-2012	4.4×10^{16}	-0.137
23-12-2012	3.8×10^{16}	-0.118

A discussion on the results of ionospheric delays:

Based on the TEC data from the IRI-2007 model, the slant range path delays have been computed using the formula in section 4.3.2. The spatial resolution of the IRI model is $1^\circ \times 1^\circ$. So there is only one TEC value for the entire study area. From the Table.(5-1), it is observed that there is a decreasing trend in the TEC values from October to December. The slant range delay also decreased from October to December. The negative sign in the path delay indicates a phase advance caused due to the ionized electrons present in the layer [2]. Ionospheric effects do not contribute more in case of RADAR waves with lower wavelengths. Since these effects are wavelength dependent, the ionospheric influence on the measurement results from C-Band data is less as compared to that of results from L and P band wavelengths.

5.5. Total path delay computation

Total path delay for 12-10-2012 data:

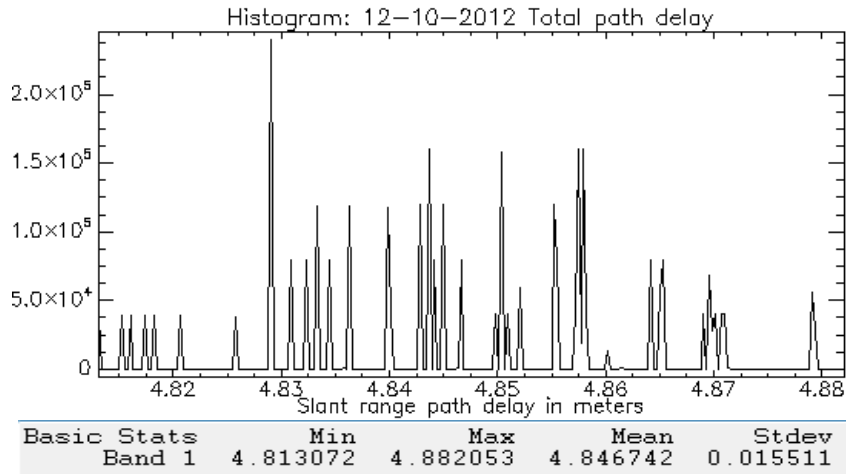


Figure 5-16: Histogram of total path delay caused on 12-10-2012

Total path delay for 23-12-2012 data:

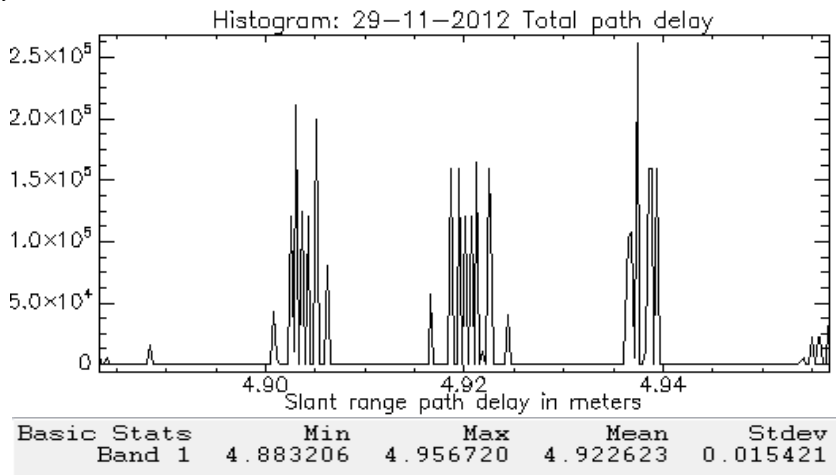


Figure 5-17: Histogram of total path delay caused on 29-11-2012

Total path delay for 23-12-2012 data:

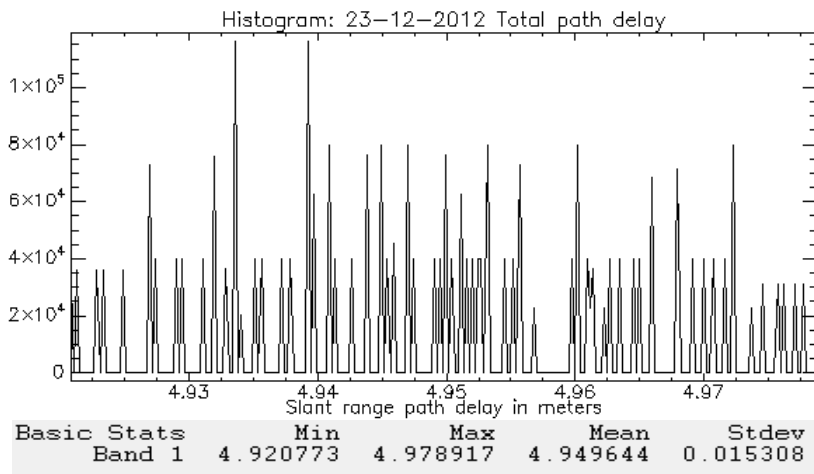


Figure 5-18: Histogram of total path delay caused on 23-12-2012

The above three Figs.(5-16),(5-17) and (5-18) show the total path delay for the three dates.

5.6. DInSAR generation and phase correction

The generated differential interferogram of data pairs of 12-10-2012 (Master) and 29-11-2012 (Slave) is shown in Fig.(5-19):

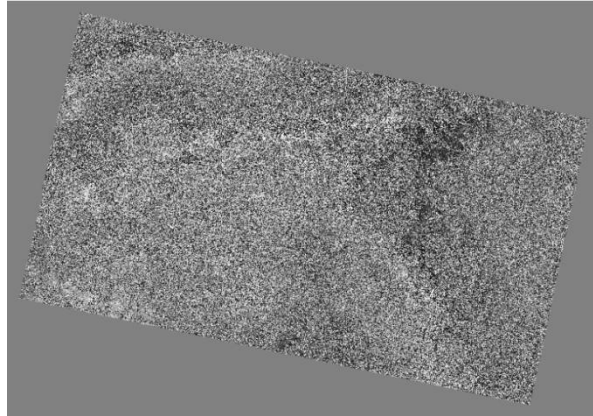


Figure 5-19: Differential interferogram (DInt) of data pair (1)

The phase of differential interferogram of data pair (1) and atmospheric corrected phase are shown in Figs.(5-20) and (5-21):

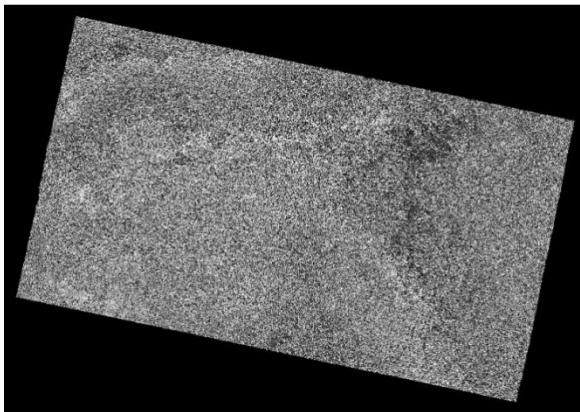


Figure 5-20: DInt phase of data pair (1)

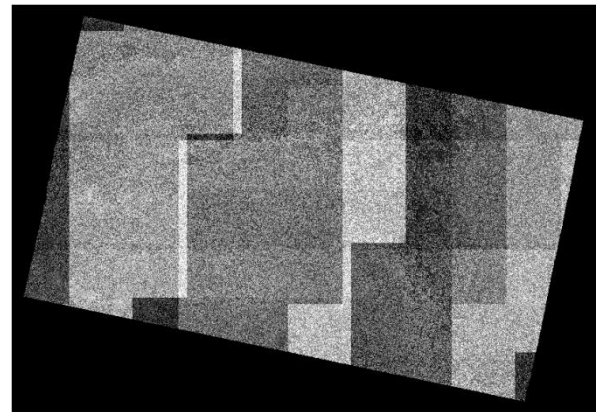
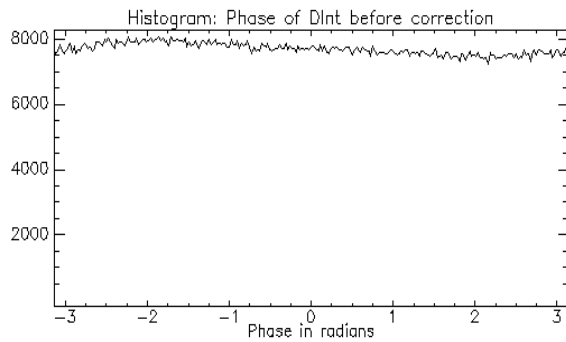


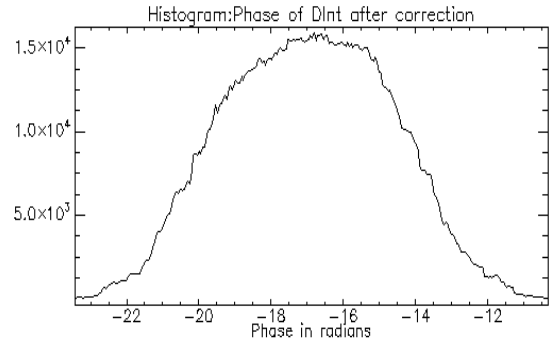
Figure 5-21: Corrected DInt phase of data pair (1)

The histograms of phases before and after correction are shown in Figs.(5-22) and (5-23):



Basic Stats	Min	Max	Mean	Stdev
Band 1	-3.141590	3.141592	-0.030637	1.811097

Figure 5-22: Phase variation before correction



Basic Stats	Min	Max	Mean	Stdev
Band 1	-23.439209	-10.337821	-16.942749	2.245152

Figure 5-23: Phase variation after correction

The corrected differential interferogram of data pair (1) is shown in Fig.(5-24):

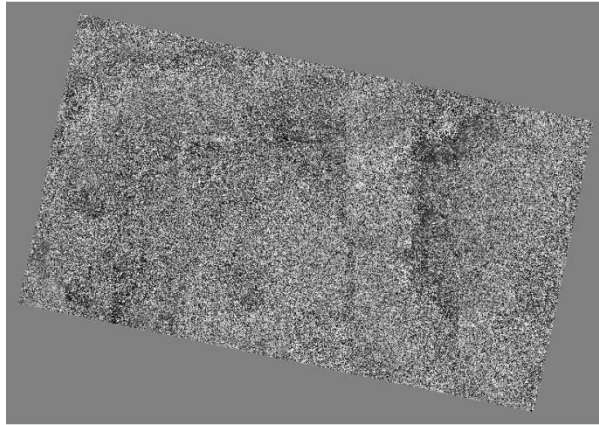


Figure 5-24: Corrected differential interferogram of data pair (1)

A discussion on the phase correction on differential interferogram of data pair (1):

The generated DInSAR phase is free from topographic phase removed by using the high resolution DEM. We have a priori information of the study area that subsidence has occurred during the time period. So the resultant phase of DInSAR generated is left with deformation phase, atmosphere phase and noise phase. Based on the phase correction procedure explained in section (4.5), the phase is corrected and the resultant phase free from atmospheric phase is shown in Fig.(5-21). The phase of the DInSAR before correction as shown in Fig.(5-22) shows a variation from -3 to +3 radians. After applying the phase correction, a drastic change is observed in the phase as shown in Fig.(5-23). The range varies between -23.4 and -10.3 radians. After the atmospheric correction, the residual phase is a combination of deformation phase and noise phase. The study chosen is a mining area with less urban settlements and continuously changing terrain and a river flowing through, there will always be a loss of coherence. The main reasons for the phase noise present in the interferogram might be due to the temporal decorrelation and volume scattering. The temporal baseline of this pair is 48 days which might cause temporal decorrelation leading to loss of coherence. It is also observed from the Figs.(5-22) and (5-23) that the phase after correction has modified to a meaningful phase term. In reality DInSAR pairs with zero baseline, no phase noise and removing the atmospheric effects, the resultant phase should be close to zero. But this is not the case here. The resultant corrected phase is a combination of both phase noise and deformation phase.

The generated differential interferogram of data pairs of 29-11-2012 (Master) and 23-12-2012 (Slave) is shown in Fig.(5-25):

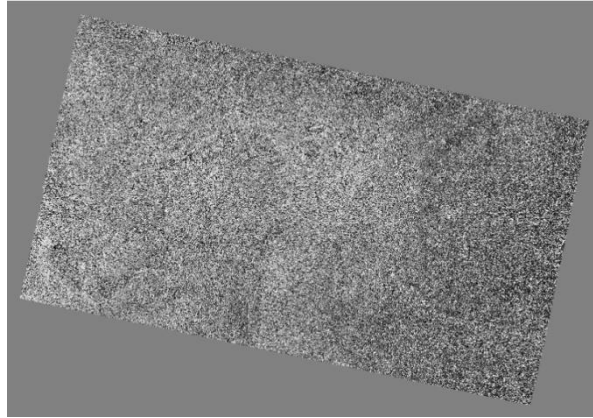


Figure 5-25: Differential interferogram of data pair (2)

The phase of differential interferogram of data pair (2) and atmospheric corrected phase are shown in Figs.(5-26) and (5-27):

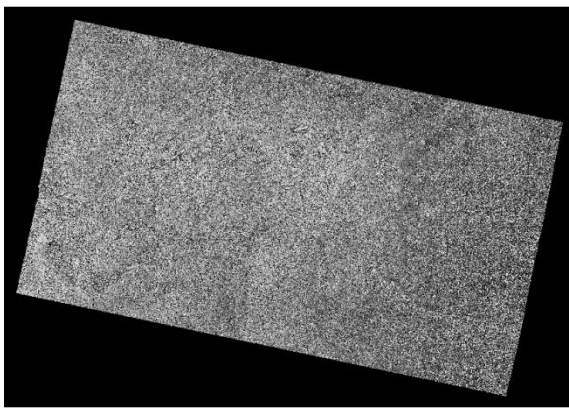


Figure 5-26: DInt phase of data pair (2)

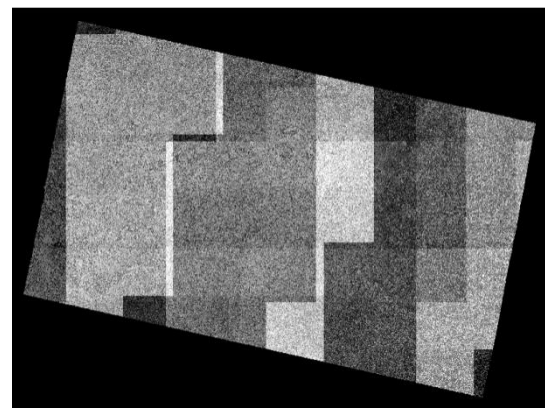


Figure 5-27: Corrected DInt phase of data pair (2)

The histograms of phases before and after correction are shown in Figs.(5-28) and (5-29):

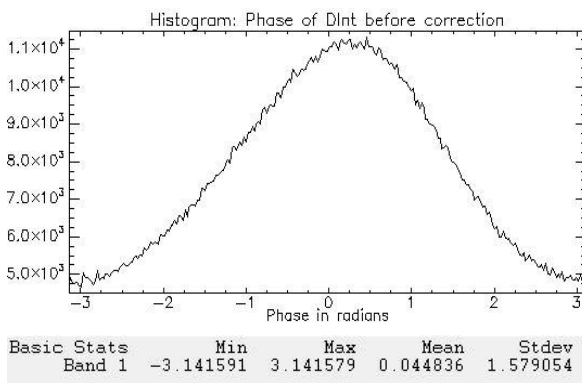


Figure 5-28: Phase variation before correction

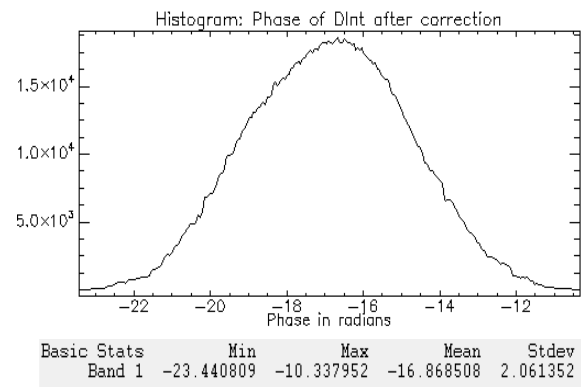


Figure 5-29: Phase variation after correction

The corrected differential interferogram of data pair (2) is shown in Fig.(5-30):

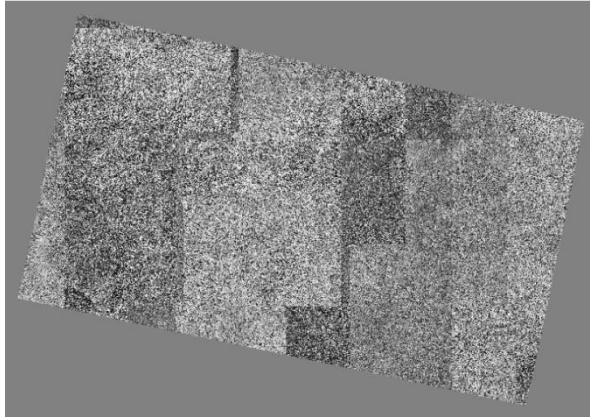


Figure 5-30: Corrected differential interferogram of data pair (2)

A discussion on the phase correction on differential interferogram of data pair (2):

The generated DInSAR phase is free from topographic phase removed by using the high resolution DEM. We have a priori information of the study area that subsidence has occurred during the time period. So the resultant phase of DInSAR generated is left with deformation phase, atmosphere phase and noise phase. Based on the phase correction procedure explained in section (4.5), the phase is corrected and the resultant phase free from atmospheric phase is shown in Fig.(5-27).The phase of the DInSAR before correction as shown in Fig.(5-28) shows a variation from -3 to +3 radians. After applying the phase correction, a drastic change is observed in the phase as shown in Fig.(5-29). The range varies between -23.4 and -10.3 radians. After the atmospheric correction, the residual phase is a combination of deformation phase and noise phase. The temporal baseline of this pair is 24 days which is the least among all the three interferometric pairs.It is also observed from the Figs.(5-28) and (5-29) that the trend of phase terms before and after correction is the same. In reality DInSAR pairs with zero baseline,no phase noise and removing the atmospheric effects, the resultant phase should be close to zero. But this is not the case here. The resultant corrected phase is a combination of both phase noise and deformation phase.

The generated differential interferogram of data pairs of 12-10-2012 (Master) and 23-12-2012 (Slave) is shown in Fig.(5-31):

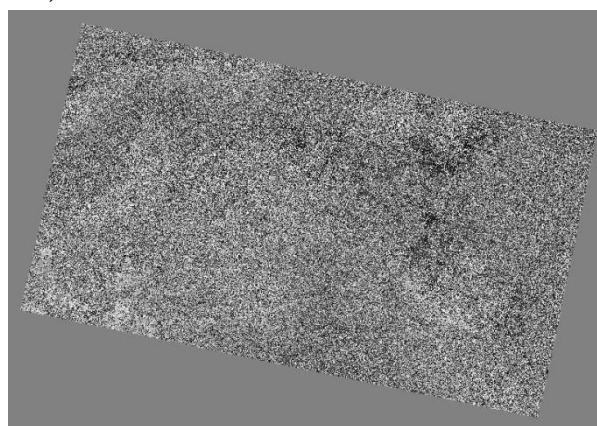


Figure 5-31: Differential interferogram of data pair (3)

The phase of differential interferogram of data pair (3) and atmospheric corrected phase are shown in Figs.(5-32) and (5-33):

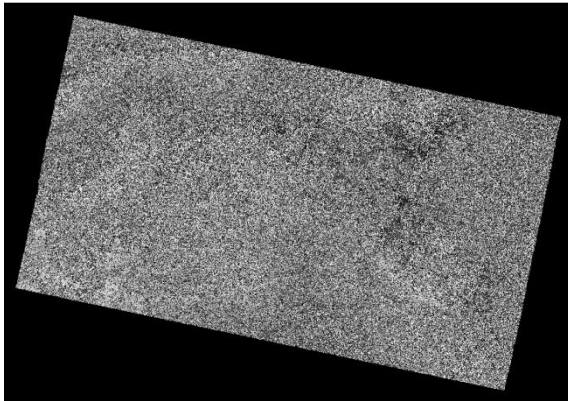


Figure 5-32: DInt phase of data pair (3)

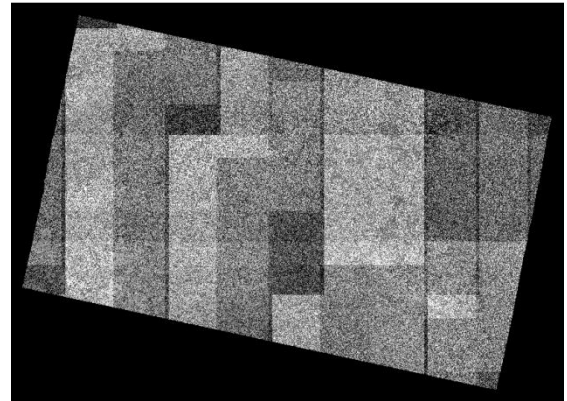
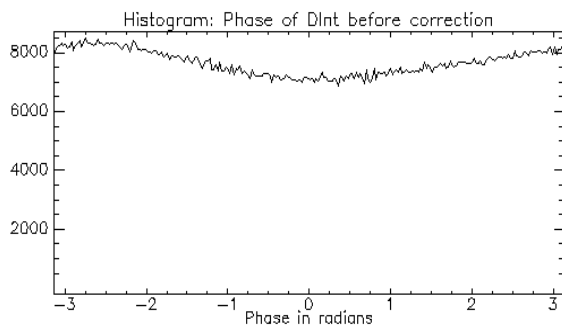


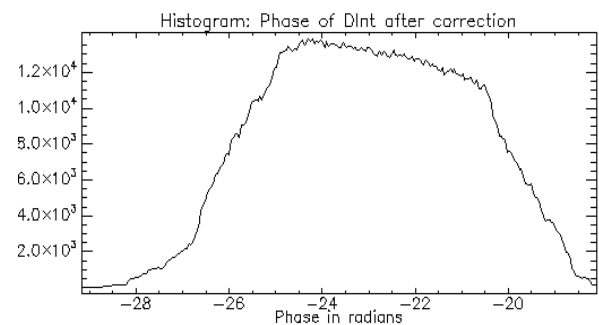
Figure 5-33: Corrected DInt phase of data pair (3)

The histograms of phases before and after correction are shown in Figs.(5-34) and (5-35):



Basic Stats					
Band 1	Min	Max	Mean	Stdev	
Band 1	-3.141593	3.141593	-0.030043	1.851434	

Figure 5-34: Phase variation before correction



Basic Stats					
Band 1	Min	Max	Mean	Stdev	
Band 1	-29.175295	-18.061100	-22.974138	2.061913	

Figure 5-35: Phase variation after correction

The corrected differential interferogram of data pair (3) is shown in Fig.(5-30):

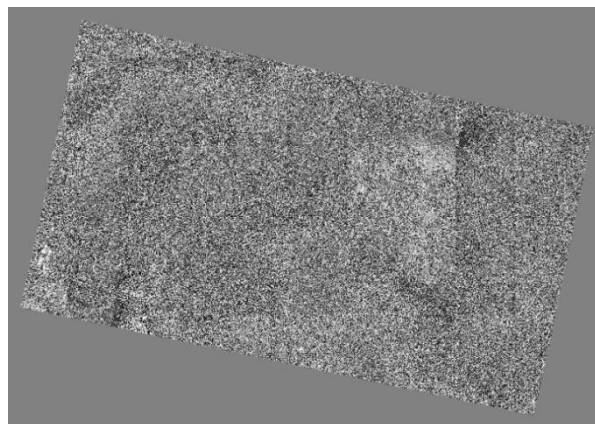


Figure 5-36: Corrected differential interferogram of data pair (3)

A discussion on the phase correction on differential interferogram of data pair (3):

The generated DInSAR phase is free from topographic phase removed by using the high resolution DEM. We have a priori information of the study area that subsidence has occurred during the time period. So the resultant phase of DInSAR generated is left with deformation phase, atmosphere phase and noise phase. Based on the phase correction procedure explained in section (4.5), the phase is corrected and the resultant phase free from atmospheric phase is shown in Fig.(5-33).The phase of the DInSAR before correction as shown in Fig.(5-28) shows a variation from -3 to +3 radians. After applying the phase correction, a drastic change is observed in the phase as shown in Fig.(5-29). The range varies between -29.1 and -18.0 radians. After the atmospheric correction, the residual phase is a combination of deformation phase and noise phase. The temporal baseline of this pair is 72 days which is the largest among all the three interferometric pairs. It is also observed from the Figs.(5-34) and (5-35) that the phase after correction has modified to a meaningful phase term. In reality DInSAR pairs with zero baseline, no phase noise and removing the atmospheric effects, the resultant phase should be close to zero. But this is not the case here. The resultant corrected phase is a combination of both phase noise and deformation phase. This pair has more noise as compared to the other two pairs which might have been caused due to temporal decorrelation.

The generated differential interferograms have been filtered using Boxcar filter for noise reduction and identification of subsidence fringes.

The filtered differential interferograms (Fint) of data pair (1) before and after correction are shown:

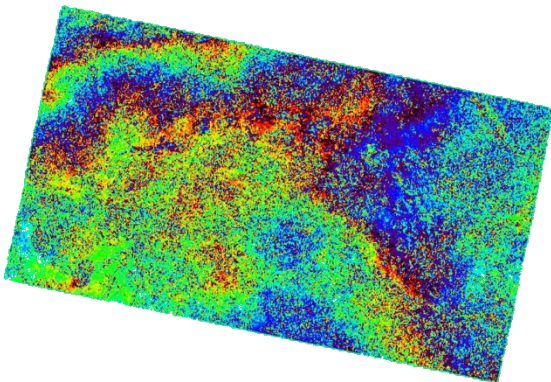


Figure 5-37: Fint before correction (pair 1)

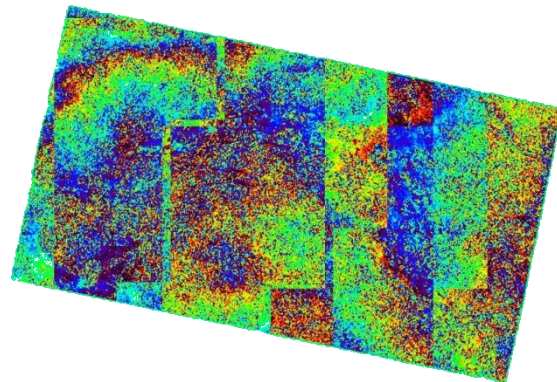


Figure 5-38: Fint after correction (pair 1)

A discussion on the filtered differential interferogram of data pair (1):

It is clearly observed from the Figs.(5-37) and (5-38) that even after the filtering applied large amount of noise is present in the data pairs which obscures the deformation information. Even after atmospheric correction is applied, the phase noise has dominated the interferogram which in turns makes difficult to identify or even discriminate deformation information from phase noise. The perpendicular baseline of this data pair is 98.356 m and the temporal baseline is 48

days. The phase noise in the data might be due to the geometric decorrelation or even the temporal decorrelation.

The filtered differential interferograms (Fint) of data pair (3) before and after correction are shown:

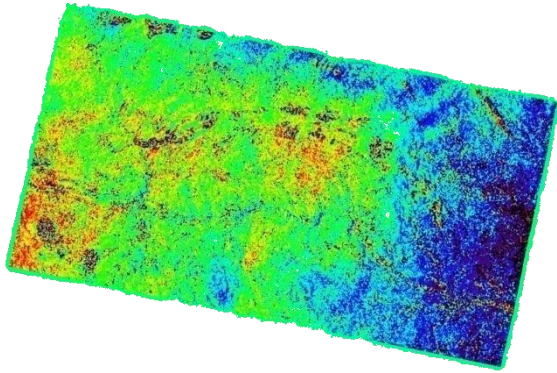


Figure 5-39: Fint before correction (pair 2)

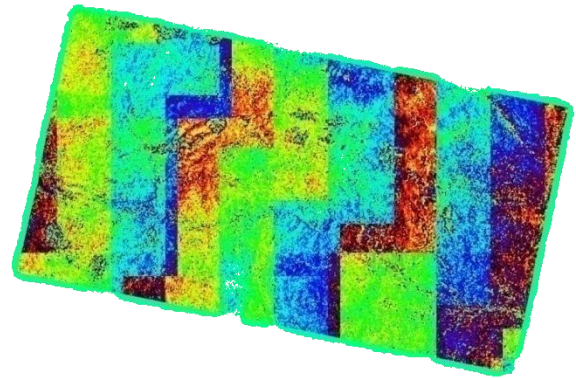


Figure 5-40: Fint after correction (pair 2)

A discussion on the filtered differential interferogram of data pair (2):

It is clearly observed from the Figs.(5-39) and (5-40) filtering has smoothed the image and noise has been removed to a major extent. The subsidence fringes are clearly visible. The presence of less noise in the pair might be the reason that among the three pairs, this pair has the shortest temporal baseline. So the temporal decorrelation factor might have been low in this case. The perpendicular baseline of this pair is 155.98 m which is optimum to make this pair suitable for interferometry.

The filtered differential interferograms (Fint) of data pair (3) before and after correction are shown:

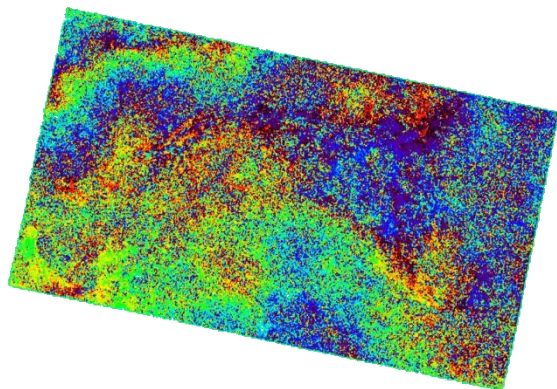


Figure 5-41: Fint before correction (pair 3)

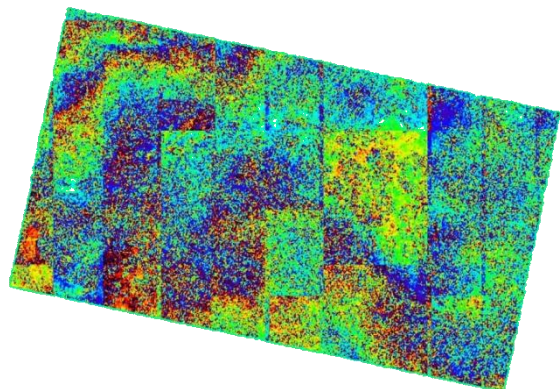


Figure 5-42: Fint after correction (pair 3)

A discussion on the filtered differential interferogram of data pair (3):

It is clearly observed from the Figs.(5-41) and (5-42) that even after the filtering applied a large amount of noise is present in the data pairs which obscures the deformation information. Even

after atmospheric correction is applied, the phase noise has dominated the interferogram which in turns makes difficult to identify or even discriminate deformation information from phase noise. The perpendicular baseline of this data pair is 58.461 m and the temporal baseline is 72 days. The phase noise in the data might be due to the geometric decorrelation or even the temporal decorrelation. This data pair has the largest temporal baseline among the three pairs.

A subsidence fringe visualized from differential interferogram of data pair (2):

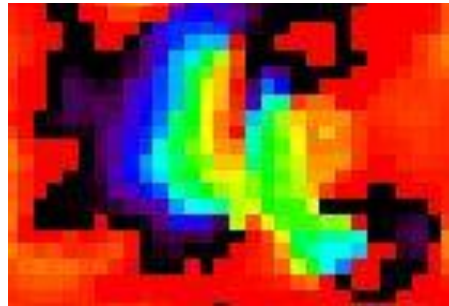
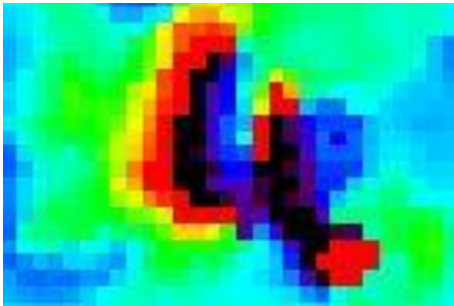
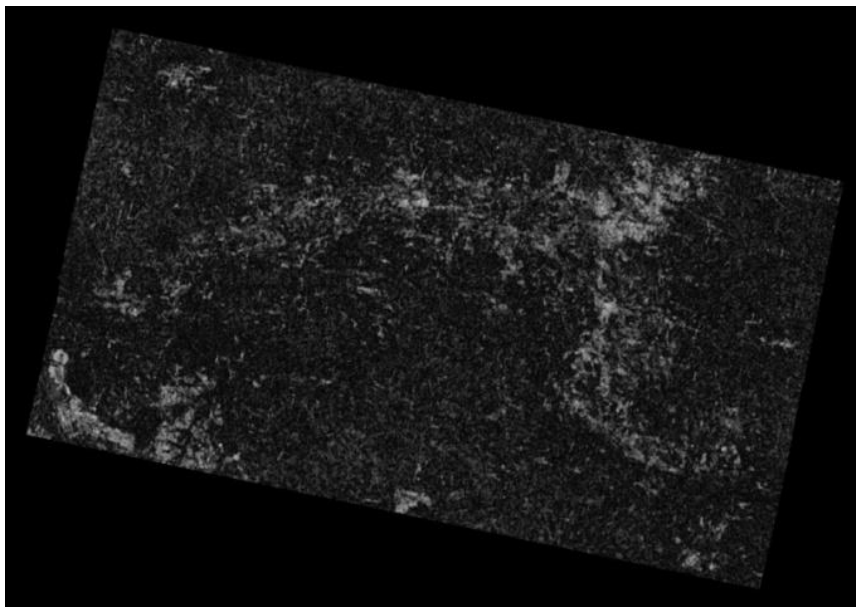


Figure 5-43: Subsidence fringe before correction Figure 5-44: Subsidence fringe after correction

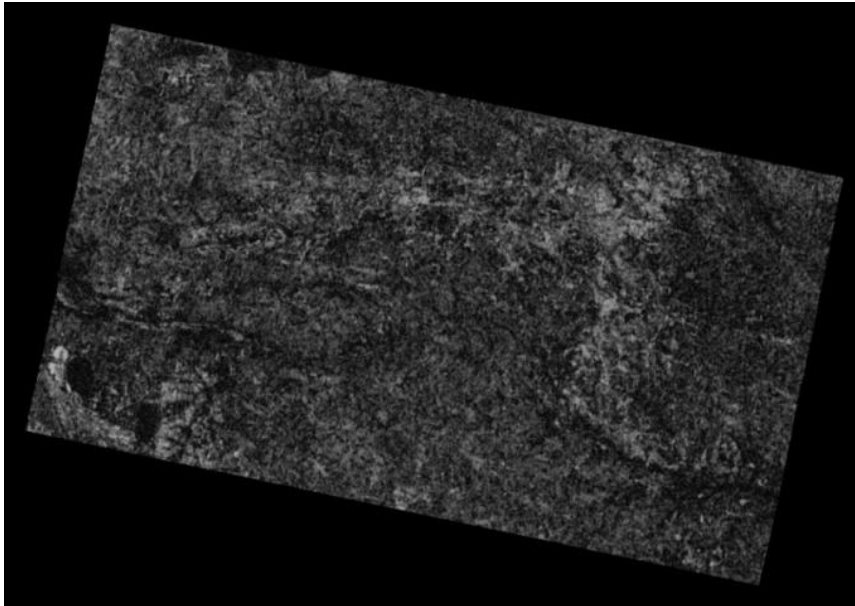
The fringe cycle pattern has changed after atmospheric correction showing an improvement of phase cycles and also better identification of the subsidence extent as compared to that before atmospheric correction.

Coherence images of the data pairs (1), (2) and (3) are shown:



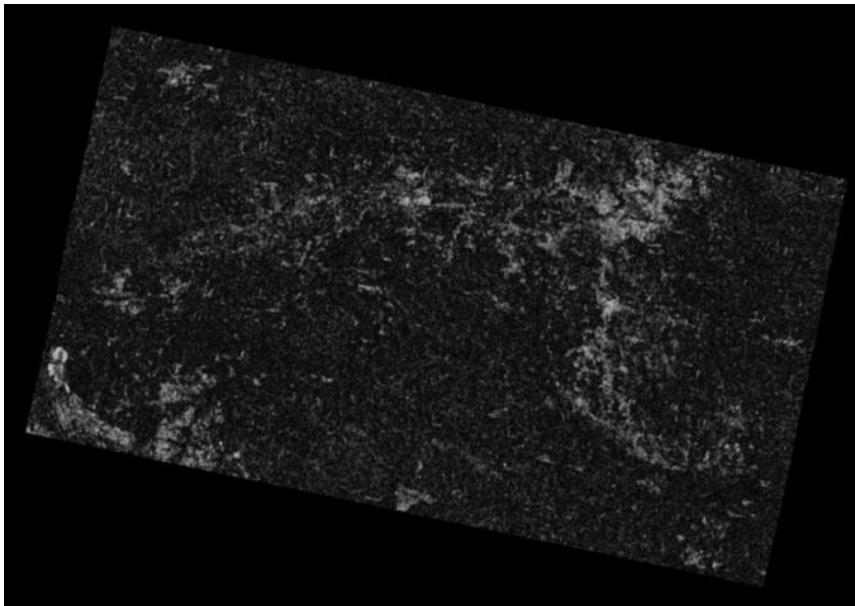
Statistics of coherence: Min: 0.000003 Max: 0.776691 Mean: 0.132297

Figure 5-45: Coherence image of data pair (1)



Statistics of coherence: Min: 0.000094 Max: 0.745828 Mean: 0.203603

Figure 5-46: Coherence image of data pair (2)



Statistics of coherence: Min: 0.000011 Max: 0.796733 Mean: 0.125230

Figure 5-47: Coherence image of data pair (3)

A discussion on the coherence for the data pairs:

The coherence images of the data pairs shown above clearly indicate that these pairs have very low coherence. A strong coherency shows that the two images are nearly identical. This is a very important issue to perform interferometry. The three data pairs show very low coherence. The reason for the low coherency might be due to the presence of different types of land use and land cover. The terrain is continuously changing because of the mining activities and land degradation. This might serve purpose for the low coherence observed. Among the three pairs, the pair nov-dec data pair exhibits better coherence than the other two. This data pair has been acquired with less time interval as compared to the other two. Temporal decorrelation might be a factor for the lower coherency exhibited by the other two data pairs.

The subsidence fringes after atmospheric correction were better visible in the data pair exhibiting better coherence. This data pair was used to derive the land subsidence measurements.

The data pair (1) and data pair (2) exhibited more phase noise and more over the overall coherence is low. These pairs were discarded for further land subsidence analysis.

Further, previously shown in section(5.2), specifically the curve fitting graphs of temperature and pressure data for October show higher uncertainty in terms of confidence interval as compared to that of November and December. This further justifies the exclusion of data pairs associated with October as master image.

Coherence subset from the data pair (2) for the test sites are shown:

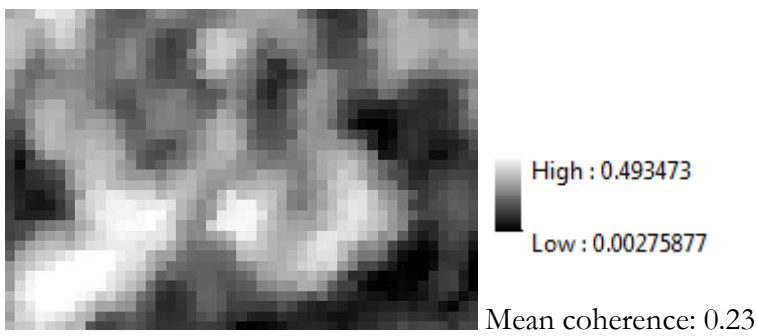


Figure 5-48: Coherence image of Maheshpur test site

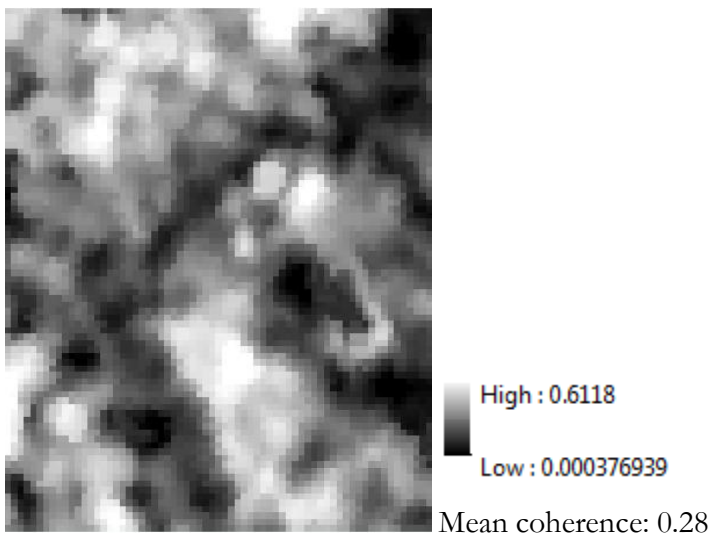


Figure 5-49: Coherence image of Bastacolla test site

From the Figs.(5-48) and(5-49), it is observed that the two test sites exhibit low coherence. As compared to the Maheshpur test site, Bastacolla exhibits higher coherency for the data pair (2).

5.7. Subsidence measurement and validation

From the atmospherically corrected filtered interferogram of data pair (2), the fringes showing subsidence were identified and their rates of subsidence have been calculated using the formula in section (4.6).

Subsidence fringes identified and spatial location of the test sites:

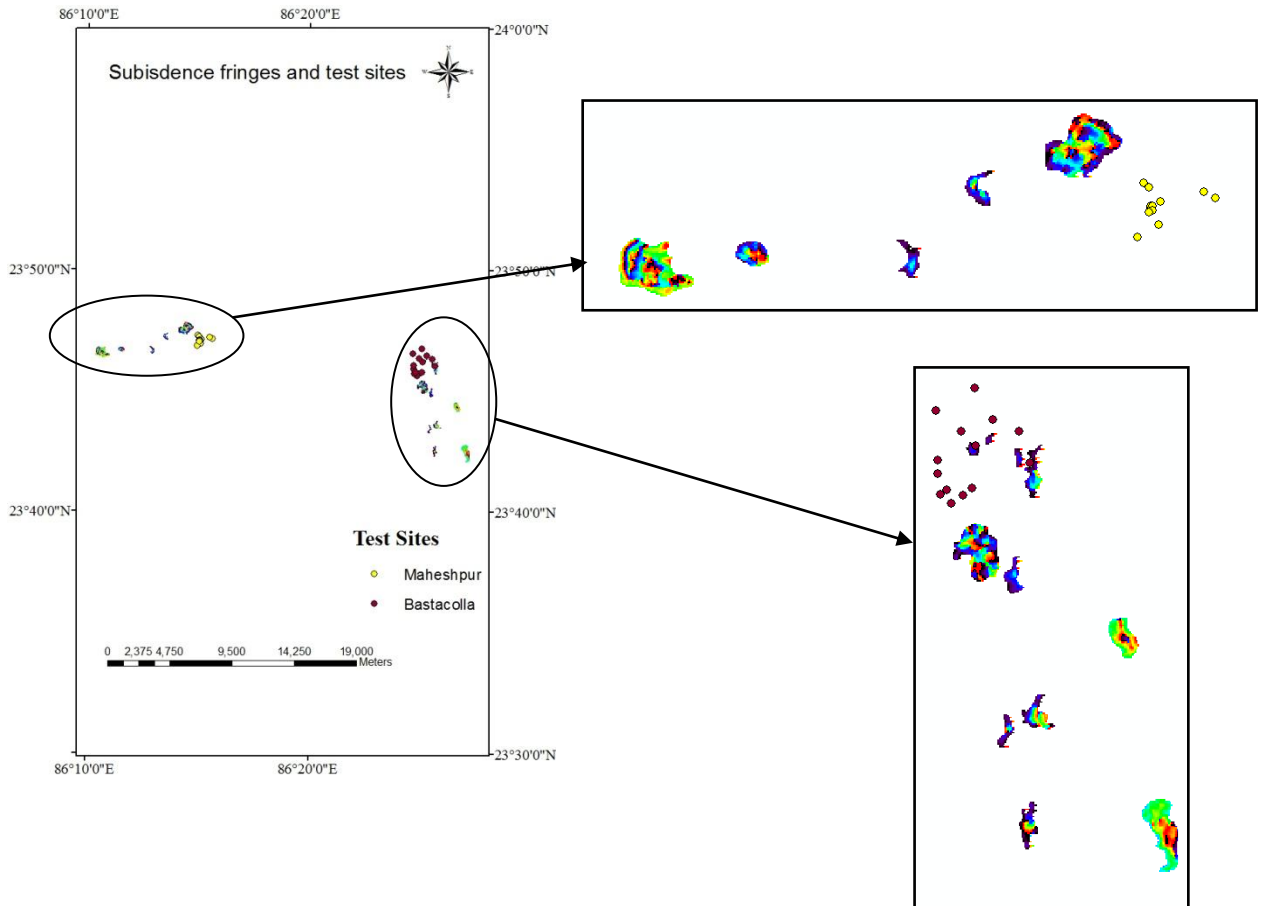


Figure 5-50: Map showing subsidence fringes and test site locations

A discussion on the subsidence fringes identified and the test site locations:

It is clearly observed from the above map that no subsidence fringes were detected in the maheshpur test site. There were fringes found north-west to the test site. The distance of the closest fringe detected is 658 m from the test site. The mean coherence of this test site is low as shown in Fig.(5-48). This might be one the factor for the absence of subsidence fringes in the test site.

Some subsidence fringes were identified in and near the Bastacolla test site. Most of the fringes were detected to the south and south east portion of the test site. Four fringes were detected within the circumference of the test site. The mean coherence of this test site was observed to be higher than the Maheshpur test site.

Rate of subsidence(mm/year) and areas(m^2) associated:

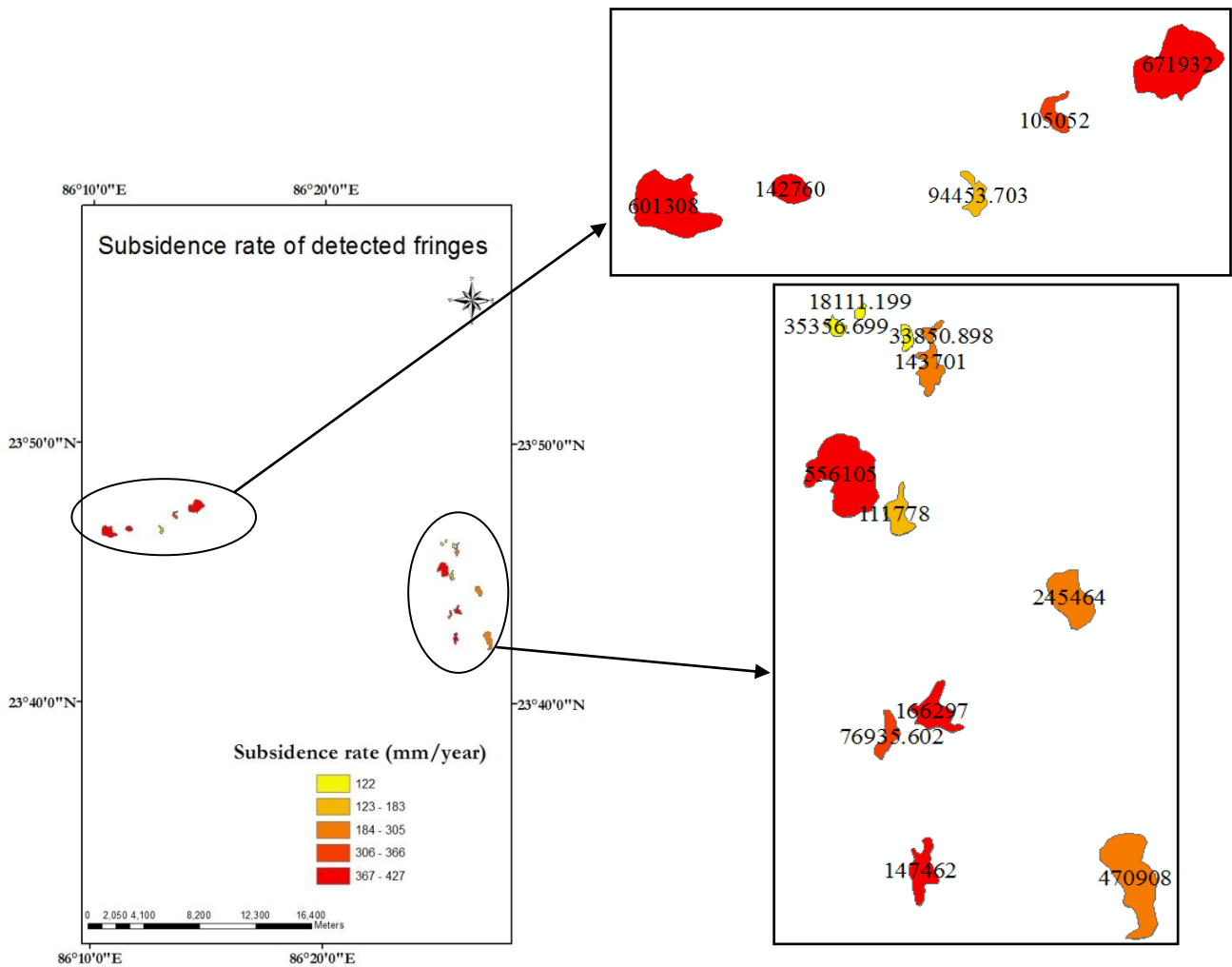


Figure 5-51: Map showing subsidence rate of observed fringes

A discussion on the subsidence rates obtained:

The rate of subsidence of the detected fringes is shown in the Fig.(5-51) describes the subsidence rate of each fringe and its corresponding area.

Validation of subsidence rates with respect to the Bastacolla ground leveling data:

There are a total of 73 pillars established in the test site each separated by a distance of 14 m respectively. The entire test site covers an area of about 3,483,517.41 Square Meters. The subsidence for each pillar has been recorded for a time period. The pillars do not have the spatial coordinates, so the validation is done based on statistical analysis by taking the minimum, maximum and mean subsidence rates of the pillars associated with the area of the test site.

The Bastacolla area rate of subsidence statistics are shown:

Minimum subsidence rate observed: 29.52 mm/yr
 Maximum subsidence rate observed: 4067.32 mm/yr
 Mean subsidence rate of 73 pillars observed: 1118.53 mm/yr

The mean subsidence rate is observed for an area of 3,483,517.41 Square Meters.

Fringes identified for validation:

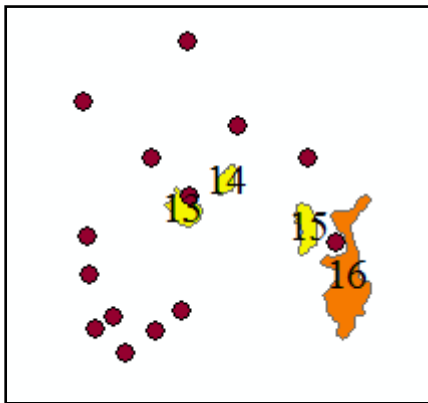


Figure 5-52: Subsidence zones observed near Bastacolla test site

Subsidence rate from DInSAR:

Table 5-2: Subsidence rate of subsidence zones identified near Bastacolla test site

Fringe Number	Subsidence rate (mm/year)	Subsided area (sq. meters)
Fringe 13	122	35356.70
Fringe 14	122	18111.20
Fringe 15	122	33850.90
Fringe 16	305	143701.00

A discussion on the comparison of results from DInSAR and ground levelling data:

It is clearly observed from the results that the subsidence rates of the fringes obtained from DInSAR are within the range of the subsidence rates observed in the test site. The subsidence observed in the Bastacolla area is higher than that of the derived results from DInSAR. The area of subsidence is very much higher as compared to that of the subsidence fringes detected. The subsidence fringes detected in the test site were in the south-east of the test site. As comparing these fringes, the coherence image of the test site also shows higher coherence in the south-east portion of the test site. The fringes were detected due to the higher coherence preserved in the south-east area of the test site.

6. CONCLUSIONS AND RECOMMENDATIONS

This section has been divided into two sections namely conclusions (section6.1) and recommendations (section6.2)

6.1. Conclusions

DInSAR is an effective tool to measure the surface deformations. The DInSAR is generated through two pass differential interferometry (using an external DEM) or three pass differential interferometry (using another Interferometric pair). In this work, the former technique was incorporated. A high resolution DEM was used to remove the topographic phase and identify the displacement phase which is the primary aim of DInSAR. Repeat pass interferometry is affected by the baseline decorrelation, surface decorrelation and the atmospheric signal present in the data. The variable state of atmosphere during the acquisition time is the reason for the atmospheric effects on repeat pass interferometry. Even longer temporal baselines lead to the decorrelation and this incorporates noise in the data. The atmospheric effects on the Interferometric phase hinder the results of displacement and heights measured. In order to mitigate these effects, an integrated approach was applied in this research work to understand the affects of atmosphere on the interferograms.

Q.1) What will be the errors induced by tropospheric and ionospheric component on the RADAR signal?

A.1) The two main layers of the atmosphere namely troposphere and ionosphere induce the atmospheric effect on the interferograms. The temperature, pressure and water vapour are the main components of the troposphere which cause the refractivity of the RADAR signal. The total electron content in the ionosphere is the main factor for phase advance or path shortenings of the RADAR signal. As described in section (5.3), the tropospheric path delay for the time of acquisition in the months of October, November and December ranges between 5.0 m to 5.07 m. As shown in section (5.4), the ionospheric path delay for the time of acquisition in October, November and December are -0.189 m, -0.137 m and -0.118 m respectively. The negative sign indicates a phase advance. The total path delay was estimated by summing the tropospheric and ionospheric path delays which were then subtracted from the phase of DInSAR to generate atmospheric effect free DInSAR.

Q.2) How can the parameters (temperature, pressure and water vapour pressure) derived from MODIS water vapour products be modeled in synchronization with acquisition time of RADARSAT-2?

A.2) RADARSAT-2 SLC data pair is acquired at 05:47AM (IST). There are no satellites providing meteorological data near or at that time. The ground meteorological data was collected from a single weather station. This lacked spatial variation of the meteorological data. So, the integrated approach of using both ground meteorological data and satellite based meteorological data used

in this research study has given an insight to model the tropospheric path delay. Using this approach, the MODIS temperature, pressure and water vapour pressure were calibrated to the time of acquisition of RADARSAT-2 from which the tropospheric path delay has been computed. By analyzing the trend of MODIS temperature and pressure readings with respect to the weather station temperature and pressure readings for the same point in the field and time, a relation has been defined between the MODIS readings and weather station readings for both temperature and pressure as described in section (5.2). Hence based on the relation, the weather station readings at 05:47 AM (IST) can be used to model and calibrate the MODIS readings for that time. The water vapour pressure band was directly from the temperature and humidity readings of the weather station as described in section (5.2). Hence, this initiative has given an insight to explore the tropospheric affects on the RADARSAT-2 data.

Q.3) What will be the accuracy of land subsidence measurements after atmospheric correction?

A.3) The rate of subsidence derived from the wrapped interferogram was compared to the subsidence rate derived from leveling performed in the test sites. The rate of subsidence from the DInSAR was described in Section (5.7). According to the results, subsidence fringes were not found from the Differential interferogram in Maheshpur test site. Lack of coherence in the data pair at the test site might be one of the causative factors for this. Four subsidence fringes were found in the Bastacolla test site and these fringes were found in the area having high coherence. The subsidence rates of these fringes were shown in section (5.7). From the results shown in section (5.7), the subsidence rates obtained from the DInSAR are in the acceptable range (within the lower and upper limits of subsidence rates from leveling data). Atmospheric correction had drastic effect on some fringes which influenced the fringe cycle for some subsidence fringes. One of the examples was shown in section (5.6). It can be concluded that atmospheric effects influence the measurements to a certain extent and their mitigation is necessary to derive accurate and precise measurements.

6.2. Recommendations

The present study aims at removing the atmospheric effects from the phase of the interferogram. The integrated approach initiated in this study made use of an automated weather station for ground meteorological observations. The entire field work was carried out using a single weather station. The weather station was useful in recording the meteorological data in the study area for a time interval proposed. The readings were continuously recorded at a single place. This procedure could show the temporal dynamics of the meteorological data for a certain area. This lacked the spatial variation of the temperature, pressure and water vapour pressure readings from the weather station. So, if the study could be performed using more weather stations placed in and around the study area, the spatial pattern of the meteorological data could also be analyzed.

Due to time constraint, the ground meteorological data collection was planned for two days before and two days after the date of pass of RADARSAT-2. It would be recommended that the

data collection period could be increased to better analyze the trend and pattern of the ground meteorological data which could lead to better comparison and analysis with respect to the satellite based meteorological data. This could enhance and improve the modelling approach.⁴ The coherence of the data pairs used for this study is very low. The main requirement for performing repeat pass interferometry is coherence. Among the three data pairs, only one data pair was used to derive the subsidence measurements as it had less noise. Due to the loss of coherence in the data pairs, phase unwrapping will lead to problems. Further work should be considered for phase unwrapping of data pairs exhibiting low coherence.

REFERENCES

- [1] F. K. Li and R. M. Goldstein, "Studies of multibaseline spaceborne interferometric synthetic aperture radars," *Geoscience and Remote Sensing, IEEE Transactions on*, vol. 28, no. 1, pp. 88–97, 1990.
- [2] R. F. Hanssen, *Radar Interferometry: Data Interpretation and Error Analysis*. Springer, 2001.
- [3] P. A. Rosen, S. Hensley, I. R. Joughin, F. K. Li, S. N. Madsen, E. Rodriguez, and R. M. Goldstein, "Synthetic aperture radar interferometry," *Proceedings of the IEEE*, vol. 88, no. 3, pp. 333–382, 2000.
- [4] X. Ding, Z. Li, J. Zhu, G. Feng, and J. Long, "Atmospheric Effects on InSAR Measurements and Their Mitigation," *Sensors*, vol. 8, no. 9, pp. 5426–5448, Sep. 2008.
- [5] A. K. Gabriel, R. M. Goldstein, and H. A. Zebker, "Mapping Small Elevation Changes Over Large Areas: Differential Radar Interferometry," *J. Geophys. Res.*, vol. 94, no. B7, pp. 9183–9191, 1989.
- [6] F. Chaabane, A. Avallone, F. Tupin, P. Briole, and H. Maitre, "A Multitemporal Method for Correction of Tropospheric Effects in Differential SAR Interferometry: Application to the Gulf of Corinth Earthquake," *IEEE Transactions on Geoscience and Remote Sensing*, vol. 45, no. 6, pp. 1605–1615, Jun. 2007.
- [7] R. S. Chatterjee, B. Fruneau, J. P. Rudant, P. S. Roy, P.-L. Frison, R. C. Lakhera, V. K. Dadhwal, and R. Saha, "Subsidence of Kolkata (Calcutta) City, India during the 1990s as observed from space by Differential Synthetic Aperture Radar Interferometry (D-InSAR) technique," *Remote Sensing of Environment*, vol. 102, no. 1–2, pp. 176–185, May 2006.
- [8] H. Tarayre and D. Massonnet, "Effects of a refractive atmosphere on interferometric processing," in *Geoscience and Remote Sensing Symposium, 1994. IGARSS '94. Surface and Atmospheric Remote Sensing: Technologies, Data Analysis and Interpretation., International*, 1994, vol. 2, pp. 717 – 719 vol.2.
- [9] H. A. Zebker, P. A. Rosen, and S. Hensley, "Atmospheric effects in interferometric synthetic aperture radar surface deformation and topographic maps," *Journal of Geophysical Research*, vol. 102, no. B4, pp. 7547–7563, 1997.
- [10] J. Askne and H. Nordius, "Estimation of tropospheric delay for microwaves from surface weather data," *Radio Science*, vol. 22, no. 3, pp. 379–386, 1987.
- [11] Z. Li, "Interferometric synthetic aperture radar (InSAR) atmospheric correction: GPS, Moderate Resolution Imaging Spectroradiometer (MODIS), and InSAR integration," *Journal of Geophysical Research*, vol. 110, no. B3, 2005.
- [12] N. Pierdicca, F. Rocca, P. Basili, S. Bonafoni, D. Cimini, P. Ciotti, R. Ferretti, W. Foster, F. S. Marzano, V. Mattioli, M. Montopoli, R. Notarpietro, S. Padmanabhan, D. Perissin, E. Pichelli, S. Reising, S. Sahoo, and G. Venuti, "Atmospheric water-vapour effects on Spaceborne Interferometric SAR imaging: Data synergy and comparison with ground-based measurements and meteorological model simulations at urban scale," in *3rd European Conference on Antennas and Propagation, 2009. EuCAP 2009*, 2009, pp. 3443 –3447.

- [13] Z. W. Li, W. B. Xu, G. C. Feng, J. Hu, C. C. Wang, X. L. Ding, and J. J. Zhu, "Correcting atmospheric effects on InSAR with MERIS water vapour data and elevation-dependent interpolation model," *Geophysical Journal International*, vol. 189, no. 2, pp. 898–910, Mar. 2012.
- [14] Z. Li, "Interferometric synthetic aperture radar (InSAR) atmospheric correction: GPS, Moderate Resolution Imaging Spectroradiometer (MODIS), and InSAR integration," *Journal of Geophysical Research*, vol. 110, no. B3, 2005.
- [15] S. Sukumar, "Ionospheric refraction effects on radio interferometer phase," *Journal of Astrophysics and Astronomy*, vol. 8, no. 4, pp. 281–294, 1987.
- [16] L. C. Graham, "Synthetic interferometer radar for topographic mapping," *Proceedings of the IEEE*, vol. 62, no. 6, pp. 763–768, 1974.
- [17] H. A. Zebker and R. M. Goldstein, "Topographic mapping from interferometric synthetic aperture radar observations," *Journal of Geophysical Research*, vol. 91, no. B5, p. 4993, 1986.
- [18] J. G. R. Earth and H. A. Zebker, "On the derivation of coseismic displacement fields using differential radar interferometry: the Landers earthquake," 1994.
- [19] R. M. Goldstein, E. R. Caro, and C. Wu, "Method and apparatus for contour mapping using synthetic aperture radar," Jan. 1985.
- [20] A. K. Gabriel and R. M. Goldstein, "Crossed orbit interferometry: theory and experimental results from SIR-B," *International Journal of Remote Sensing*, vol. 9, no. 5, pp. 857–872, 1988.
- [21] L. Jiang, H. Lin, J. Ma, B. Kong, and Y. Wang, "Potential of small-baseline SAR interferometry for monitoring land subsidence related to underground coal fires: Wuda (Northern China) case study," *Remote Sensing of Environment*, vol. 115, no. 2, pp. 257–268, 2011.
- [22] F. I. Okeke, "InSAR Operational and Processing Steps for DEM Generation," in *Promoting Land Administration and Good Governance*, pp. 1–13, 2006.
- [23] A. Reigber and R. Scheiber, "Airborne differential SAR interferometry: First results at L-band," *Geoscience and Remote Sensing, IEEE Transactions on*, vol. 41, no. 6, pp. 1516–1520, 2003.
- [24] T. Strozzi, U. Wegmuller, C. L. Werner, A. Wiesmann, and V. Spreckels, "JERS SAR interferometry for land subsidence monitoring," *Geoscience and Remote Sensing, IEEE Transactions on*, vol. 41, no. 7, pp. 1702–1708, 2003.
- [25] G. Herrera, R. Tomás, J. M. López-Sánchez, J. Delgado, J. J. Mallorqui, S. Duque, and J. Mulas, "Advanced DInSAR analysis on mining areas: La Union case study (Murcia, SE Spain)," *Engineering Geology*, vol. 90, no. 3, pp. 148–159, 2007.
- [26] H. Lee and J. G. Liu, "Topographic phase corrected coherence estimation using multi-pass differential SAR interferometry: differential coherence," in *Geoscience and Remote Sensing Symposium, 2000. Proceedings. IGARSS 2000. IEEE 2000 International*, 2000, vol. 2, pp. 776–778.
- [27] A. Ferretti, C. Prati, and F. Rocca, "Permanent scatterers in SAR interferometry," *Geoscience and Remote Sensing, IEEE Transactions on*, vol. 39, no. 1, pp. 8–20, 2001.
- [28] L. Guang, G. Huadong, F. Jinghui, G. Xiaofang, Z. Perski, and Y. Huanyin, "Mining area subsidence monitoring using Multi-band SAR data," in *Urban Remote Sensing Event, 2009 Joint*, 2009, pp. 1–6.
- [29] L. Bayuaji, J. T. S. Sumantyo, and H. Kuze, "ALOS PALSAR D-InSAR for land subsidence mapping in Jakarta, Indonesia," *Canadian Journal of Remote Sensing*, vol. 36, no. 1, pp. 1–8, 2010.

- [30] F. K. Li and R. M. Goldstein, "Studies of multibaseline spaceborne interferometric synthetic aperture radars," *Geoscience and Remote Sensing, IEEE Transactions on*, vol. 28, no. 1, pp. 88–97, 1990.
- [31] H. Tarayre and D. Massonnet, "Atmospheric propagation heterogeneities revealed by ERS-1," *Geophys. Res. Lett.*, vol. 23, no. 9, pp. 989–992, 1996.
- [32] R. Hanssen, "Atmospheric heterogeneities in ERS tandem SAR interferometry," DEOS Report No. 98.1, Delft University press: Delft, the Netherlands, 1998.
- [33] J. Saastamoinen, "Contributions to the theory of atmospheric refraction," *Bulletin Géodésique (1946-1975)*, vol. 107, no. 1, pp. 13–34, 1973.
- [34] M. J. Nahvi, "An expert system approach to determination of tropospheric error in microwave ranging," *Acta Astronautica*, vol. 17, no. 3, pp. 359–366, Mar. 1988.
- [35] Z. Li, X. Ding, and G. Liu, "Modeling atmospheric effects on InSAR with meteorological and continuous GPS observations: algorithms and some test results," *Journal of Atmospheric and Solar-Terrestrial Physics*, vol. 66, no. 11, pp. 907–917, Jul. 2004.
- [36] G. Wadge, M. Zhu, R. J. Holley, I. N. James, P. A. Clark, C. Wang, and M. J. Woodage, "Correction of atmospheric delay effects in radar interferometry using a nested mesoscale atmospheric model," *Journal of Applied Geophysics*, vol. 72, no. 2, pp. 141–149, Oct. 2010.
- [37] B.-C. Gao, "Water vapor retrievals using Moderate Resolution Imaging Spectroradiometer (MODIS) near-infrared channels," *Journal of Geophysical Research*, vol. 108, no. D13, 2003.
- [38] Z. Li, "Interferometric synthetic aperture radar (InSAR) atmospheric correction: GPS, Moderate Resolution Imaging Spectroradiometer (MODIS), and InSAR integration," *Journal of Geophysical Research*, vol. 110, no. B3, 2005.
- [39] P. M. Balaji, "Estimation and Correction of Tropospheric and Ionospheric Effects on Differential SAR Interferograms," M.Sc., Indian Institute of Remote Sensing (IIRS) and International Institute for Geoinformation Science and Earth Observation (ITC), 2011.
- [40] F. Wang, Z. Huang, L. Zhou, and D. Zhang, "The atmosphere correction in SBAS D-InSAR land subsidence monitoring application: A case study in Jiaying-Huzhou plain, China," in *2010 18th International Conference on Geoinformatics*, 2010, pp. 1–5.
- [41] M. Jehle, O. Frey, D. Small, E. Meier, and D. Nüesch, "Improved Knowledge of SAR Geometry through Atmospheric Modelling," IN "PROCEEDINGS OF EUSAR 2004," pp. 25–27.
- [42] P. A. Rosen, S. Hensley, and C. Chen, "Measurement and mitigation of the ionosphere in L-band Interferometric SAR data," in *Radar Conference, 2010 IEEE*, 2010, pp. 1459–1463.
- [43] S. Schaer, G. Beutler, and M. Rothacher, "Mapping and predicting the ionosphere," in *Proceedings of the 1998 IGS Analysis Center Workshop, Darmstadt, Germany*, 1998.
- [44] S. N. V. S. Prasad, P. V. S. Rama Rao, D. S. V. V. D. Prasad, K. Venkatesh, and K. Niranjana, "On the variabilities of the Total Electron Content (TEC) over the Indian low latitude sector," *Advances in Space Research*, vol. 49, no. 5, pp. 898–913, Mar. 2012.
- [45] D. Bilitza and B. W. Reinisch, "International Reference Ionosphere 2007: Improvements and new parameters," *Advances in Space Research*, vol. 42, no. 4, pp. 599–609, Aug. 2008.

- [46] Kenpankho, "Comparison of GPS TEC measurements with IRI TEC prediction at the equatorial latitude station, Chumphon, Thailand," *Earth, Planets and Space*, vol. 63, no. 4, pp. 365–370, Jun. 2011.
- [47] SARscape, "Synthetic Aperture Radar and SARscape," Feb-2013.
- [48] I. H. Woodhouse, *Introduction to Microwave Remote Sensing*, 1st ed. CRC Press, 2004.
- [49] G.Singh, M.K.Jain, B.Paul, R.D.Gupta and E.V.R.Raju, "Clusterization of mines for obtaining comprehensive environmental clearance: A case study of BCCL Lease hold areas," *Journal of Indian School of Mines*, special vol., pp.13-20,2010.
- [50] Z. Yanjie, "A comparison of the different models used for interferograms flattening," in *Geoscience and Remote Sensing Symposium, 2005. IGARSS '05. Proceedings. 2005 IEEE International*, July, vol. 8, pp. 5494–5496.
- [51] C.-F. Chao, K.-S. Chen, J.-S. Lee, and C.-T. Wang, "Refined filtering of interferometric phase from INSAR data," in *Geoscience and Remote Sensing Symposium (IGARSS), 2012 IEEE International*, July, pp. 1821–1824.